Polarized neutron reflectometry study of complex magnetism and hydrogen incorporation in thin-film structures

Von der Fakultät Mathematik und Physik der Universität Stuttgart
zur Erlangung der Würde eines Doktors der Naturwissenschaften
(Dr.rer.nat.) genehmigte Abhandlung

Vorgelegt von:

Laura Guasco

aus Turin, Italien

Hauptberichter:	Prof. Dr. Bernhard Keimer
Mitberichter:	Prof. Dr. Laura Na Liu
Prüfungsvorsitzende:	Prof. Dr. Maria Daghofer
Tag der mündlichen Prüfung:	15.12.2022

Max-Planck-Institut für Festkörperforschung
Universität Stuttgart
2022

Contents

Abstract

In this thesis, we studied the structural and magnetic properties of simple metals and complex oxide thin films by means of polarized neutron reflectometry. Secondary characterization methods were x-ray reflectometry, x-ray and neutron diffraction, magnetometry, electrical transport, and magnetoresistance. We modified the nuclear and electronic properties of thin films via two routes, namely via hydrogen incorporation, in the case of niobium systems and complex oxide layers, and via depth modulated hole doping, in the case of manganite heterostructures.

The study of hydrogen absorption in different matrices is important for green energy, in particular in the electrodes of fuel cells or in hydrogen storage materials, but also to understand and take advantage of the modification of electronic, magnetic and optical properties of the host materials. Due to high sensitivity of neutrons to hydrogen atoms, neutron reflectometry is widely used to study hydrogen absorption in thin films in concentrations of 10 at.%. and higher. Here we demonstrate a way to detect smaller concentrations of hydrogen with faster measurement time, by the means of neutron waveguides. We established the method in a model system composed of thin niobium layers deposited on sapphire substrates. These layers form a potential well which acts as a neutron waveguide, and for characteristic resonance momentum transfer Q_{res} of neutrons reflected from the surface, strong features in the neutron reflectivity are observed. The method is based on tracking the Q_{res} as it shifts upon hydrogen loading. The shift is caused by the modification of the potential well depth, which changes the properties of the neutron waveguide shifting the position of the Q_{res}. In the small concentration limit, this shift is directly proportional to the concentration of the absorbed hydrogen. Our measurements have shown the feasibility of the resonant neutron reflectometry (also called waveguide) method to study the kinetics of *in*

situ hydrogen loading on a time scale of seconds with detection limits of ∼1 at.%. Following the proof-of-principle experiments, the waveguide method was applied to study the room temperature kinetics of absorption in niobium systems versus the film thickness, the crystalline quality, and the external gas pressure. Thanks to simultaneous x-ray reflectivity experiments, it was possible to observe two distinct processes, the film swelling and the hydrogen incorporation, characterized by different time scales. This set of measurements demonstrated that defects and grain boundaries have a central role in the kinetics of absorption, giving new insight on the incorporation mechanisms involved.

Another way to modify the electronic properties of thin films is by electron or hole-doping. This strategy, widely used in semiconductor technologies, can be applied as well to transition metal oxides. $La_{1-x}Sr_xMnO_3$ offers a wide range of tunable properties that can be implemented in heterostructures, by taking advantage of the complexity of its structural and magnetic phase diagram. With the atomic precision of the oxide molecular beam epitaxy we were able to tune the Sr-concentration x layer by layer, and synthesize superlattices with a large gradient in hole doping. Specifically, we used a sequence of layers with x=0.4 and x=0.8, corresponding to a ferromagnetic half-metal and an antiferromagnetic insulator, respectively. We observe a dramatic change of properties by varying the thickness of the x=0.8 antiferromagnetic layer. In particular, we observed a doubled long-range non-collinear magnetic order, which was hitherto not reported for manganite based homojunctions. In this state, magnetic moments in the neighbouring ferromagnetic layers form an angle α with respect to each other, which is the result of exchange interaction with the neighbouring canted A-type antiferromagnet. In addition, we show that the degree of non-collinearity of this system, expressed in terms of the angle α, can be tuned by application of small magnetic fields.

In conclusion, we give an overview on hydrogenation of transition metal oxides, to explore the perspectives offered by the combination of different methods presented in the thesis. We briefly explain the structural and electronic response of manganite and cuprate thin films to hydrogen exposure, as an example of future for the RNR method in the field of H-doping. Our preliminary results indicate that hydrogen is a powerful control parameter in complex systems such as complex oxides.

Zusammenfassung

In dieser Arbeit untersuchen wir die strukturellen und magnetischen Eigenschaften von dünnen Schichten aus einfachen Metallen und komplexen Oxiden mit Hilfe der polarisierten Neutronenreflektometrie. Weitere Charakterisierungsmethoden sind Röntgenreflektometrie, Röntgen- und Neutronendiffraktion, Magnetometrie, elektrischer Transport und Magnetowiderstand. Für die gezielte Modifikation der strukturellen und elektronischen Eigenschaften der dünnen Schichten verfolgten wir zwei Wege, nämlich die Dotierung mit Wasserstoff im Falle von Niob und komplexen Oxiden, und die tiefenmodulierte Dotierung mit Strontium im Falle von Manganat-Heterostrukturen.

Die Untersuchung der Wasserstoffabsorption in Materialien ist wichtig sowohl für Fragen der nachhaltigen Energiewirtschaft, speziell für Brennstoffzellen und Wasserstoffspeicherung, als auch für das Verständnis und die Nutzung der gezielten Modifikation der elektronischen, magnetischen und optischen Materialeigenschaften. Aufgrund der hohen Streuquerschnitts von Wasserstoff für Neutronenwird die Neutronenreflektometrie häufig zur Untersuchung der Wasserstoffabsorption in dünnen Filmen für Konzentrationen oberhalb von 10 at.% eingesetzt. Hier zeigen wir einen Weg, um noch kleinere Wasserstoffkonzentrationen mit Hilfe von Neutronenwellenleitern in kürzerer Zeit zu messen. Wir haben die Methode in einem Modellsystem etabliert, das aus dünnen Niobschichten besteht, die auf Saphir Substraten aufgebracht wurden. Der Neutronenwellenleiter, den diese Probe bildet, ruft starke Resonanzpeaks in der Reflektivität hervor. Die Methode basiert auf der Messung des charakteristischen Resonanz-Impulsübertrag Q_{res} , der sich bei der Beladung mit Wasserstoff verschiebt. Diese Verschiebung wird durch die Änderung des optischen Potenzials der Niob-Schichten verursacht, und ist im Bereich kleiner Konzentrationen direkt proportional zur Menge des absorbierten

Wasserstoffs. Unsere Messungen haben gezeigt, dass die Methode der resonanten Neutronenreflektometrie mittels Wellenleitern zur Untersuchung der Kinetik der in-situ Wasserstoffbeladung auf einer Zeitskala von Sekunden mit Nachweisgrenzen von ∼1 at.% möglich ist. Im Anschluss an die Proof-of-Principle-Experimente wurde die Wellenleitermethode angewandt, um die Kinetik der Absorption in Niob bei Raumtemperatur in Abhängigkeit von der Schichtdicke, der kristallinen Qualität und dem externen Gasdruck zu untersuchen. Dank gleichzeitiger Messung der Röntgenreflektivität war es möglich, zwei unterschiedliche Prozesse zu beobachten, nämlich das Aufquellen der Schicht und den Einbau von Wasserstoff, die durch unterschiedliche Zeitkonstanten gekennzeichnet sind. Diese Messungen bestätigten, dass Defekte und Korngrenzen eine zentrale Rolle bei der Absorptionskinetik spielen, und gaben neue Einblicke in die Zeitabhängigkeit der beteiligten Mechanismen.

Eine weitere Möglichkeit, die elektronischen Eigenschaften dünner Schichten zu verändern, ist die Ladungsdotierung. Diese Strategie, die in der Halbleitertechnologie als Standard angewandt wird, kann auch auf Übergangsmetalloxide übertragen werden. $La_{1-x}Sr_xMnO_3$ bietet angesichts der Komplexität seines strukturellen und magnetischen Phasendiagramms ein breites Spektrum an modifizierbaren Eigenschaften, die insbesondere in Heterostrukturen zu neuartigen Eigenschaften führen. Mit der atomaren Präzision der Oxid-Molekularstrahlepitaxie konnten wir die Sr-Konzentration x Schicht für Schicht abstimmen und Übergitter mit einem großen Gradienten in der Lochdotierung synthetisieren, wobei speziell ein ferromagnetisches Halbmetall mit x=0.4 und ein antiferromagnetischer Isolator mit x=0.8 als abwechselnde Schichten kombiniert wurden. Wir beobachten eine deutliche Veränderung der Eigenschaften durch Variation der Dicke der antiferromagnetischen x=0.8 Schicht. Insbesondere konnten wir eine Verdopplung der Periode der nicht-kollinearen magnetischen Ordnung nachweisen, die bisher in allein aus Manganat bestehenden Schichtstruktuern noch nicht beobachtet wurde. In diesem Zustand bilden die magnetischen Momente in den benachbarten ferromagnetischen Schichten einen Winkel α zueinander, was aus der Austauschwechselwirkung mit dem benachbarten A-Typ Antiferromagneten resultiert. Darüber hinaus zeigen wir, dass der Grad der Nicht-Kollinearität dieses Systems, ausgedrückt durch den Winkel α, durch die Anwendung kleiner Magnetfelder leicht eingestellt werden kann.

Abschließend geben wir einen Überblick über die Hydrierung von Übergangs-Metalloxiden, um die Perspektiven darzustellen, die sich durch die verschiedenen Kombinationen der in dieser Arbeit vorgestellten Methoden ergeben. Wir erläutern die strukturelle und elektronische Reaktion von Manganat- und Cuprat-Dünnschichten auf die Wasserstoffbeladung als Beispiel für das Potential der RNR-Methode auf dem Gebiet der H-Dotierung. Unsere Ergebnisse zeigen, dass Wasserstoff ein mächtiger Kontrollparameter in komplexen Dünnschicht-Systemen ist.

Acronyms

AF Antiferromagnet.

AMR Anisotropic magneto-resistance.

CMR Colossal magneto-resistance.

EB Exchange bias.

ERDA Elastic recoil detection analysis.

FM Ferromagnet.

FRM Forschungsreaktor München II.

GMR Giant magneto-resistance.

JMAK Johnson–Mehl–Avrami–Kolmogorov.

Kara Karlsruhe Research Accelerator.

MBE Molecular beam epitaxy.

ML Monolayer.

MR Magneto-resistance.

NR Neutron reflectometry.

NSF Non spin-flip.

PMA Perpendicular magnetic anisotropy.

PND Polarized neutron diffraction.

PNR Polarized neutron reflectometry.

RHEED Reflection high-energy electron diffraction.

RKKY Ruderman–Kittel–Kasuya–Yosida.

RMS Root mean square.

RNR Resonant neutron reflectometry.

SAF Synthetic antiferromagnet.

SF Spin-flip.

SIMS Secondary ion mass spectroscopy.

SL Superlattice.

SLD Scattering length density.

SQUID Superconducting quantum interference device.

TMO Transition metal oxide.

VSM Vibrating sample magnetometry.

XPS X-ray photoelectron spectroscopy.

XRD X-ray diffraction.

XRR X-ray reflectometry.

Chapter 1

Introduction

Thin films are at the basis of several modern technologies, including electronic and spintronic devices, sensors, coatings, energy production and batteries [1]. Due to their reduced dimensionality, which enhances the surface to bulk ratio, thin films exhibit high versatility for targeted modification of structural, electronic and magnetic properties. For example, large interfacial strains can be induced by tuning the lattice mismatch between substrate and thin film (Figure 1.1a). Alternatively, the chemical interdiffusion and charge transfer (Figure 1.1b), which naturally result from the vicinity of different atoms and charges, are key mechanisms widely used to tailor specific properties in heterostructures. Finally, the presence of uncompensated spins at the interface between two materials with different magnetic order (Figure 1.1c) can lead to various effects, such as competing interface exchange couplings and spin frustration. Thanks to these numerous degrees of freedom, a plethora of phenomena that have no analogue in bulk systems was discovered at the interface between two materials, and thin film heterostructures are the perfect platform to observe such interactions. A few examples of the rich physics of interfaces are exchange bias [2], proximity effects [3], interlayer exchange interactions [4], and controlled magnetic anisotropy [5, 6].

One powerful method to study thin films is polarized neutron reflectometry, which allows the reconstruction of depth dependent structural and magnetic profiles. This technique, in combination with other complementary methods, was the primary characterization tool used in this thesis, and is reviewed in Chapter 2. In

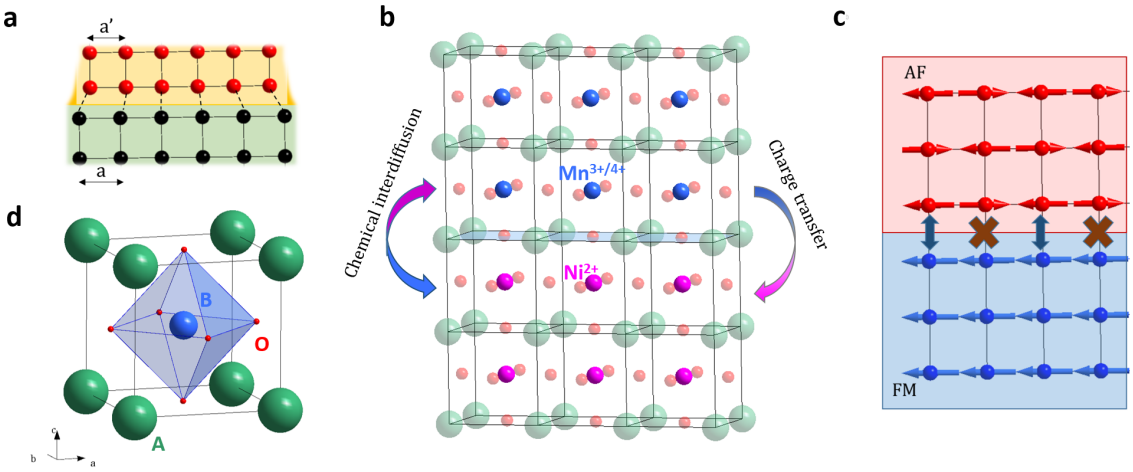

Figure 1.1: Properties of heterostructures interfaces. **a** Strain effect due to lattice mismatch with substrate; **b** Chemical and charge mismatch at the interface of different TMOs; **c** Uncompensated spins at the interface between a FM and AF materials, resulting in spin frustration; **d** Unit cell of the perovskite structure of formula ABO_3.

the following paragraphs, we will provide an introduction to the physical concepts and classes of materials of interest for my doctoral work. A particular focus is given to transition metal oxide thin film and heterostructures, which were central to our research of complex magnetism shown in Chapter 4. Following this, we will briefly show the foundations for hydrogen incorporation in solids and in thin films, with particular emphasis on conventional detection methods. This will prove useful for the discussion of the new method realized during my doctoral studies presented in Chapter 3. In addition, to propose potential candidates for our new RNR method, we will give an overview on hydrogen storage materials. We also review the rising field of H-doping of TMOs, which will be expanded with our own results in Chapter 5. Finally, an outline of the thesis is given.

1.1 Transition metal oxides heterostructures

Transition-metal oxides (TMOs) are a fascinating class of material that exhibit highly tunable electronic and magnetic properties, due to the intrinsic correlation

between d electrons and the subsequent entanglement of charge, spin and orbital degrees of freedom. Thanks to recent technical advancement in thin film growth techniques, it was possible to demonstrate unique interface phenomena in TMO-based heterostructures, such as the charge redistribution, orbital reconstruction and interface magnetic coupling driven by the orbital hybridization [7], which established them as an attractive platform for magnetic devices. We will give an overview over the underlying reasons of such an extremely rich physics, as well as highlighting some of the frontiers in this field with few selected examples.

In order to discuss the properties of TMOs we must first of all discuss their crystal structures, the most of common of which is the perovskite one. This structure, described by the basic stoichiometry ABO_3, sees the A-site cations at the corners of a cubic unit cell, with the transition metal B coordinated by 6 oxygen atoms (Figure 1.1d). This coordination results in a strong crystal field, in which the 5 degenerate d orbitals are split into three t_{2g} orbitals at lower energy, and two e_g orbitals at higher energy. The strongly directional character of these orbitals defines the possible overlap with the oxygen p orbitals, through which electrons can hop. According to the partial filling of the d band, reflected by the position of the transition metal in the periodic table, the electrons hence occupy these orbitals according to Pauli's exclusion principle and Hund's rules. Their hopping probability depends both on the orbital overlap and the strong on-site Coulomb interaction, giving rise to either metals or Mott insulators. In addition, the spin-orbit interactions, dominant in cases of heavier ($5d$) transition metals, can also modify the band structure and as a consequence the electronic properties. The result of all these competing interactions are first of all intriguing physical phenomena, such as metal-to-insulator transitions, high-temperature superconductivity, and colossal magnetoresistance [8]. Secondly, the interplay between these comparable energy scales is responsible for the high sensitivity of TMOs to external perturbations such as the strain from substrates, temperature, and electric and magnetic fields [7].

One of the basic strategies to tune the ground state of a TMO is via carrier doping. In contrast to semiconductors, many transition metals can adopt various valence states, which allows one to achieve much higher levels of doping. The most straightforward route to electron/hole doping of the transition metal is through aliovalent substitution of the A-site cation, for example Sr^{2+} in the place of La^{3+},

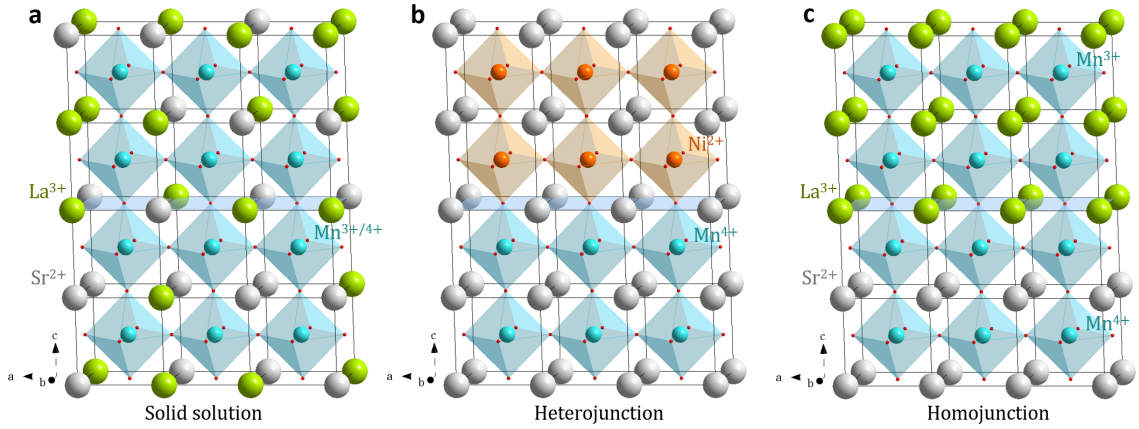

Figure 1.2: TMO doping schemes. **a**. Single $La_{1-x}Sr_xMnO_3$ film, showing random aliovalent substitution of the A-site and formation of a solid solution ; **b**. Example of heterojunction: $SrMnO_3/SrNiO_3$, with B-site substitution; **c** $LaMnO_3/SrMnO_3$ homojunction, showing ordered aliovalent substitution of the A-site.

schematically shown in Figure 1.2a. In the exemplary case of $LaMnO_3$, Sr substitution naturally leads to the change of oxidation state of Mn from 3+ to 4+, giving rise to a very rich phase diagram. The opposite outcome can be achieved through oxygen vacancies, which result in the reduction of transition metal valence. For example in $LaMnO_{2.5}$ the oxidation state of Mn is reduced from 3+ to 2+. The incorporation of H in TMOs can as well induce the reduction or oxidation of the transition metal, depending on the synthesis process and the subsequent formation of species as H^+ or H^-. In addition, the transition metal valence can as well be modified by the charge transfer arising from heterostructuring of TMOs.

In thin film heterostructures, the electronic configuration of the BO_6 network is finely tuned in two main ways: the first one is the stacking of different TMOs (B-site substitution or heterojunction), represented in Figure 1.2b. The charge transport between different transition metals, mediated by oxygen atoms, is proven to be a key player for the creation of magnetic states not attainable in single films or bulk. Some examples are superlattices made of optimally doped manganites combined with ruthenates [9, 10], nickelates [11] or cuprates [12–14]. In many cases, unexpected induced magnetism and electrical transport was observed at the interfaces of these materials, owing to orbital reconstructions and

charge transfer effects. In other cases, due to the inherent translational symmetry breaking of interfaces, additional phenomena can come into play, such as the exchange bias [15–18], controlled magnetic anisotropy [19, 20], proximity effects [21, 22], spontaneous magnetic reversal [23], and exchange springs [24]. Some of these properties have been proven to be particularly suitable for spintronics and magnetic data storage, such as electric field control of exchange bias in $La_{0.7}Sr_{0.3}MnO_3/BiFeO_3$ [25], and electrical tuning of magnetic tunnel junctions in $La_{0.7}Ca_{0.3}MnO_3/YBa_2Cu_3O_7/La_{0.7}Ca_{0.3}MnO_3$ [26].

Moving away from heterojunctions, an alternative way for adjusting electronic properties is by modulated doping. In this case we have a depth dependent A-site substitution, which gives rise to a so-called homojunction, as shown in Figure 1.2c. This doping scheme provides a depth modulated carrier concentration, with large carrier transfer between different sample regions. One of the most striking examples is the formation of a FM metal through stacking of two AF insulators such as $LaMnO_3$ and $SrMnO_3$ [27], thanks to the hole transfer between Mn^{3+} and Mn^{4+} ions. These homostructures have proven to be very similar to the solid solution single films of corresponding stoichiometry if the building blocks are thin enough. However, they can also give rise to phenomena which are unprecedented in single films, such as the enhanced magnetic ordering temperature [28], metal-insulator transition [29], interface high-temperature superconductivity [30], and the long range non collinear order that is presented in Chapter 4. Modulated doping homojunctions hence offer many possibilities to engineer new properties in any material with rich phase diagrams, such as cuprates, ruthenates, nickelates and other transition-metal oxides.

One of the specific goals of the field of oxide spintronics is the realization of tunable magnetic order. Materials with tunable magnetic order are at the basis of numerous technological innovations such as the hard disk drive, spin valves and magnetic random access memory. The control of the configuration of the magnetization in a parallel (P) or antiparallel (AP) way is the core concept for many of these applications, and was pioneered by the investigations of elemental metal multilayers [4, 31, 32]. The design of superstructures tunable between P and AP configuration of subsequent FM layers, the so-called synthetic antiferromagnets (SAFs), has since then become one of the most promising tracks in the emerg-

ing field of spintronics [33]. SAFs are on one hand easy to control thanks to the presence of FM layers, but at the same time, due to the antiparallel alignment between such layers, they show high stability and absence of magnetic stray fields, as a typical property of antiferromagnets (AFs). In recent years, an increasingly large share of research has focused on TMO-based SAFs, due to the many advantages offered by these materials, as explained in the previous paragraph. In the view of creating such oxides-SAFs, the design of the heterostructures aims to achieve tunable long-range magnetic configurations, which however are not trvial, due to their inherently short-ranged interactions. Nevertheless, by selecting FM and spacers of distinct nature, it was possible to tune different long-range exchange interactions, such as the Ruderman–Kittel–Kasuya–Yosida interaction (RKKY) for metallic spacers [34, 35], spin polarized tunnelling for insulating ones [36, 37], or dimensionality induced antiferromagnetic coupling for insulating FM and metallic spacer [38].

A special case is constituted by superlattices (SLs) in which the spacer shows AF or spiral magnetic order. In this case, as addressed by Slonczewski [39], we have to expect a non-collinear orientation (meaning neither parallel or antiparallel) of the magnetization of FM layers as a result of the competing interactions at play: the long-range coupling between FMs and the interface exchange coupling between FM and spacer. One example is the highly non-collinear magnetic structure obtained in $LaNiO_3/La_{2/3}Sr_{1/3}MnO_3$ SLs, where the magnetic spiral in $LaNiO_3$ spacer was reported to be fundamental for the global magnetization observed [11]. In this system consecutive FM manganite layers align at an angle $\pm\alpha$ with respect to the applied magnetic field. Such a heterostructure may be advantageous for the implementation of correlated oxides in spintronics applications, as shown with a tunable resistive noncollinear magnetic memory device [40], where the authors showed how to tune the coupling angle α between $\approx 180°$ (SAF) and lower values (non-collinear).

Other uses of the non-collinearity can be found in particular spintronics applications [41], such as artificial neural networks [42], and triplet spin valves [43, 44]. Specifically, TMO-based heterostructures have already shown interesting proximity effects [45–47], including first indications of triplet currents [48–50]. Junctions composed of high temperature superconductors and tuneable non-collinear mag-

netic spacers hence offer great potential to realize long-range spin-triplet current formation and propagation.

1.2 Hydrogen in solids

One of the core topics of my doctoral studies revolved around the detection of hydrogen absorbed in thin films, through the novel method of resonant neutron reflectometry. In order to better understand the method and the challenges it poses, we give here a brief overview over various hydrogen incorporation mechanisms into different classes of materials. Hydrogen is the first element of the periodic table and is normally found in nature in the form of H_2 gas, with a strong covalent bond between the two atoms. This gas molecule in contact with catalyst materials, such as Pt and Pd, is split into two atomic H^0. It is also possible to attain ionic hydrogen through the splitting of specific compounds, such as acids, obtaining H^+ or hydrides such as CaH_2, obtaining H^-. Depending on the species of hydrogen, it can be absorbed in materials either via surface adsorption [51], interstitial physisorption, or chemisorption [52], with increasingly strong bonding to the host matrix. Atomic hydrogen in particular can be absorbed in ordered solids at many different sites. The most energetically favourable positions are those where extended defects such as dislocations or grain boundaries are found, for example in polycrystalline materials. Moreover, hydrogen can occupy point defects such as vacancies. Finally, it can be absorbed at interstitial sites, a process that can result in various distortion of the host lattice. For example, for many transition metals it is possible to obtain a solid solution with hydrogen occupying interstitial positions with a non-fixed stoichiometry. The main questions to answer when studying hydrogen in solids are hence: is the hydrogen being incorporated charged or neutral, what kind of interaction links hydrogen to the host, and where is hydrogen placed once inside the structure.

Solid-state hydrogen storage

The importance of hydrogen in solids spans several branches of material science and physics. First of all, we must mention the key role of hydrogen for green

energy production and storage. The challenge to reduce our carbon footprint has become impelling during the last decades. Within the grand challenges that the scientific community has been asked to uptake, we find the transition from fossil fuels to green sources of energy. In this regard, research on fuel cells [53], photocatalysts [54] and fusion reactors [55] is of primary importance. All of these technologies require a deep understanding of the impact of hydrogen on the constituent materials. In the transportation field in particular, the main idea is to use hydrogen as a fuel instead of gasoline, with the use of fuel cells [56]. The advantages for such technologies are numerous, such as having water as combustion product instead of CO_2, and the comparatively easy production of H_2 gas. However, one of the biggest drawbacks that prevents widespread acceptance of H-fuelled vehicles is the storage of H_2 gas. Many solutions have been proposed, such as high pressure containers, liquefied hydrogen, and solid-state storage. With regard to this last category, the aim is to develop specific materials that can uptake and release large amounts of H at ambient pressure and temperature. The advantage of using solid-state storage materials is that they are chemically stable, of easy transport, ideally not toxic and not dangerous. However most of the storage materials nowadays used have a low mass storage density [57]. For this reason, scientists have spent many years to search for new materials that are light and can uptake high H quantities and release it quickly and in a controllable way, where the control parameters are temperature, pressure, and electric current [58]. We will give a short introduction to the most significant classes of hydrogen storage materials, but a detailed review of the state-of-the-art solid state storage technologies and their characteristics compared to cryogenic or compressed H_2 storage can be found in Ref. [59].

One classification of storage materials can be made through the absorption mechanism. Exemplary storage materials where atomic or molecular hydrogen is physically adsorbed into cavities and channels range from zeolites (alluminosilicates with typical pore size of a few Ångstroms), to metallorganic frameworks (MOFs) and carbon-based materials, such as carbon nanotubes, with pore size in the nanometers range. Typical chemical storage materials are ammonia, metal, and complex metal hydrides [59], where the hydrogen is chemically bound to one or more atomic species.

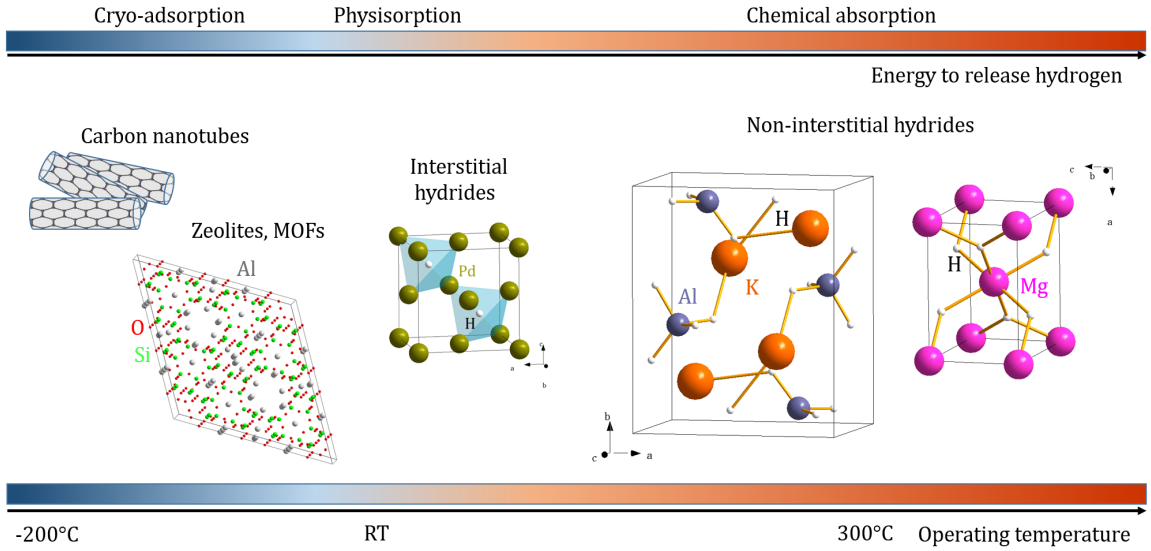

Figure 1.3: Comparison of hydrogen storage material classes versus their operating temperature and energy needed to release H_2.

A further subdivision of metal hydrides is done according to the position that the hydrogen occupies in the host crystal lattice, forming either an interstitial and non-interstitial hydride. In the first family we find all transition metal hydrides, in which the hydrogen is not strongly bound, is highly mobile, and does not have a fixed stoichiometry. On the contrary, in non-interstitial hydrides the absorption of hydrogen modifies the host crystal structure with formation of new ionic or covalent bonds involving hydrogen. A brief review of the most recent and promising candidates in both categories can be found in [60].

To compare different storage solutions we have to look primarily at the absorption weight capacity, which however for most solid-state materials is still far below the values obtained with cryogenic and compressed hydrogen, but also at the temperature of operation and energy needed to release hydrogen. Ideally the perfect solid-state storage can uptake high amounts of hydrogen and release them at room temperature with the minimum energy required. Figure 1.3 shows a comparison of the different candidate classes of materials in terms of operating temperature and energy consumption. Chemical storage is generally more stable than physical adsorption, however it also requires higher energy to break the strong chemical

bonds formed and release hydrogen, for this reason non-interstitial hydrides like alanates and Mg-hydrides are found on the right hand side. On the left side, we find materials that rely on surface adsorption, which often have to be cooled down to cryogenic temperature to prevent the spontaneous evaporation of hydrogen gas. Interstitial hydrides, which rely on physi- and/or chemisorption, are found in the intermediate region, close to the target operating temperature [61].

One difficulty encountered in this long-standing search for the perfect storage is the detection and quantification of H atoms/molecules in these materials. Most studies take advantage of gravimetric and volumetric measurements, which suffer from sensitivity limitations and are applicable only to certain classes of materials [62]. A large amount of research is taking place as well on nanomaterials and in particular in thin films [63], where the low dimensionality together with high homogeneity of lateral physical properties allowed strong improvements in this field of research [64]. For thin films, x-ray and neutron scattering techniques are widely used, since they allow good sensitivity and spatial resolution, but can be time-consuming. In this sense an improvement of such methods, as our proposed resonant neutron reflectometry (RNR), is fundamental to the research of new solid-state storage materials.

Alternative techniques for H detection in thin films.

Many different methods are nowadays available to study hydrogen absorption in thin films. Here we will give a short review of the most commonly used ones, to allow for a clear comparison with the RNR method proposed in Chapter 3.1. First of all we should mention indirect methods such as resistivity measurement [65] or change of optical properties [66], which can indeed be used to track H absorption but still require the comparison with a direct technique to calibrate the actual H concentration. Another technique that requires calibration is secondary ion mass spectrometry (SIMS). In this case an ion beam is used to remove via sputtering the atoms from the surface, which are then collected and analyzed through a mass spectrometer. This technique is extremely sensitive to hydrogen and its isotopes (down to ppm) [67], and can also discriminate between chemi- and physisorbed states [68], however it is a destructive technique. One example of direct methods

is Elastic Recoil Detection Analysis (ERDA) [69]. ERDA is a technique similar to Rutherford backscattering spectrometry, in which an ion beam is directed at the target material. The nuclei which have a mass equal or lower to that of the projectile are recoiled outside of the sample and are then analysed. This allows one to detect small concentrations of hydrogen down to 0.1 at.% in micrometer-thick films. For sub-μm films X-ray (XRR) or neutron (NR) reflectometry can be used [70]. Both methods measure the reflectivity of a surface under small incident angles (in the order of 1°), which depends on the contrast of scattering length density (SLD) ρ normal to the surface. For a single layer composed of different types of atoms, the SLD can be written as $\rho = \bar{N} \sum b_i c_i$, where $\bar{N}$ is the averaged atomic density of the layer, b_i and c_i are the scattering length and the concentration of each i-th type of atoms, respectively. The X-rays scatter on electrons and, hence, the scattering length b_i depends linearly on the atomic number of the i-th atom. In this sense hydrogen, with its one electron, is almost invisible to XRR, especially in a matrix of heavier atoms. Nonetheless, XRR has been mostly used together with x-ray diffraction (XRD), to study lattice expansion upon absorption of hydrogen [71, 72]. These methods are however once again indirect, as they require to know the correlation between the lattice parameter and hydrogen concentration.

NR on the other hand is particularly suited to study directly hydrogen in thin films due to its negative scattering length $b_H = -3.74$ fm, which guarantees a good contrast with the majority of other elements and compounds. This means that the presence of hydrogen in a system will significantly affect its SLD and hence change the neutron reflectivity. For this reason conventional NR was widely used for the study of hydrogen uptake in various single film systems [73, 74], as well as in superlattices such as Fe/Nb, Fe/V [74, 75]. In many cases the periodic structures were used to enhance the sensitivity at the position of the Bragg peaks [76]. Nevertheless, even conventional neutron reflectometry has some limitations, as the need of fitting the data to determine physical parameters such as ρ and thickness d, and the possibility to study kinetics of absorption only if this is slow enough (or easy to stop) to allow the measurement of a full (or partial) reflectivity curve. Moreover for small hydrogen concentrations, below 10 at.%, the thickness changes can be very small, as well as the contrast induced by the absorption of

hydrogen, meaning a hard determination of the exact hydrogen concentration. The method presented in the following chapters shows how to reach a higher sensitivity ($\sim$ 1 at.%) simultaneously with shorter measurement times (down to $\sim$ 20 s per measurement point), offering the possibility to have insight into faster absorption processes.

1.3 Hydrogen in complex oxides

The bridge between correlated materials such as TMOs and hydrogen in solids is found in the emerging field of hydrogen (or proton) doping. The central idea is to inject H atoms or ions in a host material to change its physical (especially electronic) properties. This idea is not completely new. In fact, several publications in the late 90s and early 2000s had shown the possibility to use H to tune the exchange coupling in thin film heterostructures [77–80].

Recently, this concept has been revived and extended to new materials. For example in all-solid-state magneto-ionic devices it was shown that H is able to tune the magnetic anisotropy of a thin layer [81–83], which can be used as a building block for voltage-controlled spin(-orbit)tronics. The impact of H on the physical properties of thin films, such as the electrical resistance and spin Hall effects, allowed as well for substantial advancements in hydrogen gas sensing devices [84–86].

Moving from heterostructures composed of simple metals and binary oxides to more complex materials, Cui et al. [87] showed that H intercalation in iron-based superconductors is responsible for a significant increase of the superconducting transition temperature, T_c. Typically, a small concentration of hydrogen absorbed can be sufficient to significantly change the physical properties of the host.

Proton doping is a blossoming field as well in correlated perovskite oxides. Shi et al. [88] showed a colossal resistance switching effect (with a variation of almost 7 orders of magnitude) in perovskite nickelates controlled by hydrogen absorption and desorption, as shown in the scheme in Figure 1.4. Here the authors showed that gaseous hydrogen is able to penetrate the perovskite structure through splitting at the Pt catalyst bars (Figure 1.4a,b). A metal to insulator transition is observed due to the charge transfer from interstitial H to the rare-earth nickelate. This results

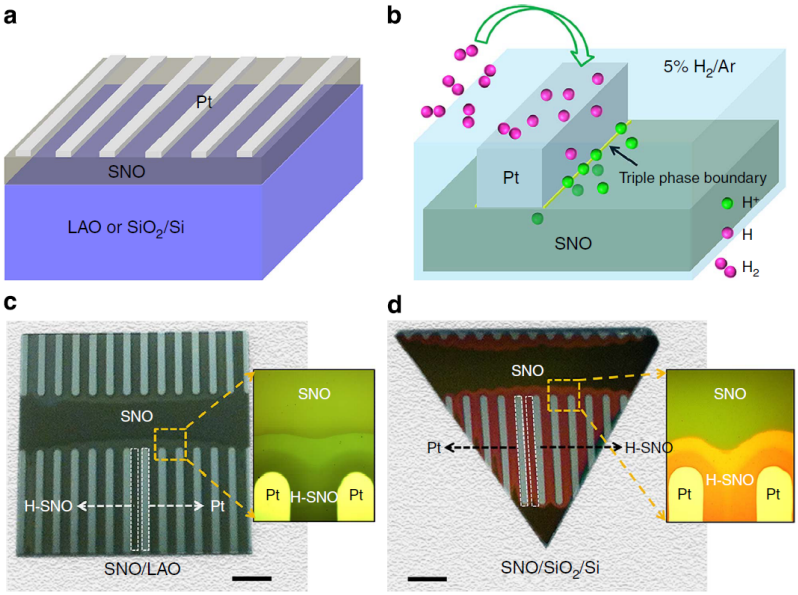

Figure 1.4: Example of H intercalation process in rare-earth nickelate, reproduced from [88]. **a**. Scheme of sample design; **b**.Schematic illustration of the H intercalation process at various interface sites; **c**. Photo of hydrogenated sample on LAO substrate, showing the different optical properties of H-SNO; **d**.Photo of hydrogenated sample on SiO_2/Si substrate, showing the change of optical properties of H-SNO. Scale bars on the last two panels are of 2 mm, insets show a zoom around a Pt bar.

in an effective electron doping, with subsequent change of optical properties from dark grey to translucent in the regions close to the catalyst (Figure 1.4c,d). A similar effect was already used for the design of tunable neural networks, where the synapses are programmed by a gating voltage charging or discharging a thin conductive nickelate layer with hydrogen to modify its resistivity [89]. Also in nickelates, the recent discovery of superconductivity in topotactic layers, obtained after annealing in strongly reducting conditions (with CaH_2 or NaH_2), has brought to attention the role of residual H and its impact on the structure, which are still open questions for the community [90, 91].

Other works have shown the possibility to intercalate H in various perovskites including titanates, cobaltates and manganites [92, 93]. In manganites in particular two publications [94, 95] have shown a metal to insulator transition for

optimally doped $La_{1-x}Sr_xMnO_3$ (LSMO) annealed in hydrogen atmosphere, which is reversible upon annealing in different atmospheres. However they report contradicting results concerning the doping mechanism, claiming the intercalation of hydrogen atoms to form oxihydride phase in one case and a topotactic reduction similar to that observed in nickelates in the other case. This is only one of many examples showing the importance of PNR and RNR studies, which provide absolute and depth resolved hydrogen concentrations and the related magnetic moments.

1.4 Structure of the thesis

This thesis is organized as follows:

Chapter 2: Experimental methods First of all we will introduce the main experimental methods used in this work, namely neutron and x-ray reflectometry. We will describe the interaction of neutrons and x-rays with matter and describe the typical reflectometry scattering geometry. We will then proceed to describe in details the principles of polarized neutron reflectometry, resonant reflectometry and the technical details of the instruments used. Finally, we give a brief description of the additional characterization methods used, including SQUID magnetometry, x-ray and neutron diffraction and electrical transport.

Chapter 3: Resonant neutron reflectometry for hydrogen detection in thin films In this Chapter, we show the foundation for the RNR method. We start by defining the relation that relates hydrogen content to the resonance position. The method is based on the formation of neutron resonators, or waveguides, through specific sample design, reviewed in details in Section 2.1.2. The strong resonance peak is a direct indication of the optical potential of the sample, and its shift is directly proportional to the hydrogen content. We then describe the realization of a proof-of-principle experiment, in which hydrogen incorporation in niobium thin layers is detected *in situ*. We show that a sensitivity of 1 atomic % was reached with a counting time of tens of seconds. We then proceed with a direct comparison with other neutron and nuclear methods. In the second part of this chapter, we show the application of the RNR method to study the kinet-

ics of hydrogen absorption in niobium versus gas pressure, sample thickness and crystallinity. The absorption of hydrogen at room temperature is an irreversible process that destroys the superconductivity in niobium, indicating a substantial modification of electronic properties in the hydride phase. We observed that the kinetics of hydrogenation of niobium depends linearly on the sample thickness, is faster for polycrystalline samples, and is exponentially faster for higher gas pressures. By using simultaneous RNR and XRR measurements we unveiled two separate absorption mechanisms, detected via the two different probes -x-rays and neutrons- thus showing the importance of using both complementary techniques.

Chapter 4: Modulated doping of complex oxide films Here, we show the synthesis and characterization of LSMO homojunctions. The samples are produced via epitaxial stacking of a ten times repeated bilayer composed of 9 monolayers of optimally doped LSMO(x=0.4) and a varying thickness of overdoped LSMO(x=0.8). The preliminary characterization of the superlattices via x-ray reflectometry, magnetometry and electrical transport are shown. The structural and magnetic depth profile of the samples, obtained from PNR measurements is described. These homojunctions are characterized by a gradual depth-dependent hole-doping, caused by Sr-interduffusion and large charge transfer, which allows the tuning of magnetic properties of the whole structure. The spacer magnetic properties are shown to vary from FM, to A-type AFM and to C-type AFM. In particular, at intermediate spacer thickness, PNR reveals superstructure reflections indicative of an emergent periodicity twice as large as the superlattice unit cell. This corresponds to a non-collinear structure with a fan-like arrangement of magnetic moments that is highly susceptible to external magnetic fields and can be regarded as a synthetic antiferromagnet (SAF). The dependence of long-range non-collinear ordering versus temperature, magnetic field and spacer thickness is described, and its possible origins are discussed. Finally, we present a preliminary device operation utilizing this newly found non-collinear phase.

Chapter 5: Proton doping of complex oxide films In Chapter 4, we show our preliminary results on hydrogen doping of TMO thin films. The first case is given by hydrogenation of LSMO(x=0.5), indicating intercalation of H atoms at

room temperature. The magnetoresistance and metallicity of the layers is successfully modified upon hydrogen loading. Additional magnetometry and PNR measurements indicate an increased magnetic moment after hydrogenations, hinting on possible oxygen reduction. The second example is given by hydrogenation of cuprate layers, which showed an increased superconducting transition temperature after hydrogen exposure. The characterization of the films via XRR and XRD indicates an expansion of the c-axis of the single layer cuprate upon hydrogen absorption.

Conclusions and outlook In this chapter we provide a brief outlook and perspectives which would be interesting to explore in view of the results presented in this thesis. The RNR method opens the door to kinetics studies on thin films which were not possible before. For example new candidate storage materials could be tested for fast absorption and desorption processes, while knowing at the same time the exact hydrogen content. Also in the field of H-doping, RNR could be of particular importance. Specifically, thanks to the use of polarized neutrons, it could be a powerful method to link the hydrogen content to changes in magnetic properties of a thin layer.

Chapter 2

Experimental methods

This section provides a general overview of the experimental methods used. The principal scattering techniques used, neutron and x-ray reflectometry, and their characteristics are discussed [96]. The experimental setup of the reflectometry measurements shown is briefly described. Specifically, polarized neutron reflectometry and its experimental geometry are defined. A short review on the principle of neutron waveguides, or resonant reflectometry is given. Finally other preliminary characterization techniques used such as SQUID magnetometry, electrical transport setup and x-ray diffraction are discussed.

2.1 Neutron and x-ray reflectometry

Reflectometry is a well known method for the characterization of thin films. It allows the study of depth dependent physical properties, such as chemical composition, atomic density, and interface and surface roughness of single or multi-layer systems. The basic principle of this technique is the reflection and refraction of radiation at a flat surface. As in the case of visible light and water, if the angle of incident radiation is below a certain threshold, known as the critical edge or θ_c, the incoming radiation is entirely reflected on the surface (total reflection). Above this angle, part of the radiation penetrates into the material, interacting with it. The ratio between the incoming and reflected intensity at different scanning angles, or reflectivity curve, is a result of interference phenomena and encodes, in

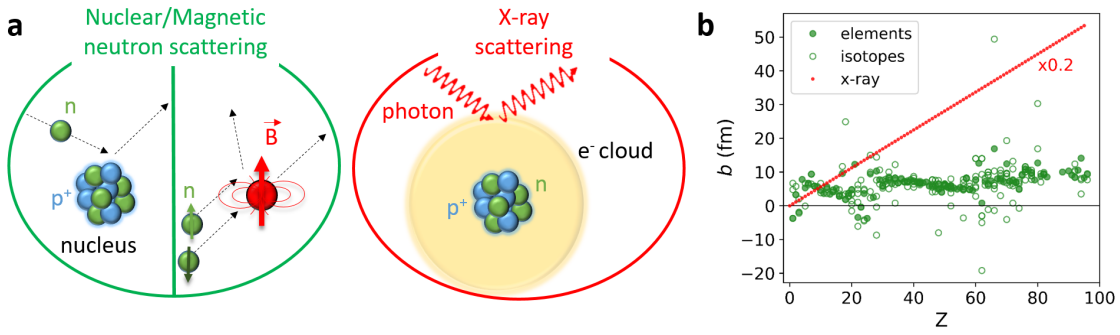

Figure 2.1: Principles of neutron and x-ray interaction with matter. **a** Simplified representation of neutron and x-ray scattering mechanism, adapted from [96]; **b** variation of neutron (green) and x-ray (red) scattering lengths for different elements versus atomic number Z. For neutrons the scattering length of the element weighted by natural abundance (filled symbols) and the specific isotopes (empty symbols) are shown.

a well studied and understood way, the information about the sample thickness, optical potential and waviness. The depth profiles are hence normally obtained by fitting model-based simulations to the measured reflectivity. In the following paragraphs, the classic formalism linking the reflectivity to the sample properties is introduced.

The optical potential of a layer composed of i atoms is normally defined as the weighted average of scattering lengths of each atom b_i multiplied by the number density $\bar{N}$, or scattering length density ρ (SLD):

$$\rho = \bar{N} \sum b_i c_i. \tag{2.1}$$

The type of interaction between radiation and matter is encoded in the scattering length b and depends on the nature of the probe. Neutrons are scattered by nuclei, while x-rays interact with electronic clouds, as represented in Figure 2.1a. As a consequence, away from resonant conditions, the scattering length of different elements of the periodic table increases with the atomic number for x-rays, while it has a non-monotonous behaviour for neutrons (Figure2.1b). This is an important aspect of complementarity between x-rays and neutron scattering techniques, since the optical contrast between two materials can greatly differ when using one or the

other probe. For example it is very difficult to detect light elements in a heavy element matrix with x-ray scattering, while that is not necessarily true for neutrons. While the majority of elements still has a positive scattering length for neutrons, hydrogen and lithium have a negative b (Figure 2.1c), meaning high contrast and high sensitivity to such atoms. Another advantage of neutrons is the possibility to distinguish between elements that are neighbours on the periodic table, such for example manganese and iron, given the non-trivial dependence of b on the atomic number. Moreover, neutrons can differentiate between different isotopes, allowing for labelling procedures that are essential both in biological [97, 98] and material [99] sciences. On the other hand x-rays are much more sensitive to heavy metals. High flux x-ray beams are also more easily produced, which is important when studying samples with small volume, such as thin films. Finally x-ray scattering becomes element-specific when particular wavelengths, associated with the absorption edges of atoms, are used, such as in the case of resonant x-ray scattering. While the two probes interact with matter in a profoundly different way, the geometry and the optics of reflectometry remain the same both for neutrons and x-rays.

In a typical experiment the intensity of the reflected beam $R(Q)$, defined as the ratio between outgoing and incoming beam intensity, is scanned while varying the momentum transfer Q [100]. If we take into account flat surfaces with properties varying only along z, the specular condition is satisfied for $\theta{=}\theta_{in}{=}\theta_{out}$, meaning that only the component normal to the film surface Q_z is non-zero and is defined, as shown in Figure 2.2a, as follows:

$$Q_z = \frac{4\pi}{\lambda}\sin(\theta) = 2k_0 \tag{2.2}$$

with k_0 the neutron or x-ray component of the wavevector $k = 2\pi/\lambda$ perpendicular to the surface in vacuum. On the other hand if we consider in-plane features such as correlated roughness, density inhomogeneities, domains, and surface morphologies, diffuse scattering can arise, with non-zero components at Q_x and Q_y [101]. In the following sections we will mostly focus on specular reflectivity, which was the primary tool used in this work for thin film characterization.

Let us consider a multilayered system composed by a periodic stacking of two

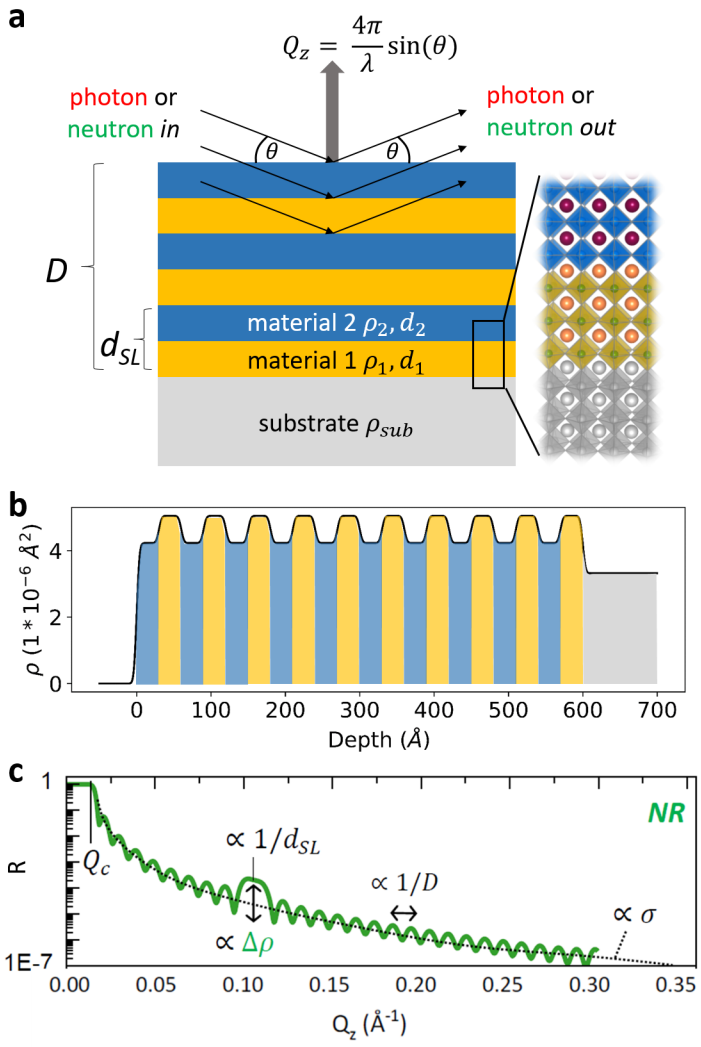

Figure 2.2: Basic principle of reflectometry adapted from [96]. **a** Definition of scattering geometry and schematics of a layered thin film heterostructure; **b** Depth profile of the neutron scattering length density for a $SrVO_3/SrCrO_3$ superlattice; **c** Simulated neutron reflectivity curve for the heterostructure described in Panel b.

different materials on top of a substrate, as schematically represented in Figure 2.2a. Each layer is characterized by a scattering length density ρ, thickness d and roughness σ. For example we can consider a $SrVO_3$(30Å)/$SrCrO_3$(30Å) bilayer repeated 10 times on top of $SrTiO_3$ substrate, with all interfaces characterized by a roughness of 3 Å. The vanadate is represented in blue, the chromate in yellow and substrate in grey. The corresponding reflectivity curve is simulated in Figure 2.2c, as the numerical solution of a Schroedinger equation of the form:

$$\frac{\hbar^2}{2m}\Delta\Psi + V(z)\Psi = \epsilon\Psi \tag{2.3}$$

where the first term corresponds to the neutron kinetic energy, with m and $\hbar^2$ the neutron mass and the Planck constant, respectively, Ψ the neutron wavefunction and ϵ the eigenvalues. The second term indicates the depth dependent potential energy seen by the neutron, which corresponds to the depth dependent optical potential of the system ρ(z), as defined in Eq.2.1. The ρ(z) for neutrons for the example structure is shown in Figure 2.2b, with high SLD at the chromate depth and low SLD at the vanadate depth.

The Schroedinger equation has been solved both analytically and numerically [102, 103], however a simple expression can be derived from the Born approximation:

$$R(Q) \approx \left| \frac{1}{Q^2} \int \frac{\partial\rho(z)}{\partial z} e^{-iQz} dz \right|^2 . \tag{2.4}$$

Equation (2.4) shows that the reflectivity is a measure of the summed gradients of optical potential along z.

Qualitatively we can describe the general features of a reflectivity curve. Below Q_c the total reflection condition holds, hence we observe a plateau in the reflectivity with R=1. Above Q_c the beam penetrates into the material, giving rise to a series of interference phenomena [104, 105]. The most prominent are the typical oscillations, called Kiessig fringes, whose period is $2\pi/D$, where D is the total thickness of the layers under study. In addition, if there is a scattering contrast $\Delta\rho$ between material 1 and 2, as in the example shown, we will observe the emergence of a superlattice Bragg peak at Q=$2\pi/d_{SL}$.

2.1.1 Polarized neutron reflectometry

An important difference between the x-rays and neutrons is the spin $\frac{1}{2}$ and the related magnetic moment of the latter, which allows the scattering of neutrons on magnetic moments present in the material under study. In this case the Schrödinger equation is represented in the basis of a spinor wavefunction of the form:

$$\Psi = \begin{pmatrix} \Psi^+ \\ \Psi^- \end{pmatrix}, \tag{2.5}$$

where Ψ^+ and Ψ^- are the two spin states. A more general optical potential for neutrons including the magnetic interaction can be written as:

$$V(x) = 4\pi\rho = 4\pi\rho_n + c\sigma B \tag{2.6}$$

Here we clearly distinguish two contribuitions: a nuclear ρ_n, defined previously in Eq.(2.1) and a magnetic one. The magnetic contribution is given by the scalar product between the magnetic induction in a medium B, and the Pauli matrix σ, multiplied by the scaling factor c:

$$c = \frac{2m}{\hbar^2}\mu_n = 0.23 \times 10^{-6}\ \mathrm{kG^{-1}\AA^{-2}} \tag{2.7}$$

with the neutron mass m and the neutron magnetic moment μ_n. The scalar product σB in spherical coordinates has the form:

$$\sigma B = |B| \begin{pmatrix} \cos\chi & \sin\chi \cdot \exp(-i\phi) \\ \sin\chi \cdot \exp(i\phi) & -\cos\chi \end{pmatrix} \tag{2.8}$$

where χ is the polar and ϕ the azimuthal coordinate, respectively, defined with respect to the direction of the external field H. In the simple and most common case, H is applied in the film plane, hence χ is the in-plane projection of the angle between M and H, while ϕ is the out-of-plane projection. As the magnetic induction B (with $B = H + 4\pi M$) along the out-of-plane direction z is continuous, it does not give rise to magnetic contrast [106]. As a result, the z components of magnetization are effectively invisible in a polarized neutron reflectometry (PNR)

measurement.

Now we can consider the two simplest cases of magnetization M, shown as green arrows in Figure 2.3, parallel and perpendicular to the external field H. When $M \parallel H$ (collinear case) the scalar product is simplified to have only diagonal elements that are non-zero ($B_{\parallel}$), while for $M \perp H$ (non-collinear case) only off-diagonal elements are left ($B_{\perp}$). By plugging the so-defined potential in the vectorial Schrödinger equation, one can show that the neutron wavefunction will retain its spin state in the first case, while it will change it in the second. This results in the respective non spin flip (NSF) and spin flip (SF) scattering.

In order to analyse these separate channels, PNR utilizes a combination of a polarizer, spin-flippers and an analyzer. The polarizer and analyzer transmit only one spin state (up + or down −) with respect to the quantization axis, defined by the external field H. The spin flippers either transmit or invert the spin state. This setup (Figure 2.7) allows one to detect 4 different reflectivities that are defined by the direction of neutron spin before and after the interaction with the sample: two NSF channels R^{++} and R^{--}, and two SF channels R^{+-} and R^{-+}. All the channels are schematically represented in Figure 2.3, where the coordinates of the experiment are also shown. We defined the x direction as the one parallel to H and y as the direction parallel to the neutron beam.

A simple model is presented for each of these reflectivities, while a more detailed mathematical derivation can be found in [106, 107]. By combining Eq. (2.4) and Eq. (2.6) once can show that the amplitude of the NSF scattering $r^{\pm\pm}(Q)$, with $R^{\pm\pm}(Q) = \left|r^{\pm\pm}(Q)\right|^2$, corresponds in the Born approximation to:

$$r^{\pm\pm}(Q) \approx \frac{1}{Q^2} \int \frac{\partial}{\partial z}[4\pi\rho_n(z) \pm \frac{2m}{\hbar^2}\mu_n B_{\parallel}(z)]e^{-iQz}dz \tag{2.9}$$

From Eq. (2.9) we can see that the NSF scattering amplitude corresponds to the sum or difference of Fourier transform of the gradients of the nuclear and magnetic profile. For cases in which $\rho_n(z) >> B(z)$, it is a common practice to use the spin-asymmetry S_{asy} to separate the purely magnetic scattering:

$$S_{asy} = (R^{++} - R^{--})/(R^{++} + R^{--}). \tag{2.10}$$

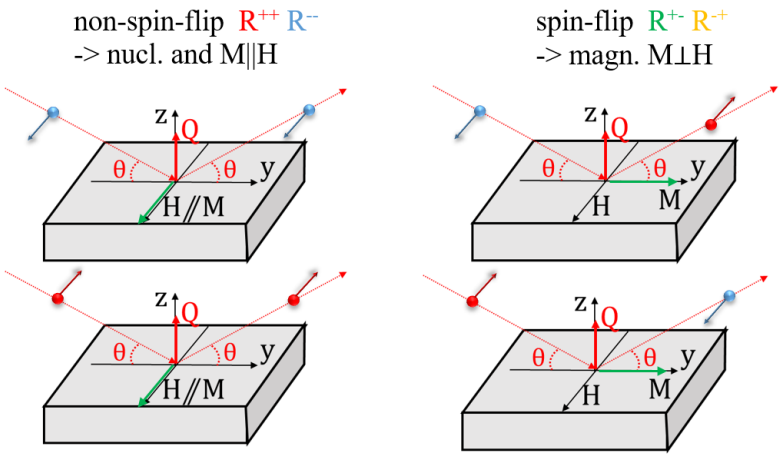

Figure 2.3: Polarized neutron reflectometry scheme, with definition of experimental geometry and the various polarization channels.

It can be shown that this quantity is proportional to the component of magnetic induction parallel to the neutron polarization vector, $B_{\parallel}$. The orthogonal component of magnetic induction $B_{\perp}$ is retrieved from the measurement of SF reflectivity. In fact, the SF scattering amplitude can be calculated in the Distorted Born Wave Approximation as:

$$r^{\pm\mp}(Q) \approx \frac{2m}{\hbar^2 Q}\mu_n \int (\Psi^{\pm})^* B_{\perp}(z)(\Psi^{\mp})dz. \tag{2.11}$$

Eq. (2.11) shows that the SF scattering has a purely magnetic nature, however its intensity can be modulated by the nuclear potential.

To summarize, these equations show how the combination of SF and NSF reflectivity profiles encodes the depth dependence of the nuclear potential, of the magnetic potential and of the component of magnetic induction vector projected on the film surface plane. Non-magnetic scattering is detected in the NSF channels, magnetic scattering from moments aligned parallel to the external field (collinear moments) is detected in the spin asymmetry S_{asy}, and non-collinear moments are detected in the SF channels. For this reason PNR has been a central characterization method for several systems, unveiling a number of magnetic phenomena such as exchange springs, perpendicular exchange bias, magnetic proximity effect, and

magnetic diluted layers [106].

2.1.2 Resonant neutron reflectometry

One of the main drawbacks of neutron reflectometry and neutron scattering in general is the low flux of incoming radiation produced with respect to x-rays. It is possible to partially overcome this limit with the use of neutron resonances or waveguides. The general idea is that to enhance the effective interaction of neutrons and sample by "trapping" them in standing waves at specific depths thanks to particular scattering depth profiles. Here the principles supporting the formation of neutron resonances are presented, summarized from the seminal work of Radu and Ignatovich in Ref. [108].

Let us consider a three layer potential, consisting of a substrate, a central layer and a capping layer, all characterized by the corresponding SLD ρ_i and thickness d_i. The amplitude of the neutron wavefunction Ψ in the central layer can be written as:

$$\Psi = \frac{t * e^{ik_1 d_1}}{1 - r_{21} r_{23} e^{2ik_2 d_2}} \tag{2.12}$$

Here t is the amplitude of neutron transmission through the capping layer and r_{ij} are the Fresnel amplitudes of a single reflection at the interface between two consecutive layers i and j:

$$r_{ij} = \frac{k_i - k_j}{k_i + k_j} \tag{2.13}$$

with k_i the normal component of the wavevector in the i-th layer:

$$k_i = (k_0^2 - \rho_i)^{1/2}. \tag{2.14}$$

We define resonant enhancement as an increase of neutron wave density $|\Psi|^2$ of at least 4 times compared to the incoming neutron field. The neutron density can be quantified numerically, by finding once again the solution to the Schroedinger equation with wavefunction Ψ, potential energy given by $\rho(z)$ and appropriate boundary conditions [109, 110]. This allows us to simulate the resonant neutron field versus depth and thickness. However before moving to the simulations, we can define the general requirements underlying waveguide formation.

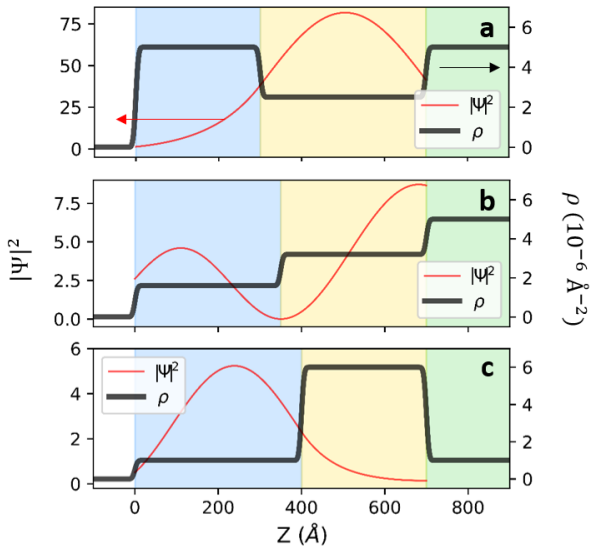

Figure 2.4: Different SLD designs to obtain resonant enhancement in a simple bilayer sample composed of capping layer (blue area), middle layer (yellow), and substrate (green). Black lines indicate the scattering length density profile for **(a)** a potential well, **(b)** a potential staircase, and **(c)** a potential step. The red line indicates the neutron density enhancement with incoming beam Ψ^2=1 versus depth for different sample design.

Sample design for resonance formation

From expression (2.12) one can show that the amplitude of the neutron wavefunction can be resonantly enhanced in the following conditions:

$$\begin{cases} |r_{23}| = |r_{21}| = 1 & \text{(2.15a)} \\ \arg(r_{21}) + \arg(r_{23}) + 2\mathrm{Re}(k_2)d_2 = 2\pi n. & \text{(2.15b)} \end{cases}$$

The condition (2.15a) calls for the resonance to be in the vicinity of the critical edge. In order to satisfy this condition, following Eq.(2.13), a strong ρ gradient must be existing at both interfaces around the central layer. SLD designs that realize such contrast are schematically represented in Figure 2.4. The first example in Figure 2.4a shows a potential well, created by encapsulating the layer of interest between a capping layer and a substrate with $\rho_1 \sim \rho_3 > \rho_2$. A standing wave is created from constructive interference of reflections at the interfaces around the

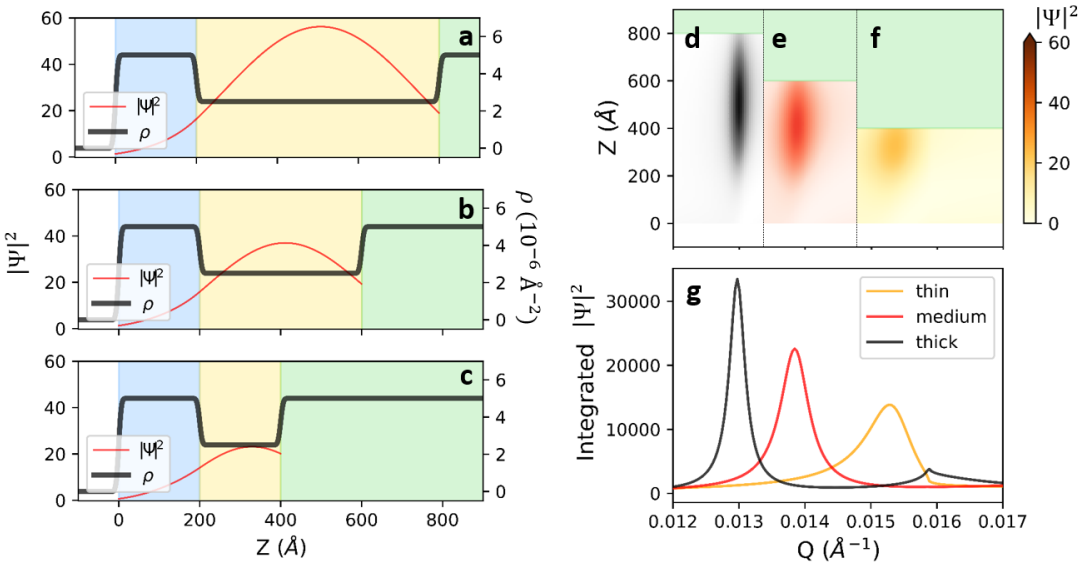

Figure 2.5: Impact of thickness variation on resonant enhancement of neutron density. Panels **(a-c)** show the neutron density enhancement for a potential well with intermediate layer thickness d_2=20, 40 and 60 nm respectively. Panels **(d-f)** display the neutron density enhancement versus sample depth and momentum transfer Q for the structures shown in (a-c), respectively. Panel **g** shows the neutron density integrated along the whole sample depth versus Q. White areas represent air, green areas the substrate, blue and yellow areas the capping and middle layer.

middle layer. The red line shows the calculated depth dependent neutron density, which is resonantly enhanced at the depth of the middle layer. A different design is the potential staircase, shown in Figure 2.4b. In this case we have a depth profile with $\rho_1 < \rho_2 < \rho_3$, which results in a resonant neutron density with maximum depth sensitivity around the top and bottom interfaces. Finally the resonant enhancement can be engineered to be centred on the capping layer with a step-like potential, with $\rho_1 \sim \rho_3 < \rho_2$ as shown in Fig2.4c.

Another way to influence the resonant field is by varying the thickness of the layers. For example, assuming the same potential well design described before, we can assess the impact of the variation of the middle layer thickness with simulations. As shown in Figure 2.5a-c, one can increase the resonant enhancement

by increasing the thickness d_2. Another important factor to keep into account apart from the the depth dependence is the momentum transfer dependence of the resonant field. Figure 2.5d-f shows a two dimensional map of the depth and Q-dependence of $|\Psi|^2$ for the three structures presented in Panels a-c. As one can see the increase of thickness not only increases the resonant enhancement, but as well produces sharper features at increasingly lower Q values. This is more clearly visible in Figure 2.5g, where the integrated density along the whole sample depth is shown versus Q.

Resonance dependence on middle layer scattering potential

Expression (2.15b) shows that the resonance position Q_{res} depends both on thickness d_2 of the middle layer and on its scattering potential ρ_2. The resonant field is thus not only useful to achieve higher intensity, but can be used as a method to track small variations in waveguide sample itself, particularly in the middle layer. If we consider a generalized small SLD deviation $\Delta\rho_2 = \rho_2^1 - \rho_2^0$ (the indices 0 and 1 indicate the initial and final values) and neglect the thickness changes, we can make the following considerations: let us assume an initial resonant wavevector k_{res}^0 and a final k_{res}^1. These wavevectors according to Eq.2.14 have the following definitions:

$$k_{\mathrm{res}}^0 = (k_0^2 - 4\pi\rho_2^0)^{1/2} \tag{2.16}$$

$$k_{\mathrm{res}}^1 = (k_0^2 - 4\pi\rho_2^1)^{1/2} \tag{2.17}$$

and hence one can write:

$$\Delta k_{\mathrm{res}}^2 = 4\pi\Delta\rho_2 \tag{2.18}$$

where

$$\Delta k_{\mathrm{res}}^2 = (k_{\mathrm{res}}^1)^2 - (k_{\mathrm{res}}^0)^2 = (k_{\mathrm{res}}^1 - k_{\mathrm{res}}^0)(k_{\mathrm{res}}^1 + k_{\mathrm{res}}^0), \tag{2.19}$$

If we consider a small $\Delta\rho_2$ variation, one can then write:

$$(k_{\mathrm{res}}^1 + k_{\mathrm{res}}^0) = \frac{Q_{\mathrm{res}}^1}{2} + \frac{Q_{\mathrm{res}}^0}{2} = Q_{\mathrm{res}}^0 + \delta Q \cong Q_{\mathrm{res}}^0 \tag{2.20}$$

where $k_{\mathrm{res}}^0(Q_{\mathrm{res}}^0)$ and $k_{\mathrm{res}}^1(Q_{\mathrm{res}}^1)$ define the resonance wavevector (momentum transfer) in the pristine and modified structures respectively. Combining Eqs. 2.18,

2.19 and 2.20 we can then write:

$$\Delta k_{\mathrm{res}}^2 \cong \Delta k_{\mathrm{res}} Q_{\mathrm{res}}^0 = 4\pi\Delta\rho_2, \tag{2.21}$$

$$\Delta k_{\mathrm{res}} \cong \frac{4\pi\Delta\rho_2}{Q_{\mathrm{res}}^0}. \tag{2.22}$$

Relation (2.22) shows the proportionality relation between the shift of the resonance Δk_{res} and a small variation of the optical potential in the middle layer $\Delta\rho_2$. This principle can be used to track processes that can impact the intermediate layer, such as intercalation of hydrogen or lithium, or modifications of the magnetic potential, as was shown by Kozhenikov et al. in [111].

Detection of resonance peaks

Up to now we focused on the formation of resonances in waveguide structures and on the link between resonance position and sample properties. Another aspect to keep in mind for performing resonant neutron reflectometry (RNR) is the detection channel. In order to detect the Q-position of the resonance, a secondary channel with intensity depending on $|\Psi|^2$ is needed. There are several possibilities to choose from, according to the properties of the sample under study. The first and probably simplest option is to detect the resonance position by spin-flip scattering in a PNR experiment. As explained in the previous section, this type of scattering arises when the magnetization M of a layer in the system is non-collinear to the neutron polarization direction. In order to perform RNR with the SF channel, we have two main requirements, namely the use of PNR and the presence of a ferromagnetic layer in the system, either in the layer of interest itself, or by adding a thin magnetic label layer. The use of PNR is not a limiting requirement, as it is available at many neutron reflectometers, allows measurements with particularly high signal-to-background ratio, is theoretically well understood [112], and has been experimentally established in different systems [113–115]. A disadvantage of using this strategy is the necessity to polarize the neutron beam, which leads to the loss of at least a factor of two in the incoming intensity.

Another possibility to detect the resonance is the absorption channel. If in the system atoms with high absorption cross section are present, the incoming

neutrons will be partially absorbed in the sample. Useful for the detection for neutron resonances are absorption reactions with spontaneous emission of α or γ radiation:

$$ {}^{m}_{a}A + n \longrightarrow {}^{m+1}_{a}A + \gamma \tag{2.23} $$

$$ {}^{m}_{a}A + n \longrightarrow {}^{m-3}_{a-2}B + \alpha. \tag{2.24} $$

Here the atom A with mass number m and atomic number a absorbs one neutron and can either emit a γ photon (2.23) or become unstable and decay into atom B plus an α particle. In both cases, the emission of the secondary radiation can be used as detection channel for resonances, as previously demonstrated for γ [116] and α [117] respectively. Also in this case the requirement is to have an atom that undergoes one of the previously mentioned reactions, such as Gd or Li, either in the sample itself or as additional label layer. Moreover one needs a dedicated detector for the secondary particles in addition to the basic neutron reflectometry setup.

Neutron channeling is another possible way to detect neutron resonances. In this case a sample with the well SLD profile design creates a guide for the neutrons which are channeled through the entire film length, until being emitted at the side in form of a microbeam. This divergent microbeam is once again proportional to the resonant neutron wave density $|\Psi|^2$. The principle and details of this technique can be found in the following works: [118, 119].

One more channel that can be used is the transmission of neutrons, in cases where a low ρ substrate, such as silicon, is used. Here some of the incoming neutrons will be transmitted through the whole sample, giving rise to a transmitted intensity which is resonantly enhanced at a specific incoming angle. An example of this effect is found in Ref. [120].

Finally, the incoherent scattering of the neutrons is also a useful detection channel if in the system atoms with high incoherent cross section are present, such as hydrogen or vanadium. Similarly to the absorption case, here as well one can measure either the reflectivity minimum at the resonant momentum transfer, or measure the incoherently scattered neutrons with an additional detector. Since incoherent neutron scattering is isotropic, the detector is placed close to the sample to maximise the solid angle and subsequently the detected intensity, as shown in

Refs. [115, 121].

In all the case mentioned above an alternative way to measure the resonance is to detect the reflectivity dip that will appear in the total reflection. This strategy on one hand is advantageous since it does not require any additional equipment, however the resolution can decrease if the dip is too shallow. In general, if the intensity of the minimum of the dip is higher than the corresponding maxima of the peak, then the statistical error increases for the former. Nevertheless this mode of detection was demonstrated and used in case of absorbing layers [122], and magnetic and incoherently scattering layers [115, 121].

The choice of detection method must hence reflect first and foremost the composition of the sample under study, and secondly the experimental setup available. If no magnetic, absorbing or incoherently scattering atoms are present in the waveguide structure, an additional thin layer with labelling function can be included, after assessing the impact of this thin layer on the overall physical properties of the layer of interest.

The position of the label layer is also important and should be selected to be most responsive to the resonant field. Figure 2.6a shows once again a potential well depth profile with corresponding resonant enhancement. Assuming the layer of interest to be the intermediate one (yellow area), one could place a label layer at any depth within the range 20-60 nm. We considered three prominent positions, namely at the interface with the capping layer (named top, indicated by the pink arrow), in the middle of the layer (middle, purple arrow), or at the interface with the substrate (bottom, indigo arrow). Figure 2.6b shows the depth and Q-dependence of the neutron density, which in turn will be proportional to our detection channel intensity. The depth cuts of this 2D map are shown in Figure 2.6c, where we observe that for this particular sample design the maximum sensitivity to the resonant field is achieved when the label is placed in the middle of the layer of interest. This example shows the importance of studying the resonant field dependence with simulations to decide the best position for the label layer during the sample design phase.

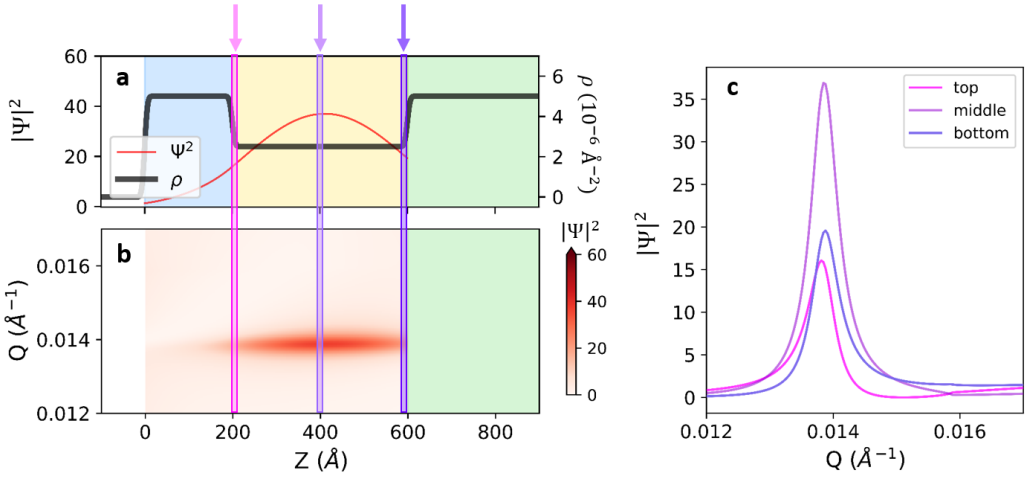

Figure 2.6: Label layer sensitivity to the resonant field versus depth. **a** Neutron density enhancement for a potential well with intermediate layer thickness d_2=40 nm; **b** Neutron density enhancement versus sample depth and momentum transfer Q for the structure shown in (a); **c** Neutron density at the label layer depth of 20 (top), 40 (middle), 60 (bottom) nm versus momentum transfer Q.

2.1.3 Experimental details

The majority of PNR and XRR experiments shown in this thesis were performed at the angle dispersive NREX reflectometer [123] at the FRM, in Garching. A scheme of the setup is shown in Figure 2.7. The instrument is located in the neutron guide hall and is provided with cold neutrons from the guide NL1. A monochromator (M) comprising 7 blades each composed of 6 parallel, highly oriented pyrolytic graphite crystals is able to reflect and focus the wavelength λ=4.28 Å at the sample position. The number of blades used influences the beam intensity, width and wavelength distribution, so that the flux and resolution can be tuned accordingly. The polarization (P) and subsequent analysis (A) of the beam is obtained with transmission through Fe/Si supermirrors on silicon substrate, with external magnetic field of 1 kOe produced by permanent magnets, to ensure the saturation of Fe layers. The direct beam is polarized in the '-' direction and flipped by adiabatic radio-frequency spin flippers SF_1 and SF_2 placed before and after the sample table. The efficiency of polarizer, analyser and flipper are $>$ 99.9%, $>$ 99.0%, and $>$ 99.99% respectively. An alternative analyser is the fan-shaped arrangement of

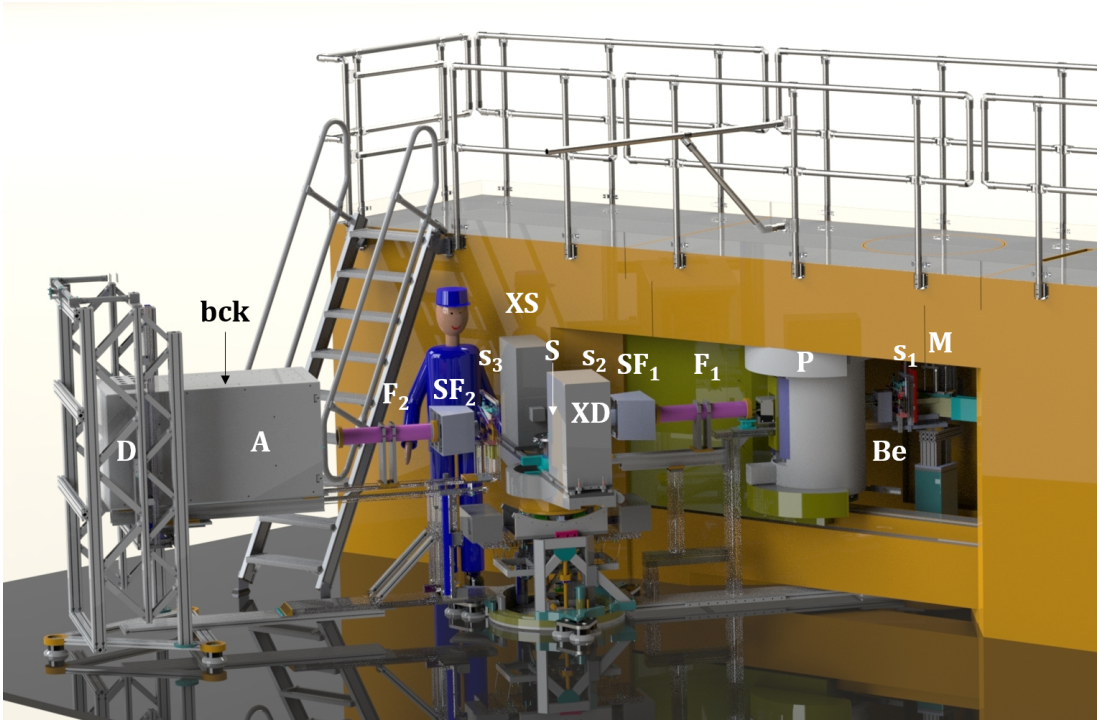

Figure 2.7: Scheme of the NREX reflectometer:starting from the right we see the monochromator (M), Beryllium filter (Be), slit system (s_{1-3}), polarizer (P), vacuumized flight tubes (F_{1-2}), spin flippers (SF_{1-2}), sample table (S), x-ray source (XS) and detector (XD), analyzer (A), background shielding (bck), and detector (D). Picture courtesy of Franz Tralmer.

30 polarizing FeSi supermirrors on 1mm Borofloat glass substrates, which allows the polarization analysis of off-specular scattering along the whole detector area. The neutrons are collected in a 2-dimensional position sensitive ^{3}He detector or in one-dimensional pencil detector (D), with efficiencies of 72% and 94% respectively. The divergence of the incoming beam is given by the two slits S_1 and S_2 placed before the sample at a distance of 2m between each other. The standard opening of 1mm for both slits typically used for reflectometry experiment gives a divergence of 0.03°. Both the vacuumized flight tubes (F_1 and F_2) placed before and after the sample reduce the unwanted neutron scattering with air, optimizing the beam intensity. On the other hand, the shielding box (bck) surrounding the detector prevents the detection of neutrons coming from the environment, hence reducing the background. The combination of high intensity combined with low

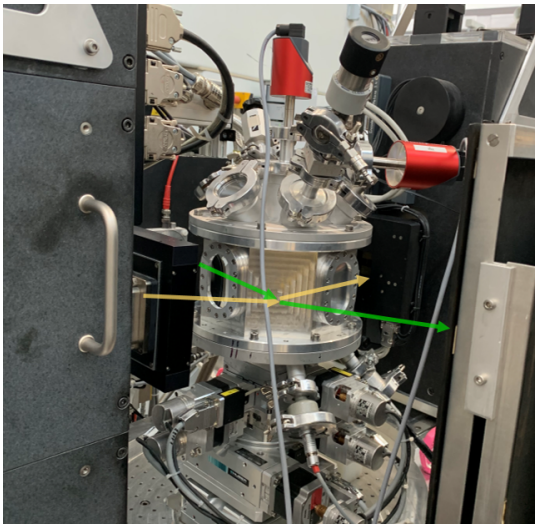

Figure 2.8: Picture of the gas tight chamber with scattering scheme showing the neutron path (green) and x-ray path (yellow). Both beams are centred at the sample position.

background allows to measure the reflectivity over around 6 orders of magnitude on samples with area of 5*5mm^2 in PNR mode.

The unique feature of NREX, allowing for simultaneous neutron and x-ray reflectometry, was used in this thesis for the study of hydrogen absorption kinetics. The x-ray source (XS) is a conventional Cu-Kα tube (λ_x=1.541 Å) with Goebel Mirror or a double Ge-Crystal monochromator. The photon propagation, indicated in yellow in Figure 2.8, is perpendicular to the neutron direction (green arrows). Both beams are centred on the sample position. The x-rays are collected at a 1-dimensional DECTRIS detector (XD). Both x-ray source and detector are located on a table that follows the goniometer tilt, hence the scattering plane of photons is independent of the neutrons reflection angle. In order to perform PNR/XRR experiments in controlled hydrogen atmosphere, a gas tight sample chamber was designed and installed at NREX. The chamber (Figure 2.8) has 100 μm Mylar and 100 μm aluminium windows for the x-ray and neutron beams, respectively. The transmission for Cu k$_\alpha$ x-rays is 94%, for neutrons close to 100%. The design allows for easy substitution in case of damage of these fragile windows without the use of any glue. The chamber is connected via vacuum-sealed valves to a turbomolecular pump and to the hydrogen (H_2) or gas mixture ($Ar_{98\%}H_{2\%}$) bottle. On top of the

Table 2.1: Comparison between technical data of different reflectometers.

Name	λ (Å)	Q-range (Å^{-1})	S geometry	P/A eff. %	Φ (n cm^2/s)
NREX	4.28	0 – 0.5	horizontal	99.9/99.0	3 x 10^5
Super ADAM	5.21	0 - 2.5	vertical	99.8/99.4	6 x 10^5
V6	4.66	0 - 0.46	horizontal	99.9/93	1 x 10^4
GINA	4.60	0 - 0.25	horizontal	89/99.6	3 x 10^3

chamber, two pressure gauges are installed to read the pressure in different ranges, allowing a precise measurement between 1000 and 1*10^{-4} mbar. The thin film sample inside the chamber are placed on a heating plate that can reach 600K.

Other sample environment options at NREX include external magnetic field, low temperature measurement, and an *in situ* transport setup. The magnetic field, produced by a conventional electromagnet, can reach magnitudes between 5 and 5000 Oe and for the experiment shown in this thesis it was applied in-plane along the neutron polarization direction. A closed-cycle cryostat allows to work in a temperature range between 3 and 300 K. The sample stick is equipped with an additional transport setup, described in the following section.

Additional facilities used were the Super ADAM reflectometer [124], the V6 reflectometer [125], and the GINA reflectometer [126]. A comparison of the main technical data of neutron reflectometers is reported in Table 2.1. S geometry refers to the orientation of the sample surface, P/A eff. indicates polarizer/analyzer efficiencies and the flux Φ is referred to an unpolarized beam at the sample position.

Concerning x-rays, besides the NREX reflectometer, additional measurements were performed at the MPI-MF beamline at the Kara Karlsruhe Research Accelerator (λ=1.238 Å) [127].

All PNR and XRR curves were analyzed with the GenX software [128], while theoretical simulations were calculated with the Parratt32 software [129]. Errors on the fitted parameters correspond to a 5% increase in the figure of merit of the fit.

2.2 Other characterization methods

2.2.1 SQUID magnetometry

A typical preliminary characterization method for thin films magnetic properties is magnetometry. Compared to PNR, which gives a depth dependent magnetic profile as explained before, techniques such as VSM and SQUID magnetometry give access to the net magnetization $M(emu)$ of thin films integrated over the whole film volume, according to the following expression:

$$M(emu) = M(G) \times V(cm^3) = M(G) \times A(cm^2) \times d(cm). \tag{2.25}$$

For this reason it is necessary to accurately measure the area A and thickness d of the magnetic part of the sample to obtain the correct magnetization value. Nevertheless it is a simple technique that is useful for cross-checking PNR results.

The system used was a commercial MPMS3 magnetometer from Quantum Design, equipped with a superconducting magnet that allows to reach 10 T. A helium refrigerator allows the measurement of magnetization between 5 and 300 K. In this case, as for PNR, the orientation of the sample with respect to the applied magnetic field direction H is important, due to the strongly anisotropic magnetic properties of thin films. All the measurements shown in this thesis have been performed with in-plane magnetic field along one edge of the sample.

2.2.2 X-ray (and neutron) diffraction

Reflectometry is a small angle scattering technique, allowing a study of the average scattering length density, but no information about the position and distances between the atoms is provided. For this purpose, diffraction techniques which have access to a larger Q are needed. The crystalline quality and orientation of thin films was studied by means of x-ray diffraction performed at the home built system of MPI-FKF. The source used was a conventional x-ray tube, from which the Cu k_α line was filtered and used. The use of a 1D detector (DECTRIS) allowed the reconstruction of scattering maps, where the scattered x-ray intensity is mapped against incoming and outgoing angles θ_1 and θ_2. This allows access to

both specular and off-specular signal, and let us distinguish between single and polycrystalline samples.

The magnetic reflections of thin films corresponding to the periodicity of 1 atomic unit cell were additionally studied by polarized neutron diffraction (PND) at Super ADAM, where the horizontal scattering geometry allows to reach high momentum transfer up to 2.5 Å^{-1}.

2.2.3 Electrical transport

A home built transport setup was used to study the in-plane electrical resistance of the films. The setup consists of four metallic springs, which are pressed on the sample surface. The excitation current for the 4-wire resistance measurement is provided through the outer contacts, while the voltage is measured through the inner contacts (Figure 2.9a-c). The wires are then connected through the sample stick with a Lakeshore 370 resistivity bridge, which allows to reduce the noise level by tuning the excitation current and measurement range of resistance. The whole sample stick is inserted in the cryostat which in turn is placed in the electromagnetic field, described in the previous section. This configuration allows to measure magneto-resistance (MR) curves, where the resistance is measured as the field is swept. Anisotropic magneto-resistance (AMR) can as well be measured with the motorized rotation of the sample stick, or of the cryostat.

For magnetic samples, the resistance depends on the angle ϕ between the electrical current $\vec{J}$ and sample magnetization $\vec{M}$, through the AMR effect. The sign of AMR depends on the type of scattering mechanism governing the electrical resistance, and it strongly depends on different materials and their conduction bands [131]. Thanks to this effect, one can use MR measurements to study the magnetic properties of a sample such as the coercivity and easy axis, similarly to a magnetometry experiment. An example is reported in Figure 2.9d-f where the MR of a 10nm cobalt layer deposited on MgO was studied at 5K. Cobalt has a positive AMR, meaning that when $\vec{J} \parallel \vec{M}$ we have a high resistance (R) state, and when $\vec{J} \perp \vec{M}$ a low R state [131]. In order to see this, the MR was measured in two different configurations: longitudinal, with $\vec{J} \parallel \vec{H}$, and transverse, with $\vec{J} \perp \vec{H}$. At $\vec{H}$ bigger than saturation field, the magnetic moment follows the external field,

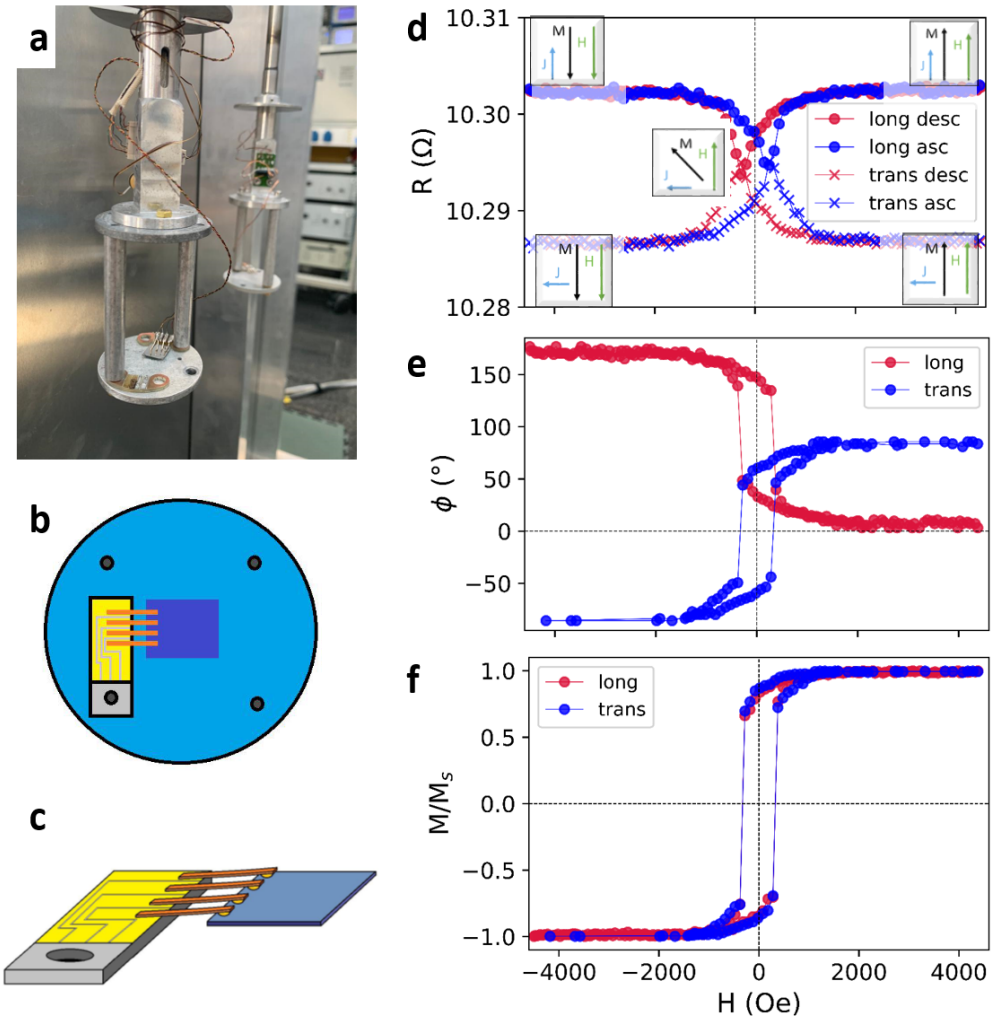

Figure 2.9: Transport measurements. **a**. Sample holder and transport setup at the bottom of the stick; **b** Scheme of the transport setup from top and side (**c**) view. The sample is represented in the dark blue area. (sketch adapted from [130]); **d**. Sample stick mounted in cryostat and electromagnet for MR measurements; **e** Anisotropic magnetoresistance of a 10 nm Co layer at 5K, in longitudinal and transverse mode. Square panels show a scheme of the orientation of magnetization $\vec{M}$, field $\vec{H}$ and current $\vec{J}$; **f** Field dependence of the angle between $\vec{M}$ and current $\vec{J}$; **g** Hysteresis loop retrieved from AMR measurement shown in Panel e.

as schematized in the square panels of Figure 2.9e. Accordingly we observe a high R for the longitudinal measurement and a low R for the transverse. Around coercivity, assuming a coherent rotation of the magnetic domains, we observe an intermediate R state, where the magnetization lays along the system easy axis (for this sample along the (110) direction). By using the following relations, derived in Refs. [5, 132] for cubic and hexagonal polycrystalline ferromagnets, we can recover the angular dependence of magnetization, shown in Figure 2.9e:

$$R(\phi) = R(0) - \Delta R \sin^2 \phi \tag{2.26}$$

$$\Delta R = R_{long} - R_{trans} \tag{2.27}$$

and the the hysteresis loop, shown in Figure 2.9f:

$$\cos \phi(H_{long}) = M(H_{long})/M_{sat} \tag{2.28}$$

$$\sin \phi(H_{trans}) = M(H_{trans})/M_{sat} \tag{2.29}$$

with M_{sat} saturation moment for renormalization. This example shows the potential of such home-built transport setup for characterization of magnetic samples. Moreover thanks to its versatility it was used both for *ex situ* and *in situ* measurements, in combination with PNR at NREX.

Chapter 3

Resonant neutron reflectometry for hydrogen detection in thin films

As we have seen in the introduction, the study of the incorporation of hydrogen in materials is a central challenge for at least two fields of research: the solid state hydrogen storage research, and the rising branch of proton-doping for the modification of electronic properties of materials. In both branches, it is crucial to detect and quantify hydrogen with the highest precision possible and allowing for *in situ* studies. Many techniques, as reviewed in the introduction, have limitations such as being indirect, destructive, or working only in high vacuum. In the following chapter, we present a new method, called resonant neutron reflectometry (RNR), which provides absolute concentration values. In kinetics, *in situ* experiments, changes of the hydrogen concentration as small as 1 at.% can be detected within a few seconds of measurement time. Here we explain the relation between the properties of neutron waveguides and hydrogen absorbed in the central layer, constituting the basis for the application of the RNR method. Two subsequent experimental sections present the main results on *in situ* loading of hydrogen into niobium layers, starting from the proof of principle experiment (see Ref. [133]) and proceeding to cases where the method is used to study the actual physics of absorption at different environment conditions (Ref. [134]).

3.1 Proof of principle: RNR on Nb systems

3.1.1 Theoretical foundation of RNR for hydrogen detection and quantification

The RNR method is based on the formation of neutron standing waves (resonances or waveguide) in thin films, reviewed in the previous chapter, with high ρ contrast between the material of interest and the neighbouring layers. If we assume an intermediate layer that is a hydrogen absorber material, the relations shown in Section 2.1.2 apply with $\Delta\rho_2$ being the SLD variation due to the considered hydrogenation process, thus we can write:

$$\Delta Q_{\text{res}} \cong \frac{8\pi\Delta\rho_2}{Q^0_{\text{res}}} = \frac{8\pi\bar{N}}{Q^0_{\text{res}}} b_H c_H. \tag{3.1}$$

where $\bar{N}$ is the average atomic density of the active layer, and b_H and c_H are the scattering length and atomic concentration of hydrogen in the active layer, respectively.

Formula (3.1) shows that the resonant field shift is directly proportional to the hydrogen content c_H and can be used to quantify hydrogen atoms absorbed *in situ*. Figure 3.1 shows the linear dependence between the shift of resonance position and the change in scattering length density of the absorbing layer $\Delta\rho_2$, which in turn depends on the average hydrogen concentration absorbed. The values shown here were simulated for a waveguide structure of 50 nm of Nb on sapphire substrate and 3 nm of Pt on top, without accounting for any thickness swelling effects. Since for several materials, such as niobium, the hydrogen absorption entails an increase of thickness of the layer, formula 3.1 should be corrected at high hydrogen content, where the swelling effect can not be neglected.

3.1.2 Sample design and growth

Samples of composition Al_2O_3/Nb(25nm)/Co(3nm)/Nb(25nm)/Pt(3nm), sketched inFigure 3.2.a, were considered for the method's proof of principle. The sapphire substrate was chosen due to its high SLD ($\rho = 5.72{*}10^{-6}\text{Å}^{-2}$) and due to the ability to grow a high-quality Nb layer on it [130, 135, 136]. The middle layer was

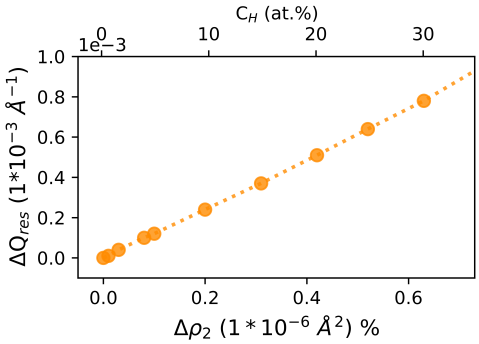

Figure 3.1: Dependence of the shift of resonance on hydrogen content calculated for a Al_2O_3/Nb(50nm)/Pt(3nm) waveguide.

chosen to be niobium, a well-known hydrogen absorber [137] with superconducting properties [138] and a low ρ=3.91*10^{-6}Å^{-2}. The bulk phase diagram of the NbH system is shown in 3.3. Here we see that Nb is able to incorporate a very high concentration of H, which in bulk leads to the formation of different phases, including solid solutions (α and α') and hydrides (β). This phase diagram is substantially different in thin films due to the clamping effect of the substrates, which prevents the formation of the β phase, as shown in Figure 3.3b [139–141]. Nevertheless, many thin film studies [74, 76, 142, 143] have shown the possibility to load high amounts of hydrogen. Moreover, hydrogen in bulk niobium has a room temperature diffusion coefficient of 2.1*10^{-6} cm^2 s^{-1} [145], which is only one order of magnitude lower than the typical self-diffusion coefficients of liquids. For this reason if we don't consider phase transitions, grain boundaries and nano-confinement effects, we would expect an extremely fast loading (around 5 μs) and homogeneous distribution of hydrogen along the whole depth of Nb. The Co inserted in between Nb layers acts as the label magnetic layer needed to trace the position of the resonance. The thickness of the layer was chosen to be small enough to allow transmission of hydrogen, as previously shown for Fe in Fe/Nb multilayers [79], and thick enough to be magnetic with properties close to bulk. Finally the structure was capped by a 3nm-thick Pt layer in order to enable the splitting of H_2 molecules at the surface and diffuse H atoms to the layers underneath [146]. Figure (3.2)b shows the calculated scattering potential of the pristine and hydrogenated sample loaded with

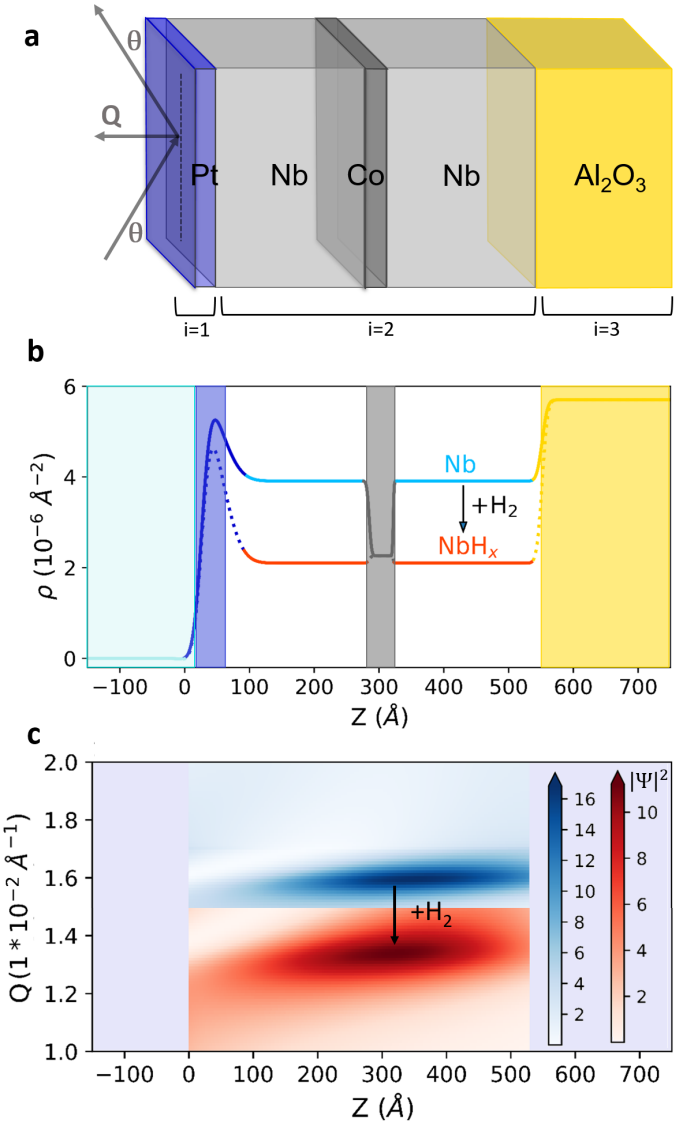

Figure 3.2: Resonant neutron reflectometry scheme. **a** Sketch of the thin-film structure and geometry of the reflectometric measurements. Q is the wavevector transfer, and θ the scattering angle. **b** Depth profile of the scattering length density ρ of the sample before (blue line) and after (red line) incorporation of 85 at.% hydrogen. **c**. The numerically calculated neutron density enhancement (with respect to the incoming beam with $|\Psi|^2 = 1$), along the film depth before (blue) and after (red) hydrogenation. For simplicity, the schematic does not include the H-induced swelling of the film.

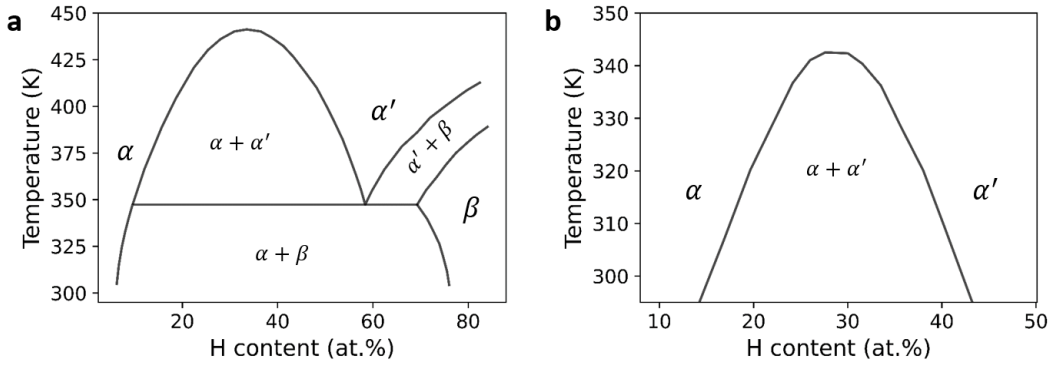

Figure 3.3: Nb/H phase diagrams. **a** Bulk Nb-H phase diagram reproduced from datapoints of [144]. **b** Phase diagram of Nb(20 nm) deposited on glass, reproduced from [141].

85 at.% of H. Such a concentration leads to a significant suppression of SLD of Nb from ρ =3.91*10^{-6}Å^{-2} to ρ =2.13*10^{-6}Å^{-2}. The SLD of the Co layer is expected to remain the same as it is more favourable for hydrogen to stay in the Nb layer, similarly as to what happens in the case of Fe/Nb reported in [74]. Figure (3.2)c shows the depth and Q dependency of the neutron field density $|\Psi|^2$ calculated for the above-mentioned profiles. For the pristine sample the resonance is observed at Q_{res}=1.6*10^{-2} Å^{-1} and extends at depths comprising the two Nb layers and the Co in between them, ensuring the label layer to have the maximum sensitivity to the resonant field. The neutron field density $|\Psi|^2$ is at its maximum 16 times enhanced with respect to an incoming beam of intensity 1. The absorption of 85 at.% of H induces a shift of Q_{res}=1.3*10^{-2} Å^{-1} and a decrease in amplitude of the resonant field to 10 times enhancement, due to a broadening of the peak caused by the different scattering potential.

According to these simulations, a series of identical samples were grown simultaneously with the Molecular Beam Epitaxy (MBE) setup of the Jülich Center for Neutron Science. This is a DCA M600 MBE system with a base pressure of 10^{-10} mbar. Before deposition, the substrates were cleaned from organic contaminations with ethanol and isopropanol ex-situ and heated at 1000°C in ultra high vacuum for 2-3 hours. The substrate temperature was kept at 303 K in order to minimize the inter-diffusion of the cobalt atoms into the niobium layer and preserve the

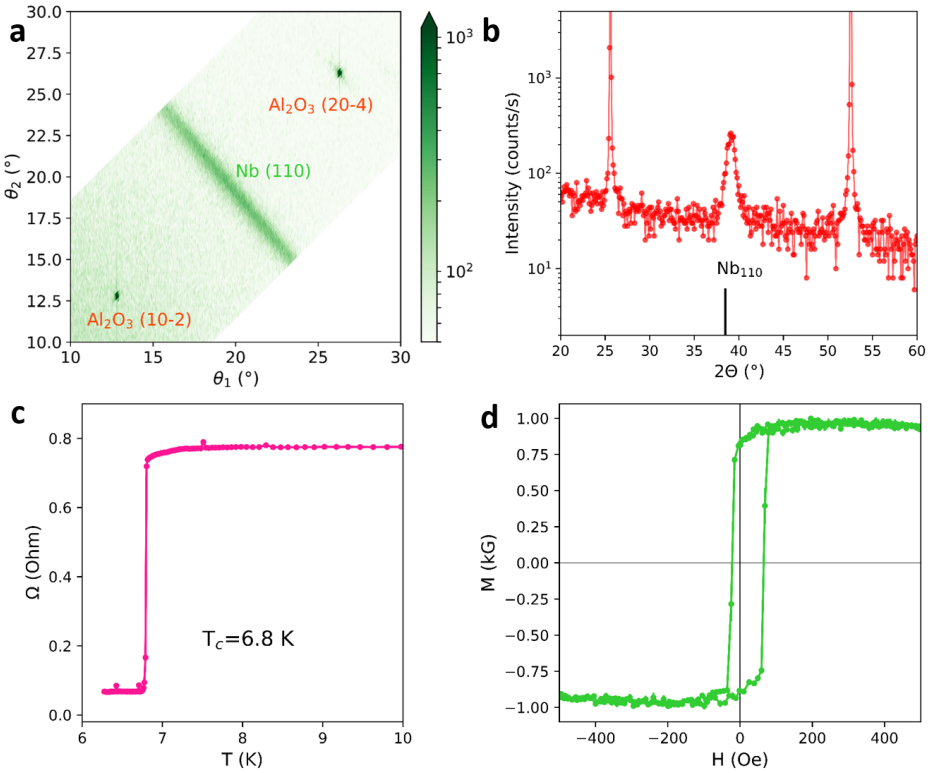

Figure 3.4: Preliminary characterization. **a** XRD scattering map of the as prepared sample showing bright peaks from sapphire and the reflection coming from polycrystalline Nb; **b** XRD specular cut of the as prepared sample showing sharp peaks from sapphire and the reflection coming from polycrystalline Nb; **c** Superconducting transition temperature from transport measurement; **d** Hysteresis loop with magnetic field applied in-plane of the as prepared sample.

good magnetic properties for such a thin layer. The rates of deposition were 0.4 Å/s for niobium, 0.1 Å/s for cobalt and 0.2 Å/s for platinum. Co was deposited by thermal evaporation from an effusion cell while Nb and Pt were grown by electron beam evaporation.

3.1.3 Preliminary characterization

The samples were characterized by XRD, SQUID magnetometry and transport measurement to have an insight on structural, magnetic and superconducting prop-

erties. XRD suggested a polycrystalline character of the Nb layers with preferential orientation along the (110) plane, as shown in Figure 3.4a,b. The transport properties of niobium (Figure 3.4c), measured by four-probe device, showed a T_c of ~ 7 K, which is lower than bulk, hence with a hint of proximity effect due to the presence of Co thin layer [146]. The hysteresis loop obtained by SQUID magnetometry measurement (Figure 3.4d) shows a saturation magnetic moment approaching the bulk value of 1.5 kG, that implies a good quality deposition of such a thin cobalt layer. The shift of the loop is an artifact due to the imprecise zero-field calibration of the SQUID magnetometer.

The samples were as well characterized by simultaneous XRR and polarized neutron reflectometry (PNR) experiments at NREX. Figure 3.5a shows the XRR curve in vacuum measured at NREX. Two main sets of Kiessig oscillations are here overlapping, a fast one connected to the thick Nb layers, and a much slower one, given by the thin Pt on top of the structure. Figure 3.5b shows a saturation PNR curve measured in vacuum at NREX under the application of a magnetic field H=4.5 kG. In this condition we expect the Co layer to be aligned with H, hence giving rise to a pure NSF scattering. The strong spin asymmetry present between R^{--} and R^{++} is proportional to the amplitude of magnetic moment of Co, that we can compare with the one extracted from magnetometry. Finally, in Figure 3.5c the remanence curve with full polarization analysis of the sample in vacuum is shown. In this case the external field was released to 5 G, allowing the Co magnetization to change its direction parallel to the easy axis of the layer. We can observe a strong SF signal together with the spin asymmetry, indicating an angle of magnetization α of around 45° with respect to H. This easy axis is induced by the R-cut sapphire substrates. The strong feature indicated by the vertical dash line is the resonance peak, appearing clearly at Q_{res}. For both XRR and PNR curves, model reflectivities were fitted to experimental data, as shown in the insets of Figure 3.5 allowing for the recovery of all significant parameters such as thickness d, scattering length density ρ and roughness σ for all layers.The SLDs for XRR fitting were kept constant at nominal values. The Tables 3.2, 3.1 summarize the values obtained and the corresponding errors calculated as a 5 at.% increase in the figure of merit of the fit.

We obtained a good match between the thickness and roughness of all layers

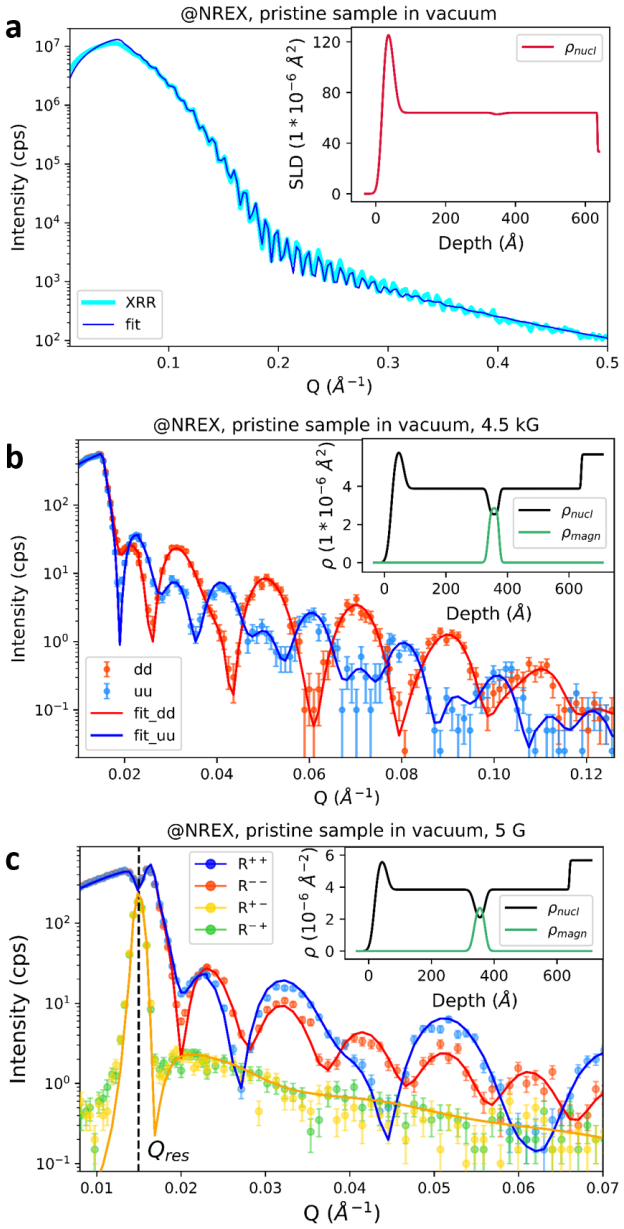

Figure 3.5: XRR and PNR measurements of the pristine sample at NREX. **a** XRR measurement of the pristine sample in vacuum. The dark blue line shows the reflectivity fit. Inset: SLD profile from XRR fit; **b** PNR saturation curve measured in vacuum with external magnetic field of 4.5 kG. Only NSF channels are shown. Solid lines show the fit to the experimental data. Inset: SLD depth profile obtained from fit; **c** PNR remanence curve measured in vacuum with external magnetic field of 5 G. Solid lines show the fit of experimental data. Inset: SLD depth profile obtained from fit.

Table 3.1: Parameters obtained from XRR data fitting.

	d (Å)	σ (Å) (RMS roughness)
Al_2O_3	∞	0.8 ± 0
Nb1	270 ± 2	11 ± 7
Co	31 ± 4	6 ± 3
Nb2	284 ± 5	11 ± 2
Pt	33 ± 2	10 ± 0.5

Table 3.2: Parameters obtained from PNR data fitting.

	d (Å)	σ (Å)	ρ_{nucl} (10^{-6} Å^{-2})	ρ_{mag} (kG)	α (°)
Al_2O_3	∞	2 ± 0	5.7 ± 0.4	0	0
Nb1	268 ± 9	4 ± 9	3.9 ± 0.4	0	0
Co	35 ± 2	10 ± 3	2 ± 0.7	0.99 ± 0.07	51 ± 5
Nb2	276 ± 5	4 ± 22	3.8 ± 0.5	0	0
Pt	41 ± 6	12 ± 4	5.7 ± 0.6	0	0

independently by XRR and PNR measurements. Moreover the magnetic moment of Co of 1 kG obatined by PNR corresponds well within errorbar to the one obtained by SQUID magnetometry, indicating a consistent fitting procedure.

3.1.4 RNR measurements

After conventional PNR measurement of the pristine state, the waveguide method was tested to measure hydrogen absorption in Nb. The samples resonance peak was first measured in vacuum and then during exposition at room temperature of a constant $Ar_{98\%}H_{2\%}$ gas pressure of 8 mbar, corresponding to 0.16 mbar of pure H_2.

The waveguide method was applied in two different modes on 2 identical samples. The first tracking mode consisted in measuring a series of consecutive Q-scans around the resonance position during the hydrogen loading, as shown in Figure (3.6)a. The recorded peaks were fitted by a Gaussian (solid lines in Figure (3.6)a). Figure (3.6)b shows the time dependent shift of the peak centres of the Gaussian. This allows to have an insight on the kinetics of H absorption process, thanks to the direct proportionality between the Q_{res} shift and c_H.

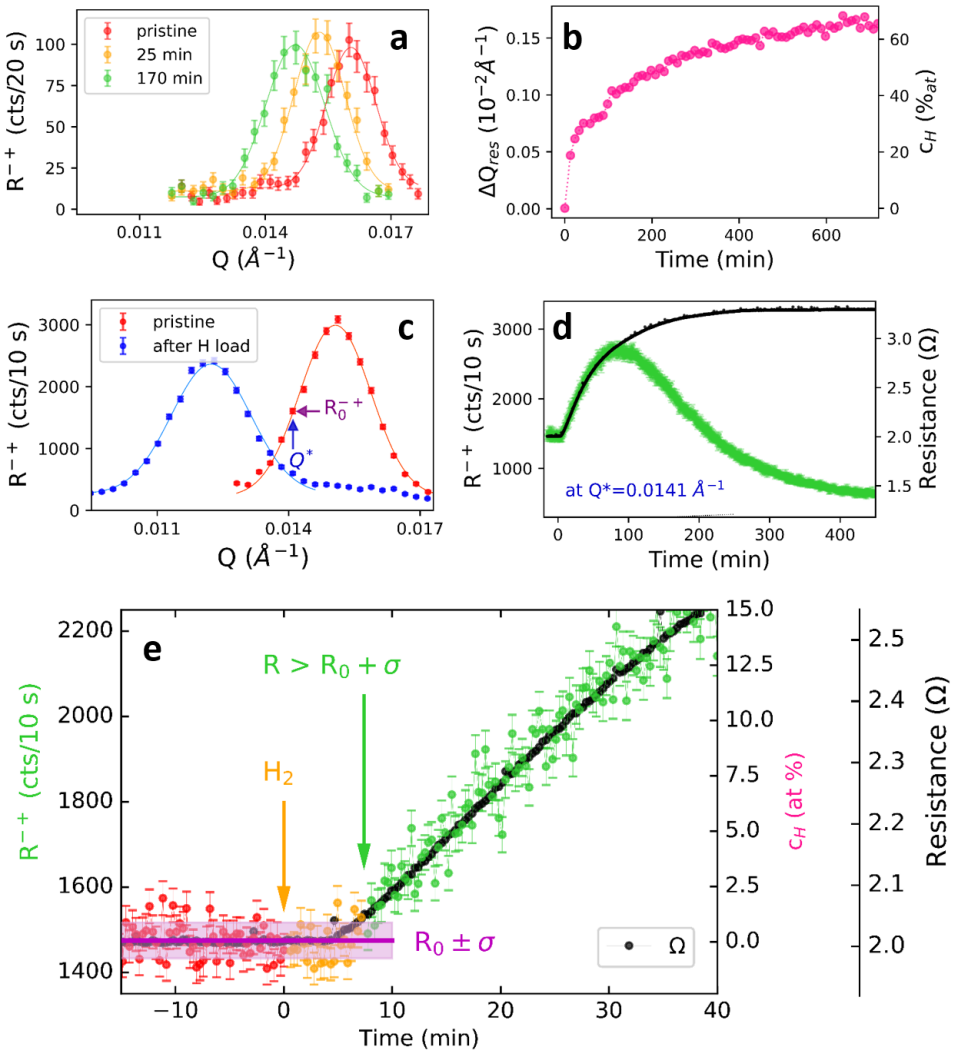

Figure 3.6: Resonant neutron reflectometry during hydrogen loading at room temperature with 8 mbar of $Ar_{98\%}H_{2\%}$. **(a)** Typical peak profiles in Q-scan mode on sample 1 at V6. **(b)** Time dependent shift (left scale) and corresponding hydrogen concentration (right scale) of the resonance peak shown in panel a. **(c)** Resonance peak measured before and after incorporation of 85 at.% of H on sample 2 at NREX. The lines are the results of fits to Gaussian profiles. The wave vector Q^* used for the fixed-Q mode is shown. **(d)** Time evolution of the intensity at Q^*, and electrical resistance during H absorption. **(e)** Closeup of the fixed-Q data in panel e, before H_2 gas was injected into the vacuum chamber (red data points), right after injection (yellow points), and after an H-induced change of the reflectivity was detected outside the standard deviation σ (green points). Resistance data points are shown for comparison in black.

Another way to track the shift of resonance is by staying at one fixed Q position on the resonance peak and monitoring the count rate as it changes during the H loading, as shown in Figure (3.6)d. Simultaneous resistivity measurements were also taken in order to compare the RNR with a well-known and widely used (though indirect) method. Figure (3.6)c shows the point chosen for the timescan, called Q*, corresponding to one of the maxima of the derivative of the Gaussian fit $f(Q)$ of the resonance peak in vacuum:

$$f(Q) = h \exp\left(-\frac{2(Q - Q_{res})^2}{w^2}\right) \tag{3.2}$$

with height h and width w=2σ. Figure (3.6)e shows a zoom of the beginning of absorption process. Staying at Q*, the count rate in vacuum was measured for 20 minutes (shown in red) in order to determine the stability of the system. The statistical fluctuation around the average value R_0 is similar to the standard deviation $\sigma = \sqrt{R}$, indicating the absence of additional systematic errors. The gas mixture was then injected in the chamber in correspondence of the yellow arrow at t=0. The first detectable increase due to hydrogen absorption and shift of the peak is considered to be the second consecutive point with intensity greater than $R_0 + \sigma$, indicated with the green arrow. By assuming that the resonance peak does not change in intensity during absorption, as expected in the case of small hydrogen concentration and stable magnetic properties of the label layer, it is then possible to calculate the relation between the shift of resonance ΔQ and the observed change in count rate ΔI, and obtain the hydrogen concentration in the sample as follows:

$$\Delta I = \frac{2h}{w} e^{-1/2} \Delta Q = \frac{2h}{w} e^{-1/2} \frac{8\pi \bar{N}}{Q_{res}} b_H c_H \tag{3.3}$$

where $\frac{2h}{w} e^{-1/2}$ is the slope of the tangent at maximum of derivative (Q*) of the Gaussian of Eq.3.2. In the small c_H region (below the 30% of atomic H/Nb) the absorption kinetics are very similar to that shown in Figure (3.6)b.

Since Eq. (3.1) is valid under the assumption of constant film thickness and homogeneous hydrogen distribution, we performed reflectometry simulations to

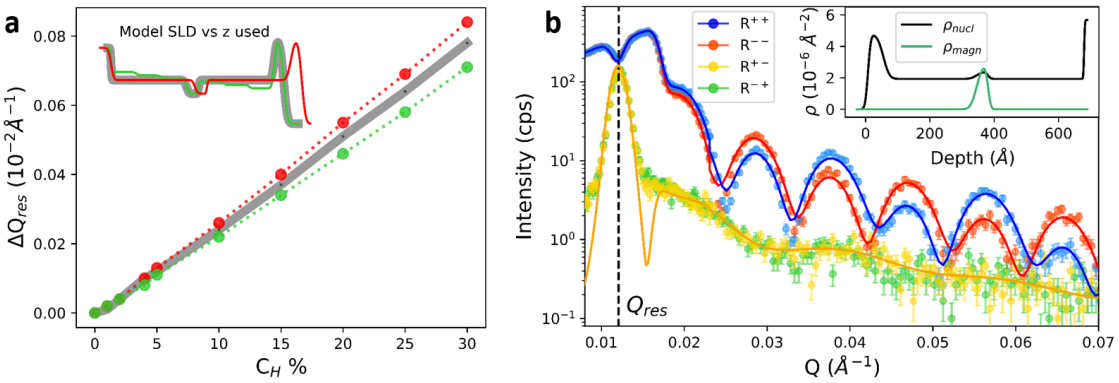

Figure 3.7: Thickness swelling effect. **a** Simulated shift of the resonance peak for homogeneous H distribution along the film depth and no thickness changes (grey), for homogeneous distribution with 10% thickness change (red), and concentration gradient of H along the layer depth (green).**b** PNR measurement of the hydrogenated sample at NREX at H=5G. Solid lines show the fit of experimental data. Inset: SLD depth profile obtained from fit.

assess the impact of H-induced swelling of the film or H inhomogeneities on the position of the resonant peak (Figure 3.7a). The thickness changes considered were of 1% increased total thickness for every 10 at.% of H loaded, according to previous literature [74]. Our simulations show that this deviation for small H concentration, below 20 at.%, is negligible, while for higher concentrations it becomes more important, up to a 10 at.% overestimation on hydrogen content for an 8% thickness increase. In this case, it is possible to apply correction factors, which are obtained from the full reflectivity curves, measured at the beginning and end of the loading process.

To this end, and in order to obtain a realistic estimate of the film swelling, we remeasured the full PNR at the end of the hydrogenation process (Figure 3.7b). The fitting of these data confirmed that cobalt was left unaltered, both in thickness and magnetic moment, and that it let hydrogen pass through as confirmed by the homogeneous H distribution in both Nb layers. Another observation obtained was the expected thickness increase of the Nb layer of $\sim$ 10 % in the fully hydrogenated state (Inset of Figure 3.7b), with a final c_H = 85 at.%. These information can be used to correct the c_H obtained by RNR. Specifically, when we apply Eq. (3.1)

to the shift shown in Figure 3.6c, one obtains $c_H = 93$ at.%, compared to $c_H = 85$ at.% if the thickness change is taken into account.

As it will be discussed in more details in the next section, in our experiments at room temperature a higher concentration of hydrogen was obtained compared to previous experiments conducted at 185 or 200°C [71, 74]. At this higher temperatures the thin film phase diagram shows the presence of the solid solution α, whilst at room temperature, the precipitation of the $\alpha^{'}$ phase is expected [141].

3.1.5 RNR advantages and limitations

The waveguide method opens the possibility to study many different systems in a new way, as it ensures a series of advantages. First, the ΔQ_{res} depends only on $\Delta\rho_2$ which in turn depends only on the H concentration, as shown in Eq. (3.1), therefore no fitting procedure in required. Second, reflectivity measurements on a limited Q range are sufficient to monitor the Q_{res} position, therefore shorter measurements times are needed, allowing a dynamic study of the absorption process. Moreover, thanks to the waveguide enhancement, the dimensions of the sample could be reduced to only 5x5mm^2, without degradation of the experimental data. This is especially important for samples with more complicated growth, such as transition metal oxides or other complex materials. Another advantage of this technique is the limit of detection. While for conventional NR it is quite challenging to detect H in concentration below 5 at.%, due to the non-uniqueness of the possible models fitting the experimental curves, in the case of the waveguide method it is possible to significantly decrease this limit. The smallest c_H difference that can be detected is strongly dependent on the waveguide design and experimental conditions. In the Q-scan mode, the resolution corresponds to the smallest detectable shift of a peak. It is possible to further decrease this limit by using the fixed Q mode procedure described in the previous paragraph. The smallest detectable concentration in this case depends on standard deviation σ at Q* before H injection and can be calculated from Eq. (3.3) as follows:

$$c_{Hmin} = \frac{w}{2h} e^{1/2} \frac{Q_{res}}{8\pi \bar{N} b_H} \sigma \tag{3.4}$$

The sensitivity limit hence depends on the width and intensity of the resonance peak, with a sharper and more intense peak meaning a lower c_{Hmin}. This in turn depends on the measurement time t_{meas} chosen, because h=$R^{+-}_{Q*} I_0 t_{meas}$ and $\sigma = \sqrt{R^{+-}_{Q*} I_0 t_{meas}}$, with R^{+-}_{Q*} being the SF reflectivity at point Q* and I_0 the reflected beam intensity at critical edge. These relations show that it is possible to decrease the limit of detection in the presence of a stronger neutron source, with a bigger sample, with a sharper resonance or with increased time of measurement. However the counting time is restricted by the speed of the kinetics which is under study.

The sensitivity of RNR compared to unpolarized NR is about an order of magnitude better, where sensitivity is understood here as the smallest concentration detected in a given time. This is due to the fact that the shift of a sharp resonance peak is easier to detect than the relatively small changes induced by H loading in the NR curves. In order to get a quantitative comparison, we performed PNR and NR simulations, with the parameters of our experiments. Two models were included in the simulation, one with the pristine resonator sample described above and one with the 5 at.% of H, with ρ_{NbH}=3.81 10^{-6} Å^{-2}. The corresponding NR and PNR reflectivities are shown in Fig (3.8)a and b. The unpolarized curves and SF reflectivity R^{-+} of the polarized curves were then subtracted and compared with each other. The minimum time of measurement to detect a difference bigger than 2σ between pristine and H-doped sample was then calculated as follows:

$$t_{min} = \frac{4R}{(R - R_H)^2 * I_0} \tag{3.5}$$

where R and R_H are the reflectivities of the pure and 5 at.% H-doped Nb films at the same Q value, and I_0 is the incoming neutron intensity. In this calculation we used an incident intensity of the polarized beam $I_0 = 500$ counts per second (as obtained in our experiment at NREX), and took into account that I_0 for a non-polarized beam can be about three times higher. For such a small concentration of H, the only points of a non-polarized reflectivity curve that show a significant change are around the critical edge at Q=0.017Å^{-1} and at first minimum of the Kiessig oscillation, Q=0.021Å^{-1}, while obviously the biggest change in the spin flip channel during the polarized experiment are around resonance at Q=0.015Å^{-1}.

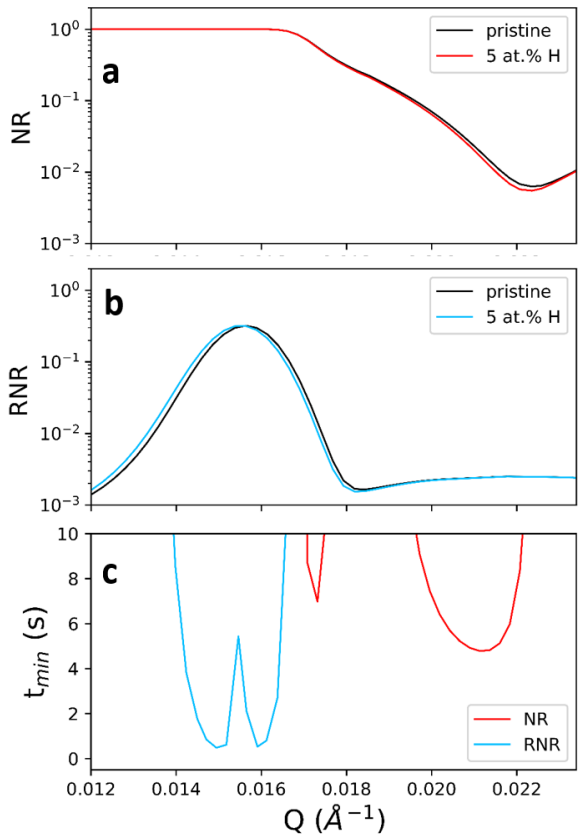

Figure 3.8: **a**. Simulated NR reflectivity curves for pristine sample and 5 at.% H loaded sample, **b**. Simulated SF of around resonance for virgin and 5 at.% H loaded sample. **c**. Minimum measurement time to resolve 5 at.% H-doped films in a conventional NR experiment (red) and PNR waveguide approach (blue).

As it is shown in Fig (3.8), even considering the most sensitive position of the conventional reflectivity curve, and accounting for the gain in intensity due to non polarized experiment (considered to be a factor of $\simeq$3, according to experiments conducted at NREX), the waveguide method ensures a gain of around one order of magnitude in the minimum time of measurement.

The limits of the RNR method are given by the dependence of the resonance peak position, not only on the SLD of the layer of interest, but also on the variation of its thickness and the H depth distribution within this layer. For this reason we propose that the RNR method should be use in synergy with conventional

Table 3.3: Comparison between methods for direct detection of hydrogen in thin films.

	Nuclear methods	Standard NR	RNR
In-situ absorption	no	yes	yes
Simultaneous probe of d	yes	yes	no
Non destructive	no	yes	yes
Kinetics (time resolution)	none	several minutes	seconds
Sensitivity limit	$\lesssim 0.1$ at.%	~ 5 at.%	~ 1 at.%

reflectometry. For example, in order to study fast absorption kinetics, the best mode of measurement is indeed the fixed-Q method. On longer timescales a series of Q-scans would allow to track the changes in intensity of the resonance peak, as expected for higher H content. Finally full reflectivity curves should always be measured at the beginning and end of absorption process in order to estimate the correction factors needed for RNR in case of swelling or inhomogeneous absorption.

Compared to the other previously mentioned techniques commonly used for H quantification in thin films, RNR is a direct method (contrarily to x-ray reflectivity and diffraction, that measure the film thickness variation upon H absorption [71,72, 76]), model-free (in contrast to NR), with no radiation damage and with possibility for *in situ* measurements (opposed to nuclear methods that employ high energy ions [147, 148]). The overall comparison with other direct methods is summarized in Table 3.3.

3.1.6 Conclusions and outlook.

We have demonstrated a new method for in-situ detection of hydrogen in thin films. It is based on the linear relation between the position Q_{res} of the resonant neutron field of a waveguide structure with the SLD ρ of the middle layer, which in turn is directly dependent on the absorbed hydrogen concentration. This method constitutes in a significant improvement with respect to previously used reflectometry methods, as it allows detection of smaller amounts of H and the study of faster dynamics of absorption, without the drawback of complicated data analysis. This method can be employed to establish the relation between absorbed H and the change of other physical properties, such as superconductivity or magnetic states

upon H uptake.

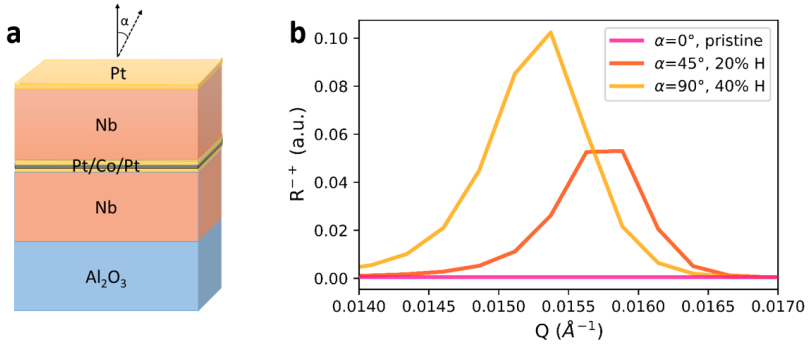

Figure 3.9: Tunable spin-orbit coupling via hydrogen absorption studied via RNR. **a**. Sketch of proposed sample and definition of the angle α for Co magnetization direction. **b**. PNR simulation around resonance position for different magnetization orientations and hydrogen concentrations.

For example, the magnetic anisotropy of a thin ferromagnet (FM) sandwiched between two heavy metal layers has been shown to become perpendicular (PMA) due to spin-orbit coupling below a certain thickness of the ferromagnet layer in various systems [6, 149]. The possibility to switch such PMA upon absorption of hydrogen or deuterium has been demonstrated in Pd-Co [150], and in Pt-Co systems [151]. More recently, this effect has also been implemented in an all-solid-state device, which achieves reversible and non-destructive toggling of magnetic anisotropy at room temperature [83]. Waveguide enhanced polarized neutron reflectometry (RNR) experiments are particularly suited to study such systems, due to the high sensitivity to hydrogen concentration and magnetization direction. Figure 3.9a shows the proposed waveguide structure that encapsules the Pt-Co-Pt trilayer of interest. Figure 3.9b shows RNR simulations of the waveguide peak evolution in the sketched sample upon H absorption into Nb. For the pristine sample (pink curve) no waveguide peak is expected in the SF channel, due to initial out-of-plane magnetization. However when H is loaded into the Nb layer and reaches the upper Pt of the trilayer system, the spin-orbit coupling at the Pt-Co interface is suppressed, and the magnetization starts to turn in-plane, giving rise to spin-flip scattering with enhancement at resonance position (red curve). While the magnetization is changing direction, the in-plane component will increase, changing

the intensity of the resonance peak (orange curve). By employing RNR on this system we are hence able to decouple the information about the angle α between the surface normal and magnetization direction, and the hydrogen content c_H. α is encoded in the intensity of the SF peak, while c_H is quantified through the its momentum transfer Q_{res}.

3.2 Kinetics of H absorption in Nb films with RNR

Following the proof of principle experiments, several follow up measurements have been performed on a series of waveguide samples, deposited at the JCNS MBE setup, of composition Al_2O_3/Nb(x)/Co(3nm)/Nb(x)/Pt(3nm), with x=11, 27.5 and 55 nm. The aim of these experiments was to study the relation between the kinetics of hydrogen absorption versus different pressures of $Ar_{98\%}H_{2\%}$ mixture in the sample chamber, versus different thickness of Nb layers, and versus the epitaxiality of the film. Thanks to the unique possibility offered at NREX, PNR and XRR were measured simultaneously, *in situ* during H absorption. Additional RNR measurements were performed at V6. The main observation was that for the highest pressure we have a faster kinetics, and that thicker films require longer time to complete the hydrogenation process. The much slower loading process observed for epitaxial films, compared to polycrystalline ones, reveals a defect driven absorption. In polycrystalline films, the comparison between kinetics observed from XRR and PNR indicates a two-step process, where the films first swell, due to the intercalation of hydrogen in grain boundaries, and then continue the in-grain absorption on longer timescales.

Other parameters that in the future will be interesting to explore in relation to the kinetics of absorption are the roughness of Pt layer on top, and the use of different catalyst (Pt and Pd) on the surface.

3.2.1 Sample design, growth and preliminary characterization

A series of samples of composition Nb(x)/Co(3nm)/Nb(x)/Pt(3nm), with x=11, 27.5 and 55 nm, was grown by molecular beam epitaxy on Al_2O_3 substrates of area 10 x 10 mm^2. A sketch of the design is presented in the Inset of Figure 3.10. The substrates were previously cleaned with ethanol and isopropanol, and annealed at 1000°C for 2-3 hours in ultra-high vacuum. The deposition of the layers took place at room temperature for all samples. The rates of deposition were 0.4 Å/s, 0.1 Å/s, and 0.2 Å/s for Nb, Co and Pt respectively.

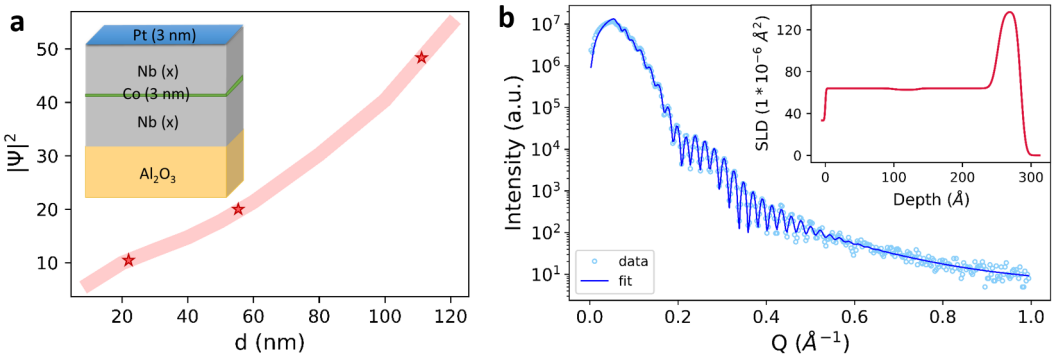

Figure 3.10: Sample structure design and preliminary characterization. **a**. Numerically calculated maximum neutron density enhancement (with respect to the incoming beam with $|\Psi|^2 = 1$) versus niobium thickness d=2x. The red stars represent the thickness chosen in this study. A sketch of the thin-film structure is represented in the upper corner of the panel. **b**. X-ray reflectivity of the as-prepared sample 22-b and fit. Inset: SLD profile obtained from fitting.

The choice of thicknesses and substrate followed the rules for formation of a waveguide structure, which include the need of a high contrast between substrate and middle layer, and a wide enough potential well where the neutrons can be trapped. The simulation depicted in Figure 3.10a shows the resonant enhancement of the neutron density for different niobium thicknesses, which shows how the efficiency of the waveguide structure increases for thicker films. The presence of a Co layer with magnetization aligned along the easy axis (110), hence non-collinearly to the external field allows the detection of the resonant field in the SF scattering channel, as explained before. The thin Pt layer was grown on top of the structure to enable the splitting of H_2 molecules on the surface.

The samples were preliminarily characterized by x-ray diffraction, which showed polycrystallinity of all the films grown at room temperature with preferential orientation along the (110) plane. The sample grown at high temperature (ID 55-c) showed epitaxial growth along the (200) plane. For all samples the pristine state was measured at room temperature with XRR, as shown in Figure 3.10b. The fit of XRR data shows a good match between nominal and observed parameters. The thickness of Nb layers is reported in Table 3.4, and Pt thickness 33.5 Å. Due to the low contrast between Nb and Co for x-rays, the Co thickness was kept fixed for

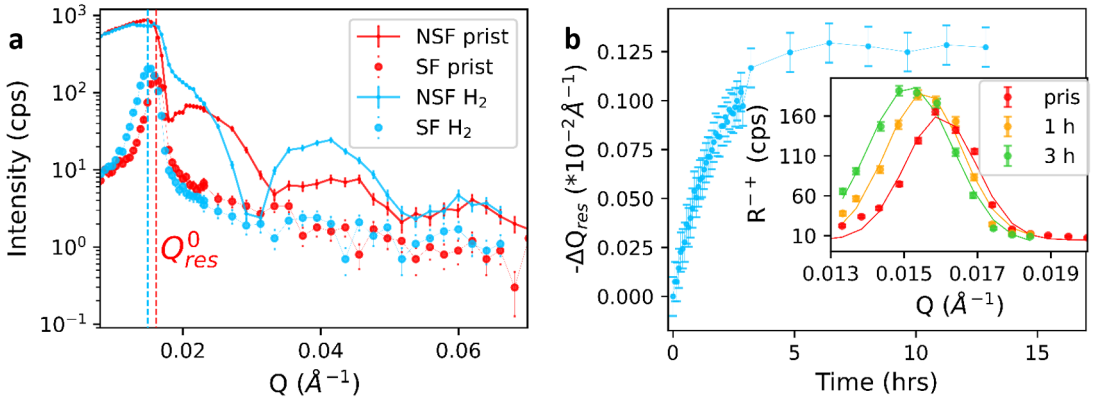

Figure 3.11: PNR and RNR experiment on sample 22-b upon exposure to 6.4 mbar of $Ar_{98\%}H_{2\%}$. **(a)**. PNR measurement showing one NSF and one SF channel of the pristine (hydrogenated) sample shown in red (blue). The dashed lines indicate the position of resonance before and after absorption; **b**. Shift of the resonance versus time measured with RNR. Inset: Q-scan measurement during H absorption.

all samples at 34.5 Å, which was consistent with PNR data. All roughness values obtained are well below 10 Å, indicating a good quality of the interfaces.

3.2.2 Experimental details

RNR measurements

The experimental setup was similar to that described previously, with the magnetization of the film lying along the easy axis at around $\simeq 45°$ with respect to the low field $H = 5G$ applied throughout the measurement. The samples were placed in a sealed chamber, vacuumized to 10^{-3} mbar and subsequently exposed to different $Ar_{98\%}H_{2\%}$ gas pressures. Before and at the end of the absorption process, long reflectivity curves with full polarization analysis were taken, in order to be able to fit all relevant parameters, such as thickness and SLD. One example of pristine and fully hydrogenated curves is shown in Figure 3.11a. The presence of the sharp resonance peak allows for a more precise fitting procedure, with more constraints for the fitted variables.

The tracking of *in situ* hydrogen absorption via RNR was made following the

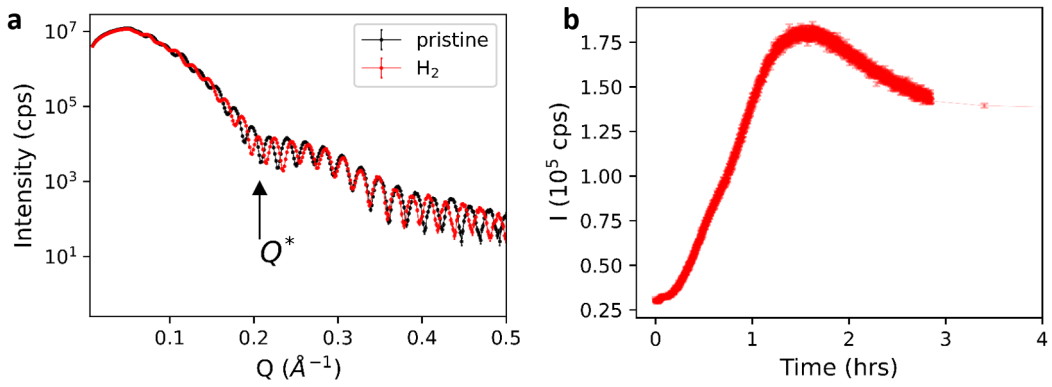

Figure 3.12: simultaneous XRR experiment of sample 22-b. **(a)**. XRR measurement of the pristine (hydrogenated) sample shown in black (red). The arrow indicates the chosen position for the fixed-Q timescan; **b**. Fixed-Q timescan of X-ray intensity versus time during H absorption.

procedure explained in the previous section. A series of Q-scans to measure the SF reflectivity R^{-+}, around Q_{res} was taken and subsequently fitted to a Gaussian profile, as shown in the inset of Figure 3.11b. This allows us to follow the resonance shift in time (Figure 3.11b), which in turn gives us information about the kinetics of absorption. The errorbar on ΔQ_{res} corresponds to $\pm\sigma$ of the fit of the peak center. Approaching saturation, a series of longer reflectivity curves was measured, in order to fit and extract the H content above 30 at.% in a precise way. The resonance shifts measured in the full PNR curves are included in Figure 3.11b (points above 3hrs), in order to have an overview of the kinetics of absorption over several hours. For low H concentration (c_H <30 at.%), where we expect negligible film expansion and small profile changes, it is possible to apply formula 3.1 and retrieve the accurate H content in the Nb layer.

XRR measurements

For the experiments carried out at NREX, a simultaneous XRR measurement was performed, to compare the two different methods. As for the neutrons, a full XRR curve at the beginning and end of process was measured, as shown in Figure 3.12a. We tracked the changes in reflectivity during the exposure to hydrogen pressure by

Table 3.4: Summary of parameters obtained from fitting of experimental data.

ID	d (nm)	p (mbar)	Final ρ_{Nb} (10^{-6} Å^{-2})	Δd/d %	c_H (at.%)
22-a	21.6 ± 0.6	4.0	2.61 ± 0.15	4.6	53.1
22-b	21.6 ± 0.6	6.4	2.20 ± 0.1	8.8	69.8
22-c	21.6 ± 0.6	8.0	2.50 ± 0.5	5.9	57.8
22-d	21.6 ± 0.6	10.5	2.27 ± 0.1	8.3	67.1
22-e	21.6 ± 0.6	22.0	2.13 ± 0.2	9.6	74.0
55-a	54.4 ± 0.4	8.0	1.93 ± 0.2	8.2	85.7
55-b	47.6 ± 1.0	8.0	2.05 ± 0.1	8.1	80.9
55-c	48.6 ± 0.2	8.0	2.10 ± 0.05	8.4	78.7
110-a	111.7 ± 1.4	8.0	1.87 ± 0.2	9.8	88.5
110-a	122.7 ± 3.2	8.0	1.90 ± 0.2	7.8	89.2

staying at a fixed momentum transfer Q*, corresponding to an arbitrary minimum of Kiessig oscillation. After approaching the saturation of the absorption process (after 2.8 hours in Figure 3.12b), we recorded a series of full XRR to have more insight on small changes of the Nb or Pt layers.

3.2.3 Results

Each sample was exposed to the gas mixture at room temperature and the kinetics of absorption were tracked by RNR and, where possible, with simultaneous XRR. Full XRR and PNR curves allowed to keep track of initial and final states. The hydrogen content was recovered using formula 3.6, which takes into account the niobium density variation upon absorption as fully derived in [76].

$$c_H = \left(\frac{\rho_{NbH}}{\rho_{Nb}} \frac{d_H}{d} - 1 \right) \frac{b_{Nb}}{b_H} \tag{3.6}$$

A summary of the most important parameters retrieved can be found in Table 3.4.

Pressure-dependent kinetics of absorption

In order to study the pressure-dependent kinetics of absorption, we considered the thin waveguide design Nb(11nm)/Co(3nm)/Nb(11nm)/Pt(3nm). The samples were grown simultaneously in order to ensure the same initial state and were

subsequently exposed to different gas pressures. The first observation from the fit of the curves measured at the end of the absorption process (found in Table 3.4 under ID=22-n) is that all Nb films have reached a similar hydrogenated state, with around 60-75 at.% of H absorbed, with the exception on the one were the smallest pressure of 4mbar of gas was used. In this case the data suggests that the thin layer was hydrogenated up to a significantly lower degree of 50 at.% of hydrogen.

An overview of the absorption kinetics can be seen in Figure 3.13, where the shift of resonance through Q-scan RNR and XRR measurements was tracked. The shift ΔQ_{res}, shown in panel a of Figure 3.13, strongly increases as the niobium becomes hydrogenated. For all applied pressures the plateau in the shift corresponds to the saturation of absorption process, with no more measurable changes in the ρ of Nb. By fitting the experimental data to an exponential curve (solid lines in Figure 3.13a) of Eq.3.7

$$c_H = A - C * \exp(-\frac{t - t_0}{\tau}) \tag{3.7}$$

with A, t_0 and C free parameters, we are able to define the time constant τ, which we can use to characterize the kinetics of absorption. The exponential law is in this case an empirical choice used to define a time parameter for all measurements.

Interestingly we observe that τ decreases rapidly with increasing gas pressure. In particular we found a phenomenological linear dependence between the τ and the inverse natural logarithm of the pressure, as shown in the inset of Figure 3.13c. This reflects the chemical potential gradient of final and initial state, consistently with previous results reported by Song et al. in [65].

An additional pressure point was measured with unpolarized, conventional NR: the intensity was tracked by staying at the fixed Q corresponding to the first Kiessig oscillation minimum. Since the intensity depends both on Nb thickness and SLD, the fixed-Q NR method is of more difficult interpretation, and does not allow for a quick hydrogen quantification, in contrast to RNR. Nevertheless, we were able to define a time constant which is consistent with the τs retrieved from RNR, shown in Figure 3.13c with a star-symbol.

Figure 3.13b shows the XRR timescan comparison at different pressure points.

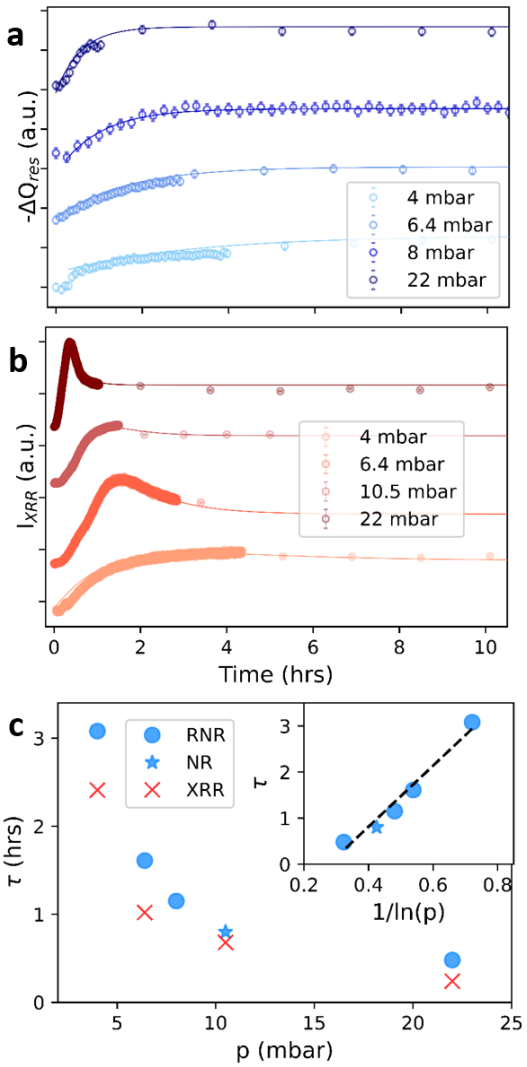

Figure 3.13: Simultaneous RNR and XRR measurements at different $Ar_{98\%}H_{2\%}$ mixture pressures. **a**. Shift of ΔQ_{res} obtained from RNR measurement at different pressures; **b**. Fixed-Q XRR measurements at different pressures; the solid lines correspond to the best exponential fit of experimental data. **c**. Time constant calculated from RNR and XRR versus gas pressure. Inset: Linear dependence of the τ and the inverse of the natural logarithm of pressure.

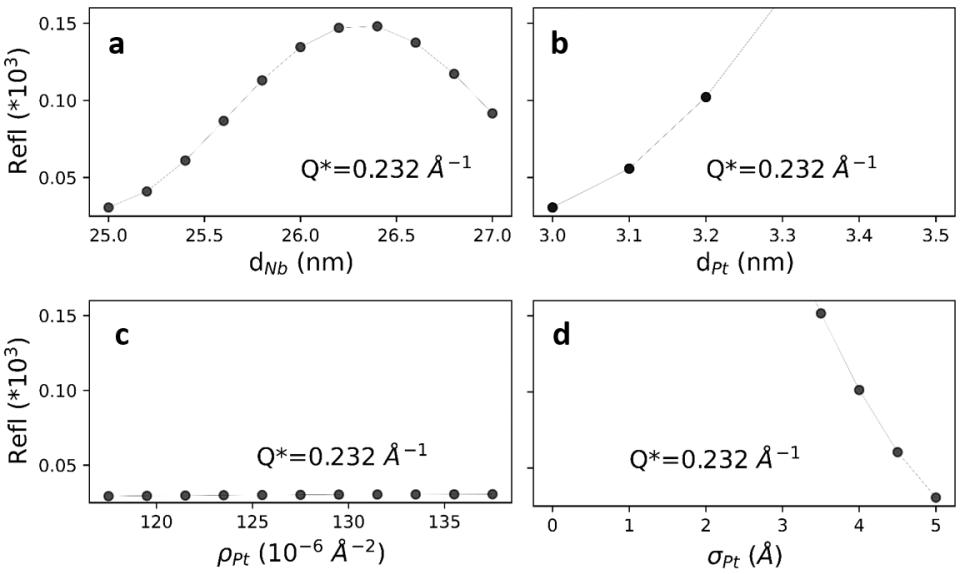

Figure 3.14: Simulated XRR intensity dependence at fixed Q*=0.232 Å^{-1} on Nb thickness (**a**), Pt thickness (**b**), Pt scattering length density (**c**), and Pt roughness σ_{Pt} (**d**).

In this case we can observe that the signal is non monotonous. Contrarily to RNR, where to a first order approximation the shift depends solely on the SLD of the absorbing layer, here the measured intensity depends in principle on all the layers SLD and thickness. However, due to the low sensitivity of XRR to hydrogen atoms, the only parameters that actively modify the XRR upon hydrogen absorption are the Nb thickness (swelling of niobium film) and Pt thickness, ρ, and roughness in case of hydrogen induced modifications of the catalyst layer. We have performed XRR simulations to understand how these different parameters modify the fixed-Q intensity, taking into account a simple system composed of a thin Pt (3nm) and a Nb (25nm) layer on top of sapphire substrate. The chosen fixed Q* corresponded to the minimum of both Pt and Nb Kiessig oscillation, to optimize the response to changes in both layers. When the Nb thickness increases, the frequency of the corresponding Kiessig oscillations increases (according to Figure 2.2), effectively shifting the previously chosen minimum to lower Q values. As a result of this effect, during a fixed Q timescan, the reflected intensity changes so that we climb and descend upon such oscillations, as shown in Figure 3.14a. We found a strong

monotonic dependence of the XRR intensity on Pt thickness and roughness (Figure 3.14b, d) but almost no dependence on the Pt ρ at this Q* (Figure 3.14c). However, the effect of the thin catalyst layer can be disregarded in our case, since the fit of initial and final XRR curve shows that Pt is unchanged upon hydrogen absorption. In summary, with fixed-Q XRR we observe strong changes appearing as peak in the beginning of the absorption process that are due to the Nb thickness change. The amplitude of this peak depends both on the pressure, but also on the arbitrary Q* chosen in the experiment.

In order to extract a time constant from these fixed-Q measurements, we fitted the XRR intensity with the model defined in Eqs. 3.8-3.9. Eq.3.8 models one Kiessig fringe of the XRR locally close to $Q*$. This Gaussian is then shifted in time by $Q(t)$. The latter is proportional to the thickness d_{Nb} of the Nb layer, which we assume to saturate according to an exponential with time constant τ_{XRR} (Eq.3.9). This model both describes the simulation in Figure 3.14a and the experimental intensities in Figure 3.13b, and permits to extract the time constants τ_{XRR}.

$$I_{XRR} \propto \exp\left(-2 * \left(\frac{Q^* - Q(t)}{w}\right)^2\right) \tag{3.8}$$

$$Q(t) = Q_c - dQ\left(1 - \exp\left(-\frac{t - t_0}{\tau_{XRR}}\right)\right) \tag{3.9}$$

As a result, for XRR as well as for RNR, we observe faster changes at the maximum gas pressure applied. τ_{XRR} however, appears systematically lower than τ_{RNR}, as represented in Fig 3.13c. We will address this point in the Discussion section.

Thickness-dependent kinetics of absorption

The series of waveguide samples Nb(x)/Co(3nm)/Nb(x)/Pt(3nm), with x=11, 27.5, 55 nm, was exposed to the same gas pressure of 8 mbar of $Ar_{98\%}H_{2\%}$ mixture in order to study the dependence of kinetics on the Nb thickness. A summary of the kinetics of absorption on different samples is shown in Figure 3.15. The shift of resonance was tracked *in situ*, showing a slower kinetics with increasing thickness.

Both from the RNR method, and from full PNR fitting, we observe that the hy-

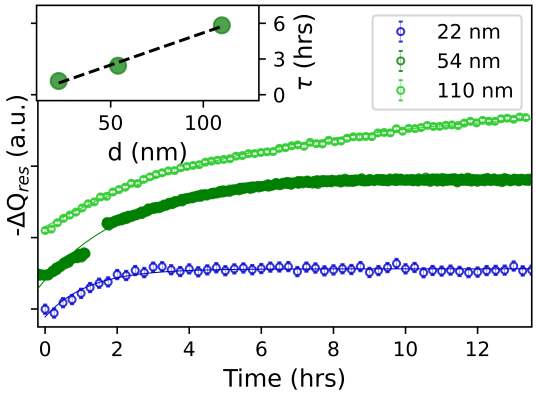

Figure 3.15: RNR measurements of different sample thicknesses. Shift of ΔQ_{res} obtained from RNR measurement, the solid lines correspond to the best exponential fit of experimental data. Inset: Time constant calculated from RNR versus sample thickness.

drogen content is lower for the thinner design, and saturates for thicker waveguides above 50 nm around 85 at.%

In the inset of Figure 3.15 we show the time constant τ, versus niobium thickness. From this analysis we observe that τ increases linearly with increasing layer thickness.

Crystallinity-dependent kinetics of absorption

The dependence of the kinetics of absorption on the crystalline quality was studied at room temperature at fixed pressure of 8 mbar of $Ar_{98\%}H_{2\%}$ mixture. The samples under study were of thickness Nb(27.5nm)/Co(3nm)/Nb(27.5nm)/Pt(3nm), and were grown at different conditions to modify their degree of crystallinity. The sample with ID 55-b was grown with the substrate kept at room temperature, hence ensuring a policrystalline structure, as shown in Figure 3.16a. The sample 55-c was grown with a substrate temperature of 800°C, which enabled epitaxial growth, as shown in Figure 3.16b. Due to the high growth temperature, we observed a high inter-diffusion of niobium and cobalt atoms, which resulted in the loss of the coherent magnetic layer, needed as the resonant field label. For this reason the kinetics of absorption was not followed with RNR, but with a fixed-Q NR measurement, as explained in the previous sections. In Figure 3.16c we compare

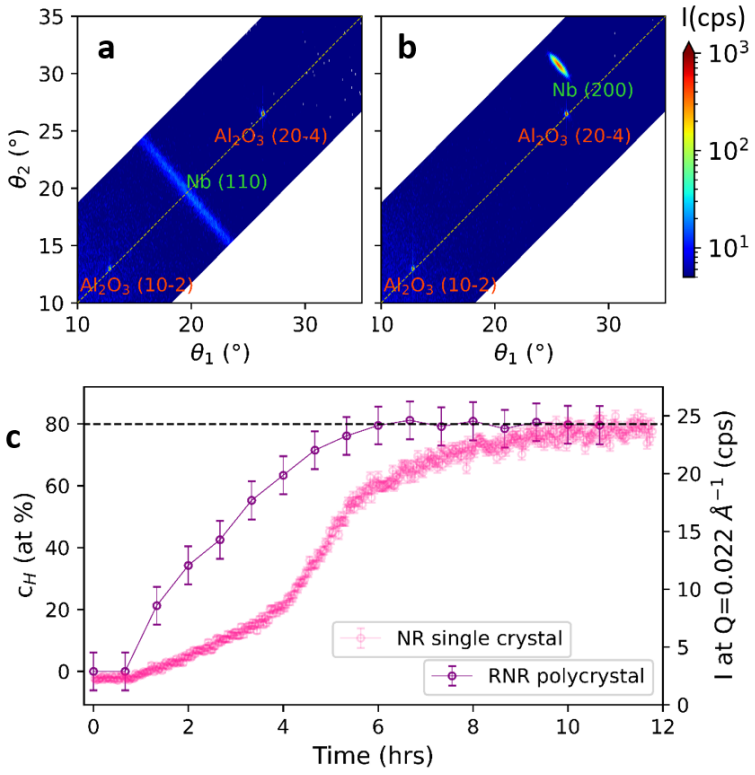

Figure 3.16: Comparison between epitaxial and policrystalline Nb kinetics of absorption. **a**. X-ray scattering map of sample 55-b showing polycrystallinity; **b**. X-ray scattering map of sample 55-c showing epitaxiality; **c**. Comparison of kinetics of absorption at RT and pressure 8 mbar for sample 55-b (purple) and 55-c (pink).

the RNR and NR kinetics studied measured on the policrystalline and epitaxial samples, respectively. The NR signal (pink dots) is once again non monotonous and of more difficult interpretation, due to the complex dependence of the NR intensity on all time-dependent parameters. Nevertheless, on a qualitative point of view, we can observe that the epitaxial sample reaches saturation after circa 9 hours, around 3 hours later than the polycrystalline sample. This observation suggests that defects speed up the hydrogenation process.

3.2.4 Discussion

Contrarily to previously published results where the hydrogen absorption was studied at around 200°C [74, 76, 142, 143], we show the hydration of niobium at room temperature, where a separation between α and β phases is expected, as shown in the bulk phase diagram reproduced in Figure 3.3a. The final hydrogen concentration found in our films after H exposure, listed in Table 3.4, shows that all Nb films, with the exception of sample 22-a, contain an average amount of hydrogen consistent with that expected for the phase β. In thin films, however, one has to take into account that the phase diagram might differ significantly from the bulk. For example, the strong clamping of niobium to the Al_2O_3 substrate [152] can impede the formation of the orthorhombic β phase observed in bulk [139]. Nanoconfinement effects at interfaces and defects as well cannot be neglected when considering solid solutions in thin films [153–155].

A different phase diagram was proposed for niobium thin films, where β phase formation is suppressed and the phase precipitation between α and α' solid solution is expected at substantially lower temperature compared to bulk films, decreasing with film thickness [71, 139–141]. An example of such phase diagram for 20 nm thick films is shown in Figure 3.3b, where the equilibrium conditions between α and α' phases at RT is shown.

A hint on the formation of a new thermodynamically stable phase after H exposure is the irreversibility upon removal of hydrogen gas pressure in an observable time scale (months), indicating that the hydrogen is trapped in the film. Consistently, we also observe that the hydrogenated samples do not show any superconducting properties down to 4 K (Figure 3.17a).

In order to desorb hydrogen from the samples, annealing at high temperature (600 K) and under vacuum for several hours was necessary. RNR and XRR measurements confirmed that the annealing was successful in removing the hydrogen, at least partially as shown in Figure 3.17b and c, with ρ and thickness of Nb restored to the initial values. In Figure 3.17b we observe that the resonance peak after the annealing (black line) has an intermediate Q_{res} between the values for the pristine and hydrogenated sample, and that the broadening is the same as that found for hydrogenated sample. This is an indication that the average ρ_2

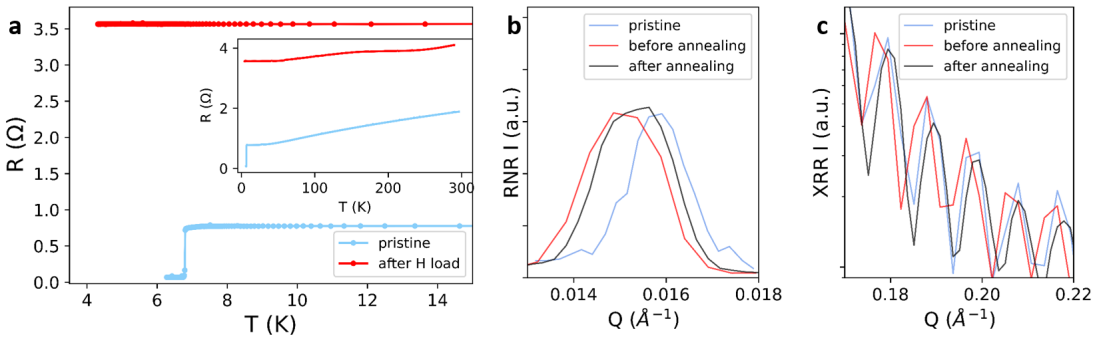

Figure 3.17: Superconducting transition and annealing procedure. **a**. Temperature dependent resistance before and after RT H exposure of a Nb(27.5)/Co(3nm)/Nb(27.5)/Pt(3nm) sample. Inset: Full temperature range of measured transport properties; **b**. *In situ* RNR measurement before and after the annealing at 600 K; **c**. *In situ* XRR measurement before and after the annealing at 600 K.

has not restored to the value of pristine niobium, either due to the presence of residual hydrogen in defects, or due to a decreased density left by voids after absorption. This second possibility is in contradiction with the XRR data, shown in Figure 3.17b, that indicate the full restoration of the thickness of the pristine sample after annealing. Nevertheless, after the annealing it was impossible to load hydrogen again, which we interpret as the result of a broken contact at the interface between the catalyst Pt and the neighbouring Nb layer. Another striking difference with high-temperature hydrogen exposure is the considerably slower kinetics at room temperature for similar thickness and pressure [74, 142]. This kinetics cannot be explained via the bulk diffusivity of hydrogen in the host material, since hydrogen should travel through 50 nm of niobium in less than 5 μs. Song et al. [71] reported a drastic increase of the relaxation times approaching the phase transition critical point, suggesting in our case as well the precipitation of α' phase. The exponential time dependence of the observed kinetics is consistent in the Johnson–Mehl–Avrami–Kolmogorov (JMAK) model of the recrystallization of metals [156–159]. In this respect, a similar model of the hydrogenation kinetics was applied in thin CoPd films [160], where the authors showed an irreversible swelling of the films in a time range of hours, similarly to our case.

The combination of all these observations suggests that the process happening during our RT measurements is the slow hydrogenation of niobium to form a new stable phase. The identification of this phase as the expected α' must still be confirmed via XRD measurements (Refs. [161, 162]), but x-ray photo-electron spectroscopy (XPS) performed on hydrogenated samples allowed us to exclude the formation of hydride β phase, due to the absence of peaks corresponding to the Nb-H binding energy.

Precipitation crystallites are expected to nucleate around lower activation energy sites, such as grain boundaries or dislocations, and to subsequently expand towards the centre of grains. Henceforth, we can describe hydrogen absorption as a defect-driven process and therefore we expect the kinetics to be strongly dependent on the amounts of defects present. This was confirmed by our comparison of epitaxial and polycrystalline samples, where two films of the same thickness but of different crystalline quality were exposed to the same $Ar_{98\%}H_{2\%}$ mixture pressure (Figure 3.16). Given that all the remaining samples are polycrystalline and showed a similar final hydrogen content and thickness swelling, it is reasonable to assume that the number of grain boundaries and other defects are proportional to the volume of the film, hence a thicker film will have more defects. This is consistent with our thickness dependence study, that showed the time τ to be linearly proportional to the d of niobium.

The pressure dependence study as well allows us to draw conclusions on the mechanism of hydrogen absorption at room temperature. In our simultaneous XRR and RNR measurements we have observed systematically higher saturation times with neutrons than with X-rays. In Figure 3.18a we compare the exponential curves described by τ_{XRR} (solid red) and τ obtained from RNR (solid blue line) at the same pressure point. We have highlighted with star symbols the end of absorption process, which was defined as 3τ, at which the signal has reached the 95% of its saturation value. Here we can observe that when the XRR signal saturates, the RNR still shows non-negligible changes. In order to explain this, we must take into account which physical variable the measurements are sensitive to: while with x-rays one only sees thickness changes, neutrons are instead sensitive also to the absorbed H atoms. We can hence explain our result if we assume that the swelling of Nb layer saturates at $3\tau_{XRR}$, while more H can still

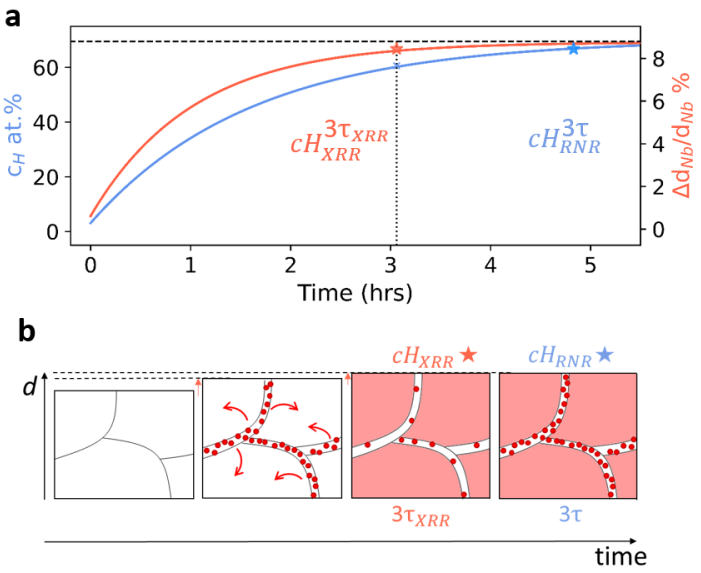

Figure 3.18: Comparison between kinetics obtained from XRR and RNR of sample 22-b and schematics of the process of absorption. **a**. RNR and XRR at p=6.4 mbar. The solid lines show exponential curves obtained from RNR and XRR measurements. The stars indicate the point at which the exponential reaches a value corresponding to 3τ, the horizontal dashed black line shows the saturation level; **b**. Simplified diagram of the proposed absorption process at room temperature.

be absorbed beyond 3τ. We can simplify the hydrogenation of niobium films at room temperature according to the schematics represented in Figure 3.18b. At the beginning of the process, hydrogen atoms dissociated at the Pt interface travel through the underneath niobium, increasing its overall thickness. We can expect H atoms to accumulate on grain boundaries (second panel in Figure 3.18b) and from there start the nucleation for the new phase. The observed increase in Nb thickness Δd/d, of around 8% for all samples, is substantially bigger than the expected interplanar spacing of 4% [76]. This indicates that the majority of the observed swelling is due to hydrogen accumulating in defects or voids present, as previously suggested by Rehm et al in [76]. The irreversible swelling is also the evidence of plastic out-of-plane expansion, consistent with the reports for room temperature hydrogenation of Nb films [163]. At a time corresponding to $3\tau_{XRR}$ (third panel in Figure 3.18b), the expansion of the lattice is terminated, as all

the grains have undergone phase transition. The niobium contains at this point a hydrogen content called here $cH^{3\tau}_{XRR}$. However a non-negligible amount of hydrogen, corresponding to $cH^{3\tau}_{RNR}$-$cH^{3\tau}_{XRR}$, can still enter the structure in the voids left at the grain boundaries after hydrogen moved towards the centre of grains. This measurement shows the complementarity of information obtained from X-rays and neutrons.

3.2.5 Conclusions

We have shown the thickness dependent and pressure dependent hydrogen absorption kinetics in niobium thin films at room temperature by means of resonant neutron reflectometry. RNR allowed us to follow the H content *in situ*, giving insights on the saturation time of the films upon exposure to H atmosphere. We have shown that the films are able to withhold high amounts of hydrogen, undergoing a phase transition which is irreversible at room temperature. The speed of the kinetics, expressed in terms of time constants, was shown to be linearly dependent both on the thickness, and on the external pressure of gas. The differences of time constants measured by XRR and RNR, which still shows changes after XRR has reached saturation, hint on a defect-driven hydrogenation process, where the film stops swelling even though it is still absorbing hydrogen. The comparison with *in situ* XRR measurements showed the potential of using both techniques simultaneously, allowing for a deeper understanding of the absorption process.

Chapter 4

Modulated doping of complex oxide films

Creating novel electronic states by reduced dimensionality of a system is one of the core concept of nanotechnology. In the case of thin films a lot of effort is directed to the realization of highly tunable electronic properties, mainly for M-RAM and spintronics applications. One of the main advantages of using oxides as constituent materials for devices, apart from the high structural quality, is the adjustability of electronic properties via electron or hole doping, giving access to rich phase diagrams. This lead to the discovery of peculiar physical phenomena which are not achievable in elemental metals, such as colossal and tunnel magnetoresistance, high spin polarization, and high temperature superconductivity. In this chapter we report on the design and realization of a system with a highly tunable non-collinear magnetization, realized in a manganite homojunction. This system was characterized by magnetometry, XRR, PNR and magnetotransport measurements.

The main experimental sections will follow to show the results presented in Ref. [164].

4.1 Emergent non-collinear magnetism in manganite homojunctions

4.1.1 Sample design and growth

The samples under study are manganite homojunctions with depth modulated doping, where the carrier leaking across interfaces allows to tune the magnetic nature of the whole structure. We chose $La_{1-x}Sr_xMnO_3$ (LSMO), which allowed us to exploit its rich phase diagram [165, 166], shown in Figure 4.1a. The Sr-doping was varied between the nominal values of optimally-doped x=0.4 (half-metallic ferromagnet (FM) with the Curie temperature of 382.6 K) and overdoped x=0.8 (insulating C-type antiferromagnet (AF)), as shown in the sketch in Figure 4.1b. The thickness of the FM layer, d, was kept constant at 9 monolayers (MLs) (1 ML =3.87 Å), while the thickness of the overdoped layer was varied in the range of n = 1-9 MLs. In the following we will refer to each sample by the thickness of overdoped layer, for example the sample with n=6 will be called $N6$. This doping scheme provides not only a simpler growth procedure with reduced number of elements in the final structure, but also guarantees good electrical transport properties thanks to the suppression of interface scattering between the two very similar layers.

The samples of nominal composition 10 x [$La_{0.6}Sr_{0.4}MnO_3(d)$+ $La_{0.2}Sr_{0.8}MnO_3(n)$] were grown using ozone assisted molecular beam epitaxy (MBE) at the Max Planck Institut für Festkörperforschung (MPI-FKF). The layer-by-layer deposition was monitored by *in situ* RHEED, to control the thickness and crystallinity of the epitaxial layers. Samples were grown on a $(LaAlO_3)_{0.3}(SrAl_{0.5}O_3)_{0.7}$ (LSAT) substrate of dimensions 10x10 mm^2.

4.1.2 X-ray reflectometry

The samples were structurally characterized with room temperature x-ray reflectometry (XRR) measured at the Kara Karlsruhe Research Accelerator (λ=1.238 Å). Figure 4.2a shows an example of an XRR curve from the sample $N6$. The main observation, common to all samples, is the presence of superstructural Bragg peaks, denoted as $(00n)_{SL}$, which arise from the periodicity given by the modula-

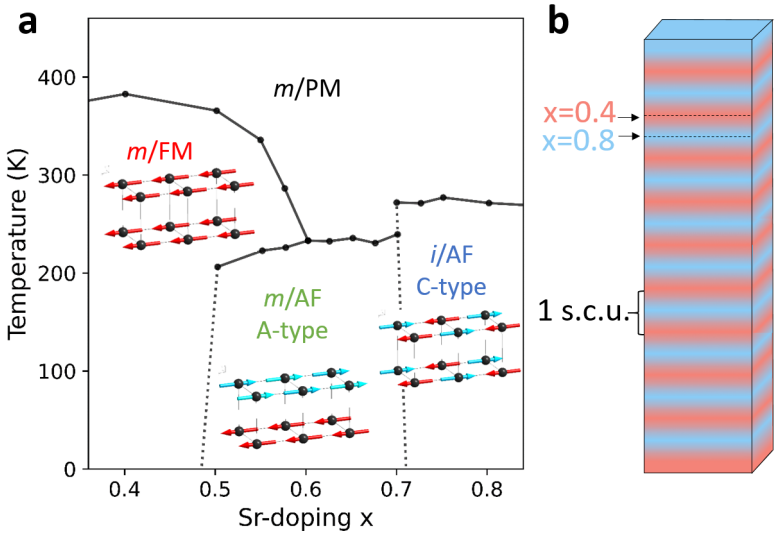

Figure 4.1: Phase diagram and schematic representation of the depth-modulated SLs. **a**. Bulk phase diagram of $La_{1-x}Sr_xMnO_3$ with data points taken from [165], where m/i stands for metallic/insulating, and PM/FM/AF indicate the paramagnetic/ferromagnetic/antiferromagnetic phase; **b**. Sketch of the samples design and definition of s.c.u., where the zero is set in the center of the optimally doped (x=0.4) layer.

tion of the Sr-concentration. By fitting a model structure to the XRR curve, we obtained the depth profile of the structural scattering length density (SLD) shown as a solid line in Figure 4.2b. Here we refer to the super-cell unit (s.c.u.) as our repeating unit cell composed of one FM layer and one overdoped layer. The fit suggested a strong Sr-diffusion, with a transient layer extending up to 3-4 MLs ($\approx$ 15 Å). Moreover the smearing was found to be asymmetric with respect to upper and lower interfaces, suggesting a preferential diffusion of Sr-ions towards the growth direction, as previously observed in other systems [30]. The smearing of interfaces was confirmed by comparison to a second model with sharp interfaces (dotted line in Figure 4.2a,b), which showed a poor match with the experimental data.

The smearing of SLD profile observed can be explained by either actual Sr/La inter-diffusion across the layers, or by charge transfer from the overdoped to optimally doped layers. Since x-rays are sensitive to the electron density, we can shed

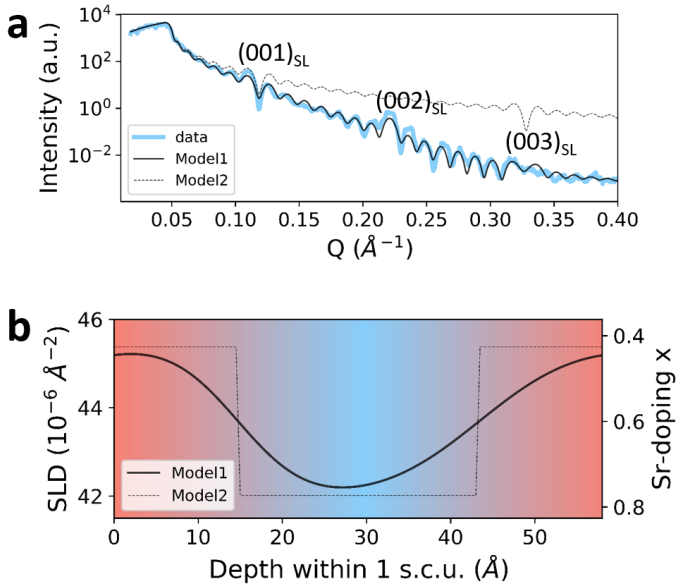

Figure 4.2: Structural characterization of the SLs via XRR. **a**. Experimental XRR of sample $N6$ (light blue), best fit obtained with Sr-diffusion model (black), simulated curve obtained with no diffusion model (dashed black); **b**. SLD depth profile of one s.c.u. of the Sr-diffusion model (black) and no Sr-diffusion model (dashed black), showing the corresponding Sr-doping.

light on this smearing mechanism. The optical contrast in terms of scattering length b between optimally and overdoped LSMO is proportional to the difference between the number of electrons in the two layers:

$$\Delta b \propto \Delta e^{-}. \tag{4.1}$$

Sr and La have 38 and 57 electrons, of which 2 and 3 in the valence band, respectively. For the optimally doped LSMO(x=0.4) the average number of (valence) electrons on the A site thus is (2.6) 49.4, while for LSMO(x=0.8) is (2.2) 41.8. The nominal difference Δe^{-} is of 7.6 total electrons and 0.4 valence electrons, which are those contributing to the Mn oxidation state. If we assume a total smearing of Sr/La A site occupation and only charge transfer effects, the contrast between the layers should come only from the 0.4 valence electrons, while if there is an actual modulation of Sr-doping, the contrast should be much higher and

proportional to the 7.6 total electrons. To compare the experimentally obtained optical contrast Δb_{fit} of sample $N6$ to the nominal one with no smearing effects $\Delta b_{0.4-0.8}$, we can then write the following expression:

$$\Delta b_{0.4-0.8} : \Delta e^-_{0.4-0.8} = \Delta b_{fit} : \Delta e^-_{SL} \tag{4.2}$$

which gives

$$\Delta e^-_{SL} = \frac{7.6e^- \cdot 0.2fm^{-1}}{0.19fm^{-1}} = 7.2e^-. \tag{4.3}$$

Here the scattering lengths are calculated as $b = (SLD \cdot MM)/(\delta \cdot N_A)$, with δ the density in g/cm^3, MM the molecular mass in g/mol, and N_A the Avogadro number. The obtained electronic contrast is hence too big to be ascribed to charge transfer effects alone, and a Sr-doping modulation must be taken into account. Accounting for the uncertainty of the XRR fit, which reflects on the error of Δb_{fit}, we cannot exclude the presence of additional charge transfer effects between the layers.

4.1.3 SQUID magnetometry

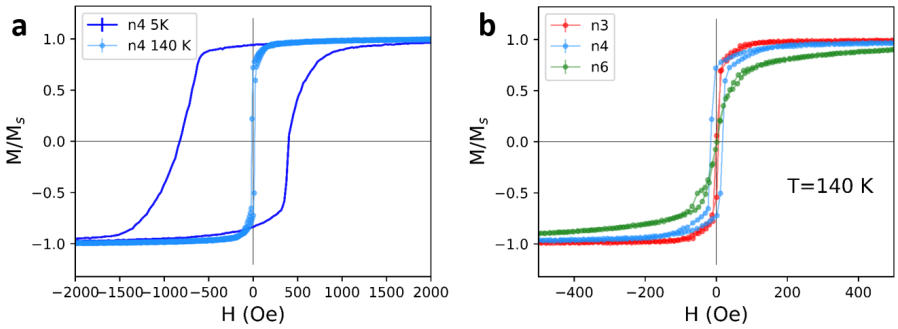

Figure 4.3: Hysteresis loops measured via SQUID magnetometry. **a**. Hysteresis loops for sample $N4$ at 5K and 140 K; **b**. Comparison of hysteresis loops of different samples at 140 K.

The magnetic properties of the SLs were studied by SQUID-VSM magnetometry in VSM mode at the MPI-FKF with a MPMS3 magnetometer from Quantum Design. The magnetization of samples was measured between 5 and 295 K with

field applied in plane and along the sample edge direction, equivalent to the crystallographic (100) axis of LSMO.

The samples showed the typical hysteresis loops of ferromagnetic LSMO, with coercivity decreasing upon increasing temperature (Figure 4.3a). Typical S-shaped loops are observed for all samples at temperature between 100 and 300 K (Figure 4.3b). The saturation moments decreased when the sample was warmed, as expected from a ferromagnet approaching Curie temperature. Saturation of moments is reached for all samples above 1 kOe.

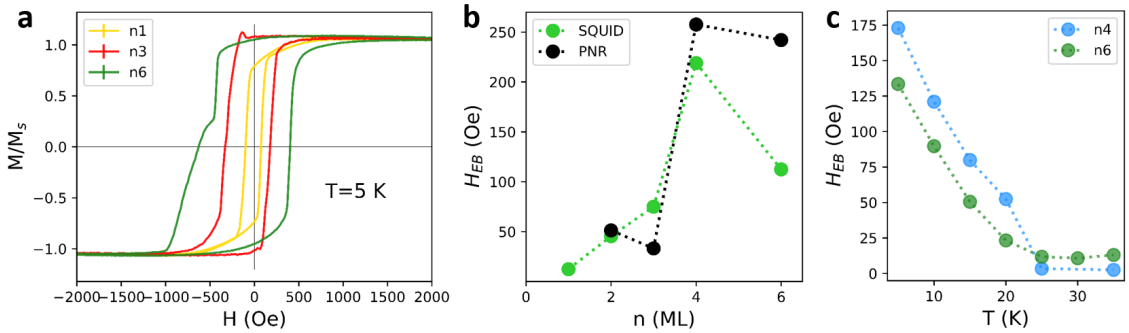

Figure 4.4: Low temperature magnetic properties measured via SQUID magnetometry. **a**. Hysteresis loops at 5K for samples $N1$, $N3$ and $N6$; **b**. Exchange bias field obtained from SQUID and PNR measurement versus spacer thickness; **c**. Temperature dependence of the exchange bias field for samples $N4$ and $N6$.

In addition, we observed a negative exchange bias (EB) in all samples with n >3 below 25 K (Figure 4.4a), which was also confirmed with additional PNR experiments (Figure 4.4b). The exchange bias field H_{EB} is defined as shown in Equation 4.4, where H_{c1} and H_{c1} are the positive and negative coercivities of the hysteresis loop. The dependence of exchange bias versus spacer thickness and versus temperature is shown in Figure 4.4b and c, respectively.

$$H_{EB} = \frac{H_{c1} - H_{c2}}{2} \tag{4.4}$$

The presence of exchange bias is a signature of the presence of AF ordering in the overdoped layer.

Another feature found for $N6$ at 5 K is a kink in the hysteresis loop in the upper

branch (green line in Figure 4.4a), or decreasing H. Such a kink can be explained as the consecutive switching of different parts of the sample upon magnetic reversal. For example, if we assume that the SL is divided in two regions each identified by a different H_{EB}, only the part with smaller EB will have switched at the intermediate field H_{kink}=-500 Oe, while the rest is still in the positive saturation direction. This can be simulated by a simple superposition of two hysteresis loops each with coercivity H_c and slope ht. The ratio between the saturation moment M_s of each loop will give us information about the volume of each magnetic region. The

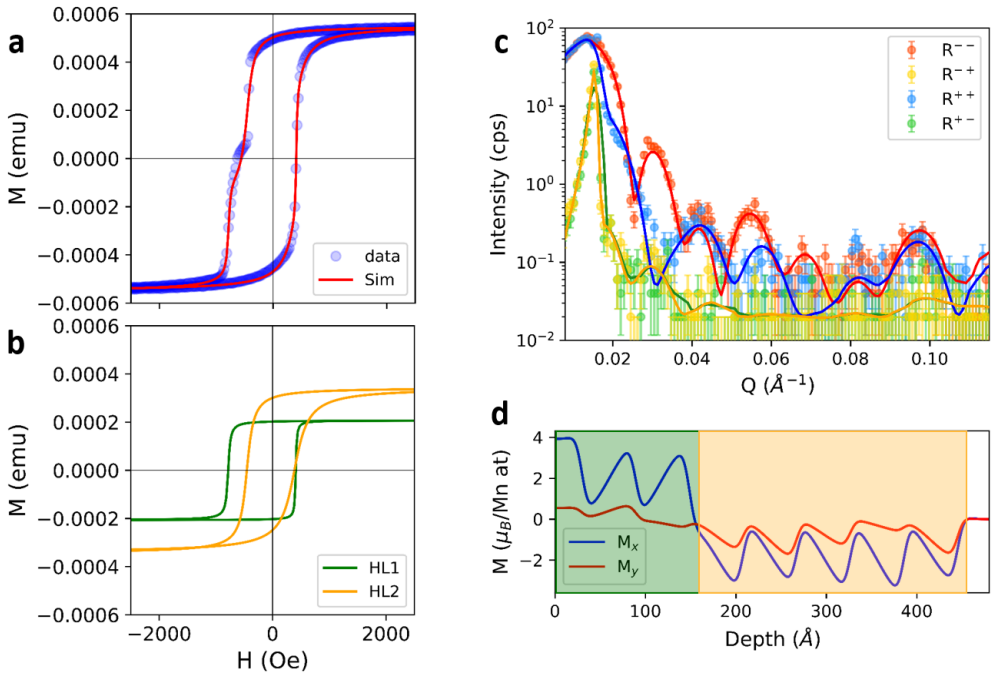

Figure 4.5: Characterization of hysteresis kink of sample $N6$ at T=5K. **a**. Measured and simulated hysteresis loop; **b**. Deconvolution of the two magnetic components from the simulation shown in Panel a; **c**. PNR measurement and fit at 5K and H=-500 Oe measured at Super ADAM; **d** Magnetic depth profile over the entire SL depth at 5 K and -500 Oe, showing in blue the component of magnetization M_x parallel to the applied field H, and in red the component M_y perpendicular to H. The magnetic reversal first occurs only in the upper 5 FM layers (yellow area), while the 3 bottom layers (green area) are still antiparallel to H.

hysteresis loop was approximated with a simple arctangent function (Ref. [167])

defined as follows:

$$M(H) = \frac{2}{\pi} M_s \arctan\left(\frac{H - H_c}{ht}\right). \tag{4.5}$$

Due to the presence of exchange bias, the upper (UB) and lower (LB) branches were simulated separately, in order to allow for different positive (H_p) and negative (H_n) coercivities, with the following expressions:

$$M_{UB}(H) = \frac{2}{\pi} M_{s1} \arctan\left(\frac{H - H_{p1}}{ht1}\right) + \frac{2}{\pi} M_{s2} \arctan\left(\frac{H - H_{p2}}{ht2}\right) \tag{4.6}$$

$$M_{LB}(H) = \frac{2}{\pi} M_{s1} \arctan\left(\frac{H - H_{n1}}{ht1}\right) + \frac{2}{\pi} M_{s2} \arctan\left(\frac{H - H_{n2}}{ht2}\right). \tag{4.7}$$

A fit using as free parameters the saturation moments, coercivities and slopes was made based on the experimental hysteresis loop measured by SQUID. The result is shown in Figure 4.5a, and the two hysteresis loops 1 and 2 obtained are shown in Figure 4.5b. As one can see from this plot, the kink can be explained as the superposition of the two loops with different EB. The saturation moment of each of these loops indicates that the sample is split in two parts accounting for 37% (green) and 63% (yellow) of the total magnetization, or 3 and 5 FM layers out of the total 8 respectively. In order to gain further insight into this partial switching mechanism, a full PNR was measured at T=5K and H=-500 Oe, where the kink in the hysteresis loop was observed. The data (dots) and fit (solid lines) of all four polarization channels are shown in Figure 4.5c. The retrieved magnetic depth profile in Figure 4.5d shows that 5 FM layers have already switched (yellow area), while the 3 remaining one are still aligned in the positive field direction (green area). Interestingly, PNR suggests that the part with bigger exchanged bias, which is non reversed yet, is the one closer to the substrate, where the crystalline quality is supposed to be higher. This suggests a better magnetic contact between FM and AF interfaces, with the consequence of an increased EB for the layers grown first.

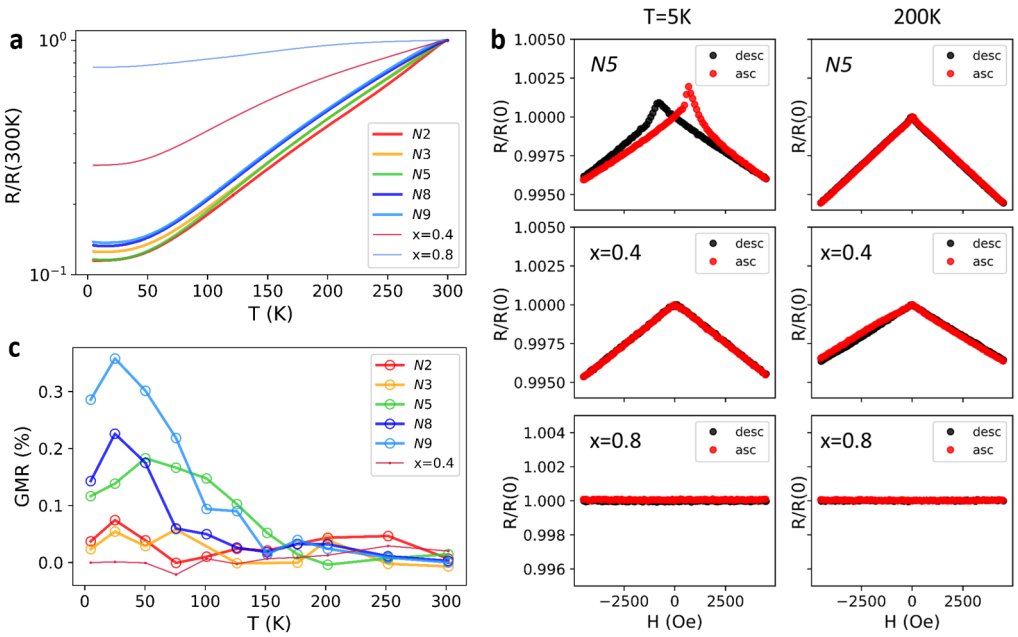

Figure 4.6: Summary of transport measurements. **a**. Normalized resistance at H=4.5kOe versus temperature for the SLs and single layers of doping x=0.4 and x=0.8; **b**. Normalized magnetoresistance measurements for sample $N5$ (first row), x=0.4 (second row) and x=0.8 (third row) at T=5 K (left column) and T=200 K (right column). The descending (ascending) branches are indicated with black (red) symbols; **c** Comparison of GMR effects for different sample versus temperature. Only values relative to the descending branch are reported for simplicity.

4.1.4 Electrical transport

The electrical transport of the SLs was studied at temperatures between 5 and 300 K. In order to compare with the constituent materials, LSMO(x=0.4) and LSMO (x=0.8), two additional single layer thin films of thickness 50 nm were grown by MBE in the same conditions as the SLs. Figure 4.6a shows the resistance versus temperature curves for selected SLs and for the single layers. The curves were measured in a saturating field of 4.5 kOe, and normalized to the RT resistance. The x=0.4 sample showed the expected metallic behaviour. The metallicity and ferromagnetism in LSMO with x<0.5 are known to be intimately connected due to the half filling of the t_{2g} band, where Hund's rule impedes the hopping if the spins are not parallel. Interestingly though, for the SLs we observe an even increased

metallicity. In particular, the R(T) dependence of all SLs and of the x=0.4 sample follows a linear decrease and a plateau below 50 K, which can be fitted with a power law of $T^{2.5}$. The good agreement of such fit confirms a scattering through electron-magnon ($R(T) \propto T^{4.5}$) and electron-electron ($R(T) \propto T^2$) interactions, as previously shown by [168]. In contrast, for sample x=0.8 the resistance does not vary with the power law of $T^{2.5}$, hence a different scattering mechanism is expected with respect to FM LSMO.

In addition to these transport measurements, the magnetoresistance (MR) of samples was studied. The field was swept from positive to negative field H (descending branch) and back (ascending). Figure 4.6b shows an extract of the most meaningful results: the overdoped x=0.8 sample shows no signs of MR, consistently to the expected AF phase for this doping (bottom row). The FM single layer x=0.4 shows the well known colossal magnetoresistance (CMR) effect [169], which results in the linear dependence of resistance and applied field, shown in the middle row. We did not observe any significant increase of CMR while heating up the sample, indicating that the Curie temperature of the sample was well above RT. For the SLs (in the top row the example of sample $N5$) in addition to the CMR effect, we observe at low temperatures the emergence of peaks around coercive field. These peaks are associated with an increased scattering of conduction electrons due to non-collinear or AP alignment of spins of adjacent magnetic layers. This effect is commonly addressed as giant magnetoresistance, or GMR, and is defined as shown in Eq.4.8, following the work of Granada et al. [170].

$$\mathrm{GMR}(\%) = 100 * \frac{R_{max} - R'}{R'} \tag{4.8}$$

The definition of R_{max} and R' is shown in Figure 4.7, where the MR of sample $N5$ at 50 K is shown. For each MR branch, R_{max} is defined as the maximum value measured, while R' (shown as black empty dot) is defined as $R'=\mathrm{m}H_{max}+\mathrm{b}$, with H_{max} the field corresponding to R_{max} and the slope m and intercept b of the linear regression of the beginning of the MR, where only CMR effects are present, as shown in dashed lines.

The comparison of GMR effects for all samples at different temperatures is represented in Figure 4.6c. While the single FM layer x=0.4 does not show any GMR,

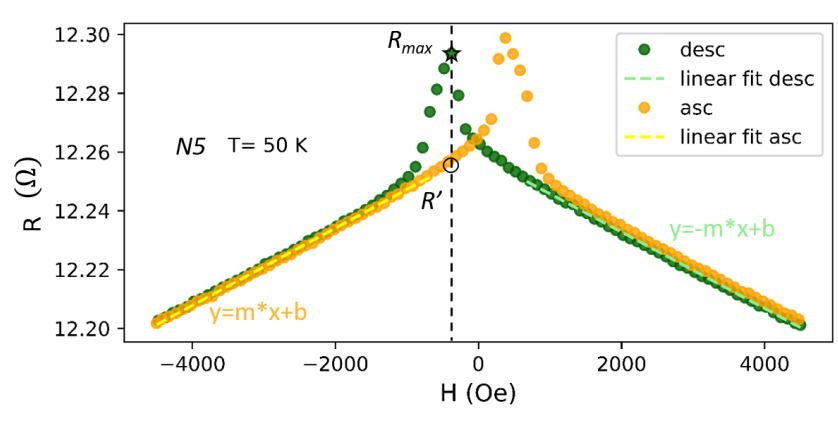

Figure 4.7: Definition of GMR for sample $N5$ at T=50 K.

this effect increases with increasing spacer thickness. This is a hint of increasing antiferromagnetic correlations in the spacer, that act as scattering centers for conduction electrons during the magnetization reversal process. The fading of GMR above 150 K indicates the weakening or disappearance of such AF correlations.

4.1.5 Polarized neutron reflectometry

We carried out PNR at different temperatures and magnetic fields to reconstruct the depth-dependent magnetic phase diagram of all the SLs.

Figure 4.8a shows a representative reflectivity curve of the sample $N5$ at the lowest temperature and saturated state (3 K and 4.5 kOe). The strong superlattice Bragg peak $(001)_{SL}$ is a common feature among all samples (also shown in Figure 4.9a) and, as for XRR, results from the SL periodicity. In PNR however, its intensity arises mainly from the strong magnetic contrast rather than from nuclear contrast, which in this case is marginal (nominally less than 3% of the average scattering potential).

We retrieved the depth-dependent magnetic profile by fitting a ten times (eight times for $N6$) repeated bilayer model to the PNR curve. The magnetic moment of the AF layer was kept fixed at 0 μ_B/Mn atom, while the roughness σ of both interfaces was used as a smearing parameter for the magnetic profile. A summary of the most important fit parameters is shown in Table 4.1.

Figure 4.8b shows the variation of the magnetic moment along 2 s.c.u. for

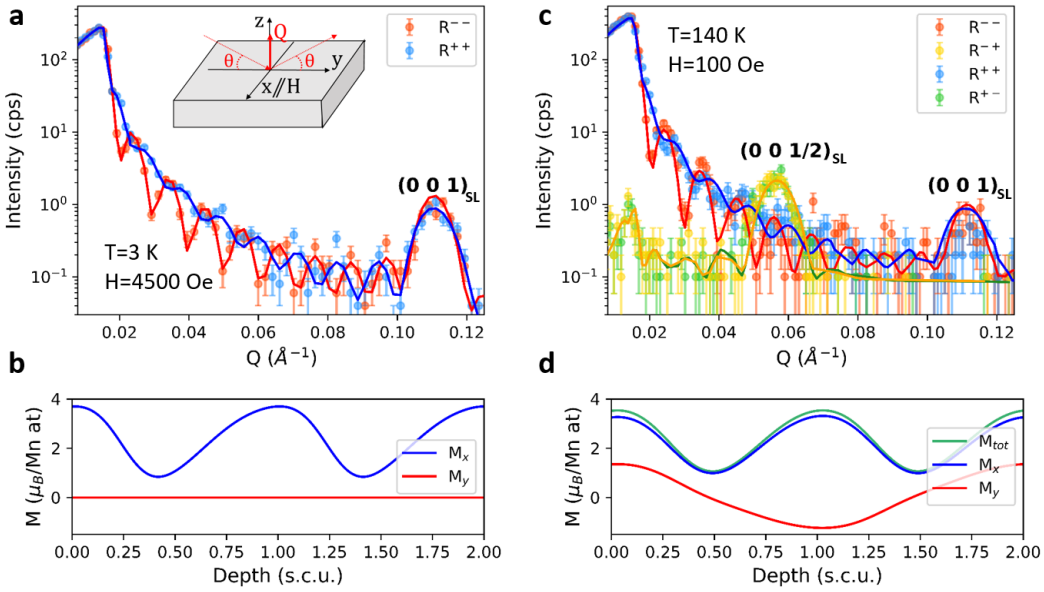

Figure 4.8: Selected PNR curves for sample $N5$. **a**. PNR measured on the $N5$ sample at 3 K and saturation field of 4.5 kOe and fit curves (solid lines). The SF channels, showing background signal only, are omitted. On the inset a sketch of the coordinates of experiment is shown; **b**. Magnetic depth profile over 2 s.c.u. at 3K and 4.5 kOe, showing in blue the component of magnetization M_x pointing along the applied field H, and in red the component M_y perpendicular to the applied field H; **c** PNR measured on the $N5$ sample at 140 K and applied field of 100 Oe and fit curves (solid lines), **d** Magnetic depth profile over 2 s.c.u. at 140 K and 100 Oe, showing in green the total magnetization profile, in blue M_x, and in red M_y.

sample $N5$. This result confirms that the magnetization is modulated along the z direction in lockstep with the concentration of Sr. The magnetic depth profile is asymmetric at the upper and lower interface, similar to previous observations [171]. Remarkably, the magnetization does not reach zero at any depth, although no net magnetization is expected at x=0.8, which is nominally C-type AF in bulk samples.

Given the result from low temperature measurements, we investigated the magnetic phase diagram at the intermediate magnetic fields and temperatures. PNR unveiled a doubling of the magnetic structure present in sample $N5$ at 140 K manifested by the SF peak at the half of the reciprocal superstructural periodicity (labelled $(0\ 0\ \frac{1}{2})_{SL}$), as shown in Figure 4.8c. Such a strong feature appearing

Table 4.1: Summary of parameters obtained from fitting of experimental data at 3K and 4.5 kOe.

ID	d_{FM} (Å)	d_{AF} (Å)	σ_{FM} (Å)	σ_{AF} (Å)	M_{FM} (μ_B/Mn at.)
$N2$	31.8 ± 0.3	10.3 ± 0.3	7 ± 1	12 ± 2	3.87 ± 0.3
$N3$	30.8 ± 0.3	14.9 ± 0.3	5 ± 2	13 ± 3	3.87 ± 0.3
$N4$	36.3 ± 0.3	15.7 ± 0.3	5 ± 2	12 ± 2	3.87 ± 0.3
$N5$	36.5 ± 0.2	20.3 ± 0.2	5 ± 2	11 ± 1.5	3.87 ± 0.2
$N6$	30.2 ± 0.7	28.9 ± 0.5	5 ± 1.5	13 ± 3	3.87 ± 0.2
$N8$*	40.5 ± 0.5	27.5 ± 0.5	3 ± 5	11 ± 3	3.08 ± 0.2
$N9$	40.2 ± 0.2	30.0 ± 0.2	3 ± 3	15 ± 1	3.20 ± 0.2

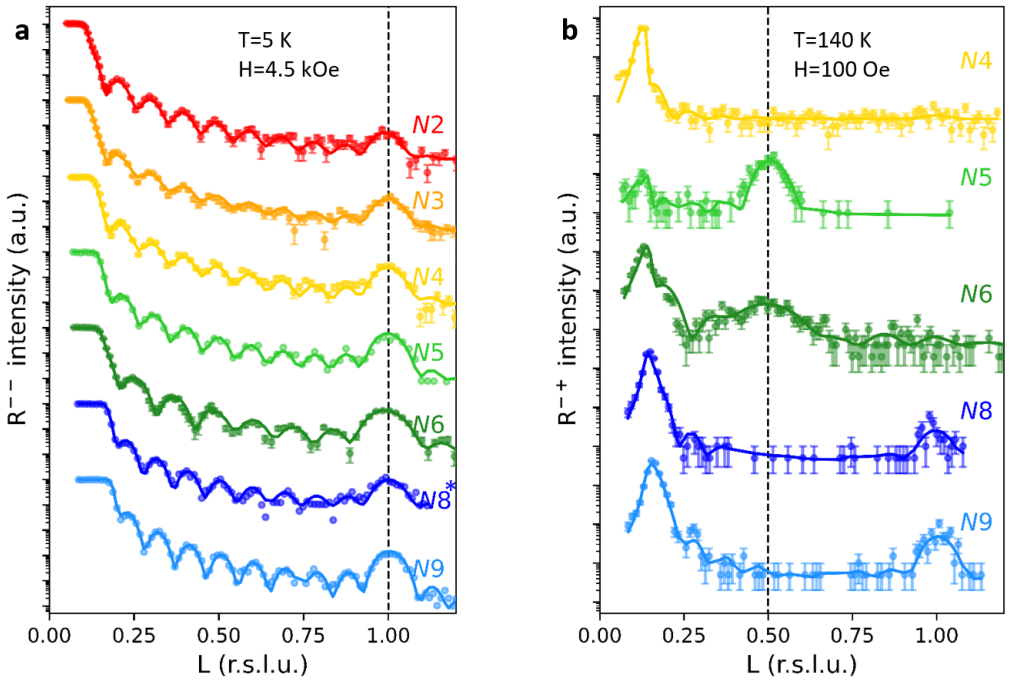

Figure 4.9: Comparison of neutron reflectivity for different samples. Q values are here normalized in reciprocal superlattice units. The solid lines are fit curves with a simple model of FM-AF stacking. **a**. NSF channel measured on different samples at 5 K and applied field of 4.5 kOe ($N8$* measured at 140 K and 200 Oe), showing the emergence of the $(0\ 0\ 1)_{SL}$ peak; **b**. SF channel measured on different samples at 140 K and applied field of 100 Oe, showing the emergence of the $(0\ 0\ \frac{1}{2})_{SL}$ peak for $N5$ and $N6$.

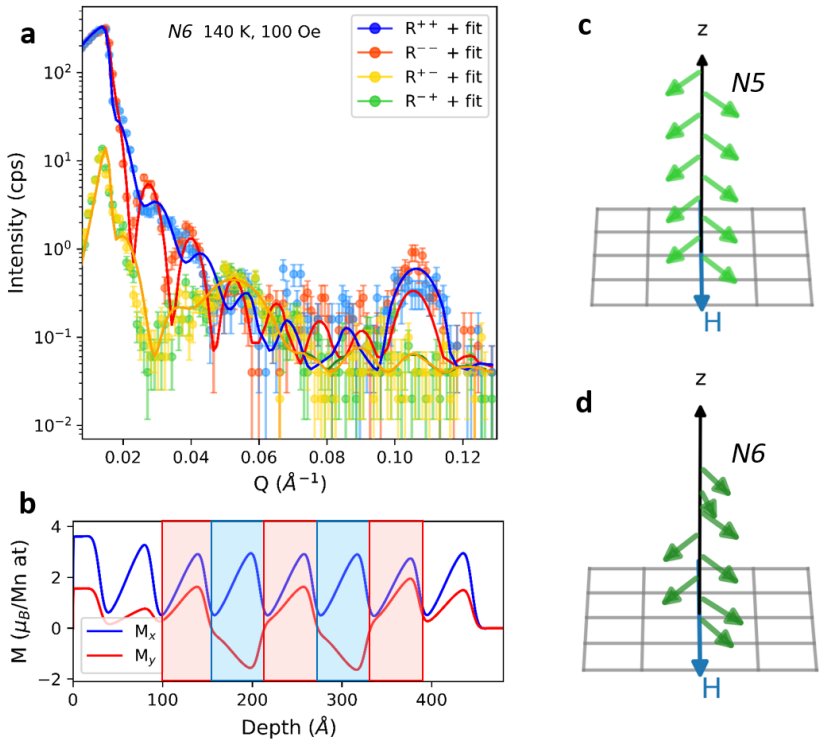

Figure 4.10: Characterization of $(0\ 0\ \frac{1}{2})_{SL}$ peak in sample $N6$ at T=140K H=100 Oe. **a**. PNR measurement and fit ; **b**. Magnetic depth profile over the entire SL depth, showing in blue M_x, and in red M_y. The doubling of magnetic structure is observed only in 5 (out of total 8) repetitions (red and blue boxes), indicating short range ordering; sketch of the orientation of magnetic moments in FM layers in sample $N5$ (**c**) and $N6$ (**d**).

exclusively in the SF channels points to the formation of a long-range magnetic order, where the magnetic moment at the optimally doped FM layer is canted by an angle $\pm\alpha/2$ with respect to the applied magnetic field.

PNR analysis was performed with fixed thickness, roughness and magnetization amplitude taken from low temperature measurement. The only free parameters in the fit were the directions of magnetic moment in FM layers. This allowed to retrieve the opening angle $\alpha = \alpha_1 - \alpha_2$. The best fit is shown in Figure 4.8c as solid lines, and the corresponding magnetic SLD profile in Figure 4.8d. The SLD profile clearly shows that the periodicity of M_y is 2 s.c.u., hence twice the periodicity of

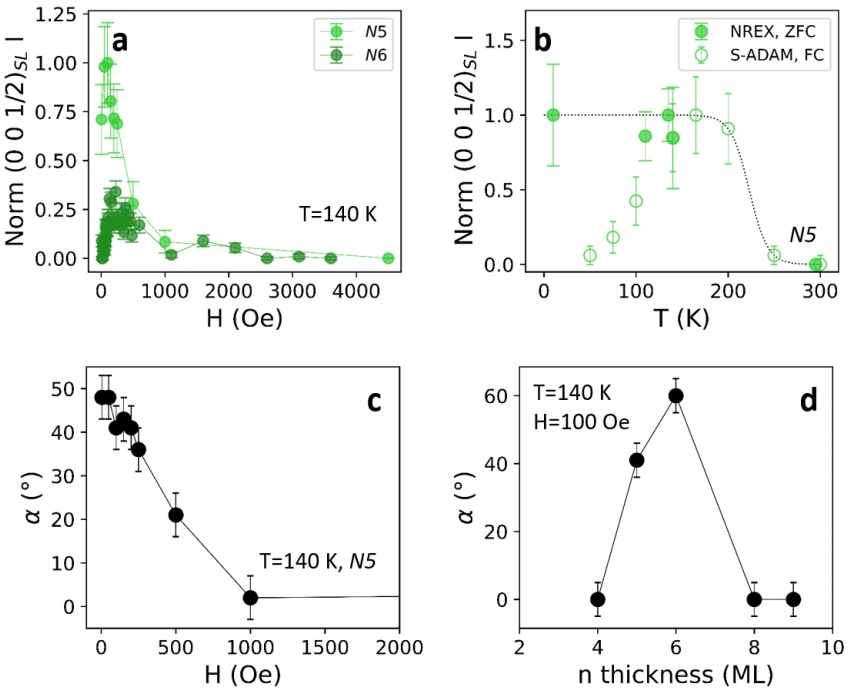

Figure 4.11: Characterization of doubling of magnetic structure by PNR. **a**. Field dependence of the $(0\ 0\ \frac{1}{2})_{SL}$ peak of sample $N5$ and $N6$; **b**. Field dependence of α for $N5$; **c**. Temperature dependence of the intensity of the $(0\ 0\ \frac{1}{2})_{SL}$ peak of $N5$, **d** α versus overdoped layer thickness at 140 K and 100 Oe. The light lines in **a-d** are a guide to the eye.

M_x.

In Figure 4.9b, we compare SF channels between different samples at the same field and temperature. We could observe the signature $(0\ 0\ \frac{1}{2})_{SL}$ peaks in samples $N5$ and $N6$, but not in the other samples. This is in stark contrast to the results from SQUID magnetometry, where all samples showed a very similar behaviour of extremely soft ferromagnetism at intermediate temperatures, as shown in 4.3b. A small parenthesis should be opened here about the intense feature at low Q (around 0.2 s.c.u.). This is the resonance peak arising from the strong contrast between the substrate LSAT and the heterostructure on top of it. It can be shown that for Q→0 the SF intensity is a measure of the integral non-collinear moments of the system [172–174]. Therefore it is clear why for sample $N5$, in which the doubling of the magnetic structure gives indeed a zero integrated non-collinear

magnetization, this feature is the smallest. In the other samples, on the other hand, we observe a strong signal, which suggests either the formation of magnetic domains, or that all the FM layers point to the same direction, which may reflect the easy axis of the system.

We found substantial differences in the $(0\ 0\ \frac{1}{2})_{SL}$ peak width of samples $N5$ and $N6$. For $N5$ the peak width is the same as for the other superstructure peaks, implying a complete correlation between all FM layers and hence a long-range order. On the other hand for $N6$ the peak is clearly broader, indicating that the correlation between FM layers is degraded. PNR simulations, shown in 4.10, suggest that only a part of the sample (5 out of 8 FM layers) is in the fan-like configuration, meaning a short-range order with correlation length shorter than the total depth of the SL. The presence of uncorrelated FM layers is also consistent with the small steps observed in the hysteresis loop of $N6$ at 140 K (green points in 4.3b). Tracking the behaviour of the $(0\ 0\ \frac{1}{2})_{SL}$ peaks intensity against the external applied field, we observe that the fan-like non-collinear order is stable up to H=1 kOe (Figure 4.11**b**). Figure 4.11**b** indicates that the non-collinar superstructure emerges below 200 K. The opening of the angle α after field cooling with H=4.5 kOe is observed only above 100 K (empty circles) when the magnetic loops show soft-magnetism and small coercivity (4.3b), while at low temperature the hardening of magnetic properties of the FM layers (4.3a) prevents it. Remarkably, we also observe the spontaneous formation of the fan-like structure when cooling down in zero field (full circles). The field dependence of the opening angle α was obtained by fitting the full-polarization curves. The result is shown in Figure 4.11**c**. The value of α peaks at $H = 0$ Oe and decreases continuously until it reaches zero at $H \lesssim 1$ kOe, where all FM layers are field-aligned. Finally Figure 4.11e shows the opening angle α at fixed field versus the overdoped layer thickness.

4.1.6 Discussion

First of all we want to examine the magnetic nature of overdoped layers stacked between optimally doped FM layers, and their possible interaction. The fitting of XRR profiles (Figure 4.12a) showed that the Sr-doping level at the center of

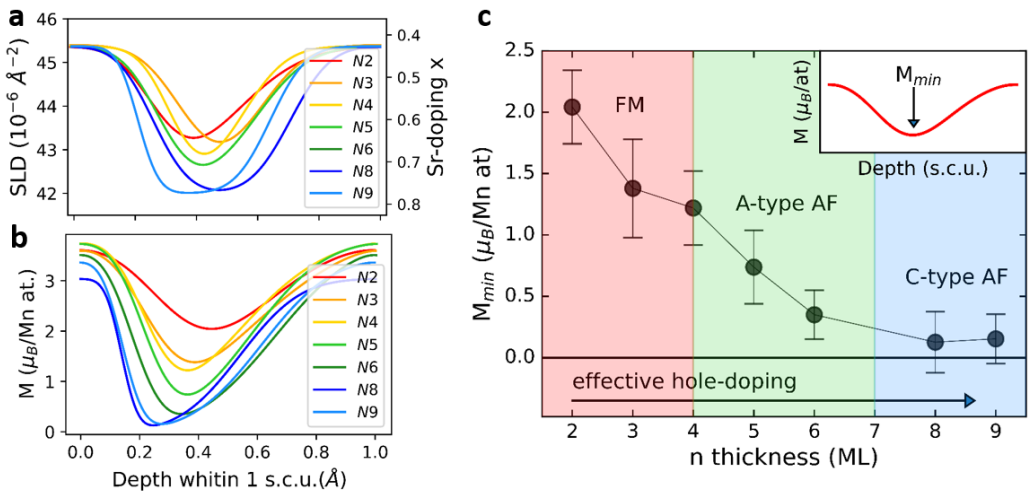

Figure 4.12: Magnetic nature of the overdoped layer. **a** Depth-dependent SLD profile and Sr-doping over 1 s.c.u. determined from XRR fitting for different samples at RT; **b** Magnetic SLD profiles extracted from PNR measurements at 5K and 4.5 kOe on different samples. (*sample $N8$ fit at 140K, 100 Oe); **c** Magnetization in the center of the overdoped layer, retrieved from PNR data fitting shown in Panel a, versus spacer thickness. Inset: Definition of M_{min} from magnetic depth profile.

overdoped layer varies for all samples between 0.6<x<0.8, and according to the phase diagram of bulk LSMO (Figure 4.1a), the A- and C-type AF order corresponding to these doping level does not exhibit a net magnetization. However, the magnetic depth profiles obtained from PNR of different samples (Figure 4.12b) shows that the magnetization approaches 0 only for the thickest overdoped layers $N8$, $N9$, while it still has a finite value for the remaining samples. The presence of a net moment in the overdoped layer can be attributed to an additional charge transfer which redistributes holes from the overdoped to the optimally doped regions, as previously reported [175–177]. This mechanism diminishes the effective hole-doping of the layer and allows to tune its magnetism following the phase diagram, ranging from a FM order with reduced moment in the samples with the thinnest overdoped layers ($n \leq 4$, red region Figure 4.12c), to a A-type AF for the intermediate samples $N5$ and $N6$ (green region), and finally approaching the nominal doping of x=0.8 with a C-type AF in the thickest samples $n \geq 8$ (blue

region). The absence of AF order for n <4 is also consistent with the absence of exchange bias at low temperatures for these samples, shown in (Figure 4.4b).

In particular we can explain the observed magnetic profiles of samples $N5$ and $N6$ if we assume a canting of moments in the A-type layer, as previously observed for doping around x=0.5 in thin films [178, 179] and in bulk [166] manganites. This canted AF phase results in the canting angle γ, defined as the angle between the moments of two adjacent MLs. The angle γ is the consequence of competing double-exchange and superexchange interactions and was shown to depend on the Sr-doping in thin films [179]: for 0.4<x<0.6 γ varies between 0 (FM order) and 180° (AF order). The proposed scenario is represented in Figure 4.13a,b in the commensurately aligned states and the doubled magnetic structure, respectively. As shown here, the magnetic $M_{x,y}$ profiles are reproduced if we consider moments in the AF layer which are (i) modulated in magnitude and (ii) canted by an angle that increases with the increasing hole-doping in the range $0 < \gamma <180°$, with the antiferromagnetic order direction perpendicular to the applied field, consistently with [179]. Another possible scenario is that represented in the4.13c,d, in which all moments have the same magnitude, both in the AF and FM layers, and only canting is considered. Except for the canting angle of AF layer γ, which in the second case is significantly larger, both models are equally describing our magnetic profiles $M_{x,y}$. However, the model in Figure 4.13a,b with modulated magnitude of moments gives the better physical picture, as it agrees with the observed reduction of moment in overdoped layers (Figure 4.12). We want to emphasize that even though the suggested canted A-type AF is a highly non-collinear phase, the PNR depth resolution averages the magnetization over $\approx$ 2 MLs. Hence, the the magnetic moments of individual atomic layers are not resolved.

In order to verify the canted AF nature of the overdoped layer, we grew a single layer LSMO of Sr-doping x=0.5 and thickness 50 nm by MBE on LSAT substrate. The single layer was characterized by PNR, to confirm the presence of a net moment, and by polarized neutron diffraction (PND), which allows to resolve the atomic AF order. The doping x=0.5 was chosen to mimic the effective hole-doping expected in the overdoped layer of the SLs $N5$ and $N6$. An antiferromagnetic peak at (0 0 $\frac{1}{2}$) (r.l.u) was observed by PND for this sample in SF channels at 100 K and field of 5 kOe (Figure 4.14a). The presence of the peak

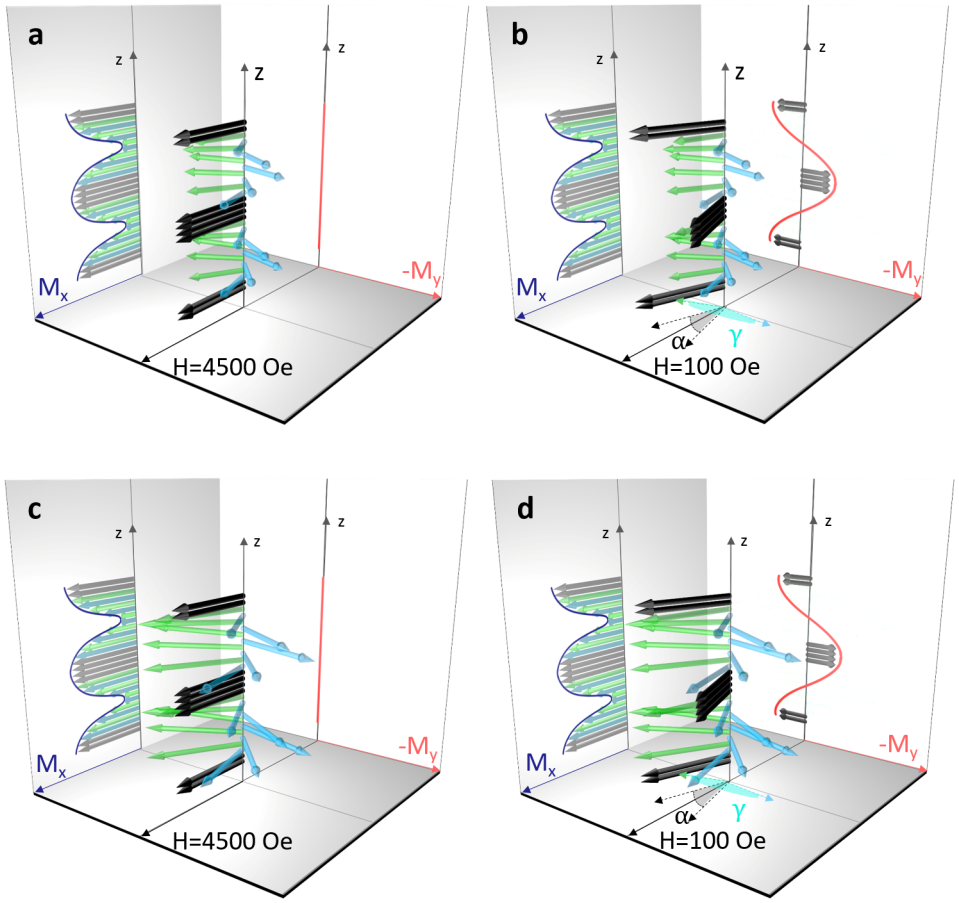

Figure 4.13: Visualization of the non-collinear magnetic structure in sample $N5$. Each arrow represents the average magnetic moment direction in one ML. The projections on the left (right) wall represent the magnetic SLD profile parallel to the applied field M_x (perpendicular to the applied field M_y) as blue (red) lines. **a**. Model of magnetic configuration at 3 K and 4.5 kOe with modulation of the moment amplitude. **b**. Model of magnetic configuration at 140 K and 100 Oe, showing the doubling of the magnetic structure along y direction (red line). The definition of the opening angle α and canting angle γ are shown as a projection on the bottom plane; **c** Model of magnetic configuration at 3 K and 4.5 kOe with fixed moment amplitude. **d**. Model of magnetic configuration at 140 K and 100 Oe, with fixed moment amplitude.

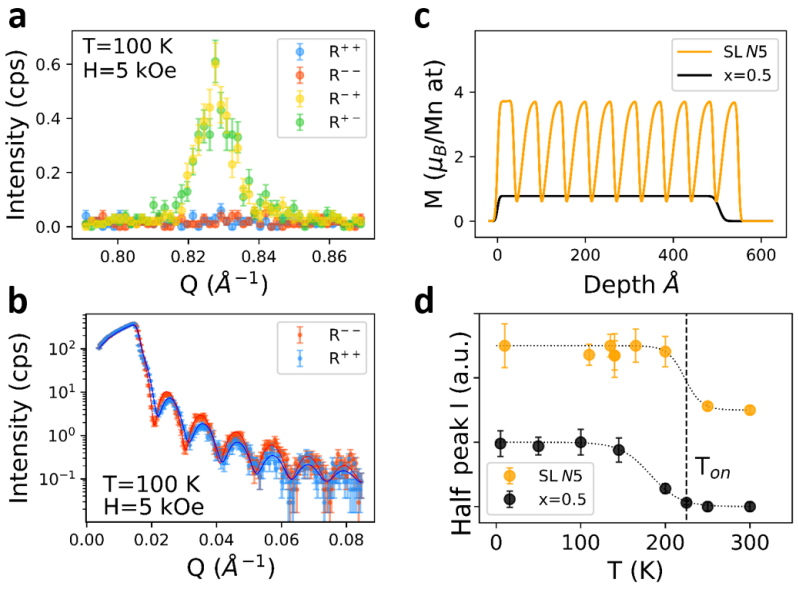

Figure 4.14: Summary of measurements on the overdoped LSMO (x=0.5) single layer. **a**. AF peak measured at SuperADAM for the single layer sample x=0.5 at 100 K and 5kOe, showing only SF intensity. **b**. PNR for the single layer sample x=0.5 at 100 K and 5000 Oe and fit curves. **c**. Comparison of magnetic depth profiles at saturation field of the SL $N5$ at 140 K and the single layer x=0.5 at 100 K. **d**. Comparison of the temperature dependence of the superstructural AF peak in $N5$ and of the single layer atomic AF peak in x=0.5. The dotted lines are a guide to the eye, the dashed line indicates the onset temperature T_{on}.

only in the SF channels is reminiscent of the superstructural one observed in our SLs, and once again signifies the perpendicular orientation of spins with respect to the applied field. From this measurement we evince that an applied field of 5 kOe is not sufficient to suppress the AF order by ferromagnetic alignment of the spins, confirming previous reports [179] where the canted AF phase was shown to persist at least up to 8.2 kOe. Therefore, for our magnetic model of the SLs, we considered fixed moments in the canted A-type AF layer at all applied fields $H < 5$ kOe. The difference between the observed profiles obtained at different fields comes from the soft FM layers: above 1 kOe aligned to external field (Figure 4.13a), and below 1 kOe coupled and pointing to $\pm\alpha$ (Figure 4.13b).

We confirmed the canting of spins of the AF with PNR measurement of the

single layer x=0.5, which shows clear spin asymmetry of R^{--} and R^{++} channels and hence the presence of a net moment (Figure 4.14b). Model simulations on this PNR curve allowed to retrieve a moment of 0.8 μ_B/Mn atom. If we compare the magnetic SLD profile obtained for the SL $N5$ and for the single layer x=0.5 we can observe that the moment coming from the canted AF layer coincides with the one present at the overdoped layer depth in the SL $N5$, as shown in Figure 4.14c, suggesting the presence of A-type antiferromagnetic correlations in intermediate thickness SLs. Another strong hint on the crucial role played by the canted AF layer is given by the comparison of temperature ranges in which the superstructural order and the antiferromagnetism are present: we have found a $T_{Neel} \approx 225$ K in the x=0.5 single layer, which corresponds to the onset temperature T_{on} of the doubling of magnetic structure in $N5$ (Figure 4.14d).

Now we discuss the origin of the doubled magnetic structure. Given the complexity of this magnetic configuration, a quantitative assertion of the energies at stake goes beyond the scope of this study, however we can describe the observed behaviour in a qualitative way. We propose that the observed opening angle α is the result of two competing interactions: interfacial exchange interactions and Zeeman interaction. The interfacial exchange interactions alone can naturally explain the period-two superstructure observed at low field (Figure 4.14b), with the FM moments following the canting of the neighbouring spins. In the presence of a magnetic field, the additional Zeeman interaction leads to the gradual alignment of the spins towards the field direction. This competition can be used to tune the degree of non-collinearity of our fan-like structure, in contrast to the canted modulated spin structure found by Santos et al. [179] which was shown to be stable up to 8.2 kOe. A similar tunable non-collinearity was reported for nickelate/manganite heterojunctions by Hoffman et al. [11], where the helical order in the nickelate spacers lead to a similar doubling of the magnetic structure of manganite layers. Remarkably, such complex long-range order could be achieved in our case in a homojunction with such a slight variation of doping.

By combining our knowledge of the effective doping of the overdoped layer and of the exchange interaction at the interface with the optimally doped layer, we can now address the thickness-dependence of the overall magnetic state. For $n \leq 4$, the spacer thickness is lower than the charge smearing length, and hence the whole

SL behaves like a FM with slightly modulated magnetic moments. For $4 \leq n \leq 7$, the overdoped layer is a canted A-type AF, due to the lower effective doping level caused by the charge transfer. A strong exchange coupling links the canted moments in the AF with the moments of the FM layer. The short-range intra-layer coupling and long-range AF interactions result in the complex non-collinear orientation of spins for sample $N5$ and $N6$. Finally, when $n \geq 8$, the overdoped layer is still AF, with the innermost part characterized by a Sr-doping closer to the nominal x=0.8. This phase corresponds to C-type AF (AF ordering in the plane) that, in contrast to A-type AF (FM ordering in the plane), does not allow exchange coupling with the neighbouring FM layer. The presence of this phase thus effectively decouples subsequent FM layers.

4.1.7 Device operation

The fan-like structure found is an interesting building block for spintronic devices, where the complex non collinear magnetism gives different resistive states controlled by the opening angle α. An interesting effect was found for sample $N5$ at T=100 K. Figure 4.15a shows the MR measured while decreasing the field to 0 (black symbols) and increasing it back (red). A hysteresis opens at around 500 Oe, indicating a higher resistance state with decreasing H and a low resistance state with increasing H. This measurement indicates a "breathing-effect" of the magnetic fan structure with lower (higher) opening angle when the field is decreased (increased).

In order to prove this mechanism, PNR measurements at the maximum of the $(0\ 0\ \frac{1}{2})_{SL}$ peak at the same temperature and range of fields were performed. The SF intensity, which is direct indication of the opening angle α, was tracked while sweeping the field from +4.5 kOe to 0 and back. As it is shown in Figure 4.15b, the behaviour of SF reproduces the MR measurement, indicating an effective role of the lon range non-collinear structure in the hysteresis observed.

This effect could be used in a memory device, in which by looping the field up and down (but without needing reversal) the high and low resistance states are achieved. Figure 4.15c shows the reproducibility and stability of the effect over several loops, represented as the measured resistance at fixed field H=220 Oe

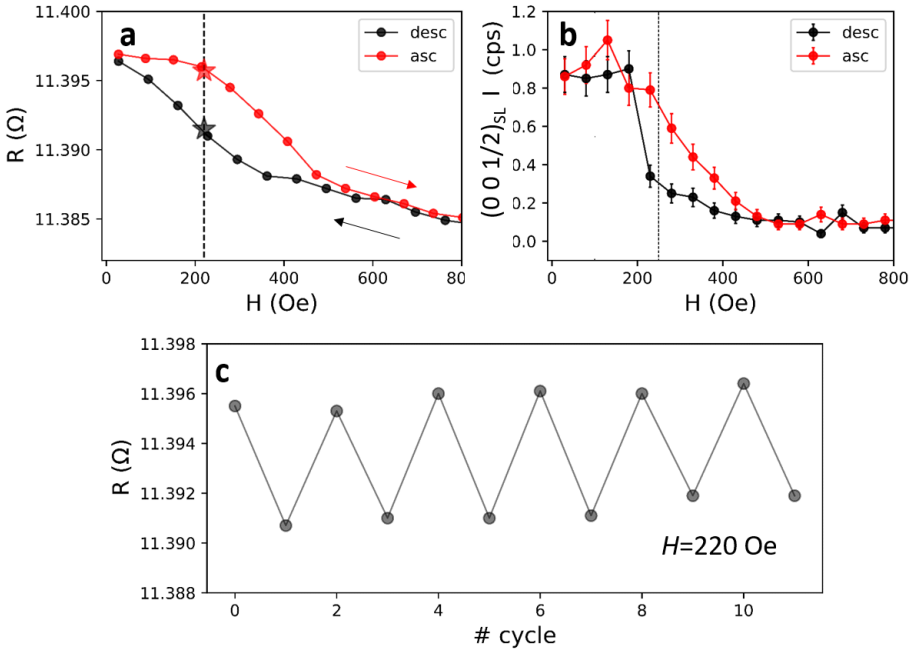

Figure 4.15: Device operation of sample $N5$ at 100 K. **a**. Resistivity loop showing hysteresis without magnetic reversal; **b**. PNR measurement of SF intensity at Q corresponding to the maximum of $(0\ 0\ \frac{1}{2})_{SL}$ with field sweeping; **c** Cycling over the two distinct magnetic states shown by stars in Panel a.

during the cycling procedure. Even though the difference in resistances is very small, it is indeed measurable, and could be enhanced significantly with the use of an out-of-plane current instead of an in-plane one as used in this example.

4.1.8 Conclusions

In summary, we have synthesized and characterized a series of all-manganite superlattices, stacking a fixed thickness of FM LSMO and a varying layer thickness of overdoped LSMO. By doing so we were able to tune the charge diffusion and hence the magnetism in the spacer layer, which in turn modified the magnetic properties of the whole superstructure. We have shown that is was possible to engineer a doubled non-collinear magnetic structure, which was found for spacer thickness of 5 and 6 MLs between 10 and 225 K and below 1 kOe.

At this temperature it is possible to tune the non-collinearity of the system through the opening angle α by application of relatively small fields ($H \lesssim 1$ kOe). This tunable noncollinear magnetism, or in other words this canted synthetic antiferromagnet, could be an interesting component for spintronics devices, where the non-collinearity of the system is modified by an external field [40], or by current via spin transfer torque [180]. Another possible application for this novel magnetic configuration could be as component for all-oxide triplet spin-valve structures [48–50], where the presence of built-in and tunable non-collinearity of the LSMO-LSMO structure, in proximity with a superconductor, could bring to long-range triplet pair generation.

We have demonstrated the potential of our doping scheme to tailor unique magnetic properties, not observed in bulk, namely the long-range coupling reported here for the first time in an all-manganite superlattice. We believe that this is a successful example that opens novel paths to engineer new properties in any material with rich phase diagrams, such as cuprates, ruthenates, nickelates and other transition-metal oxides.

Chapter 5

Proton doping of complex oxide films

In this chapter, the modification of electronic properties of TMOs via proton doping is presented. Preliminary results on manganite and cuprate films will be shown. These examples are indicative of the possibilities offered by proton doping of thin films, and of future applications of RNR, as the key-technique to study such systems.

5.1 Hydrogen in LSMO

The envisioned effect of proton-doping in LSMO is the removal of oxygen atoms from the perovskite structure, following the results of [95]. This in turn gradually reduces the oxidation state of Mn ions from 3+ to 2+, enabling to travel along the phase diagram towards lower hole doping and hence to tune different electronic and magnetic properties. In our experiments, an initial doping level of the LSMO layer x=0.5 was chosen in order to be close to the phase boundary between FM and A-type AF phases, as previously shown in Figure 4.1a.

A sample of composition Pd(5nm)/$La_{0.5}Sr_{0.5}MnO_3$(20nm) was deposited by MBE on LSAT substrates of area 10 x 10 mm^2. The LSMO was epitaxial, with the c-axis oriented perpendicular to the layer. The thickness of the layer corresponds to 52 monolayers. The thin palladium was deposited on the surface as catalyst for

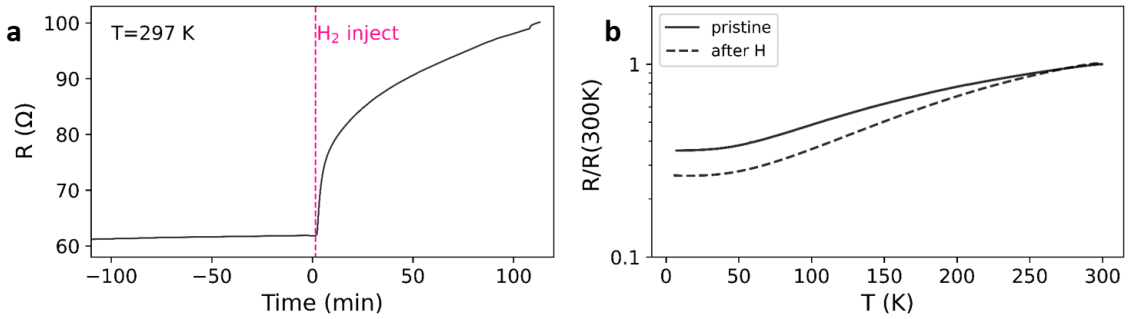

Figure 5.1: *In situ* hydrogen loading and transport measurement of LSMO(x=0.5) thin film. **a**. Room temperature resistance change during hydrogen exposure; **b**. Transport measurement of the pristine and hydrogenated sample.

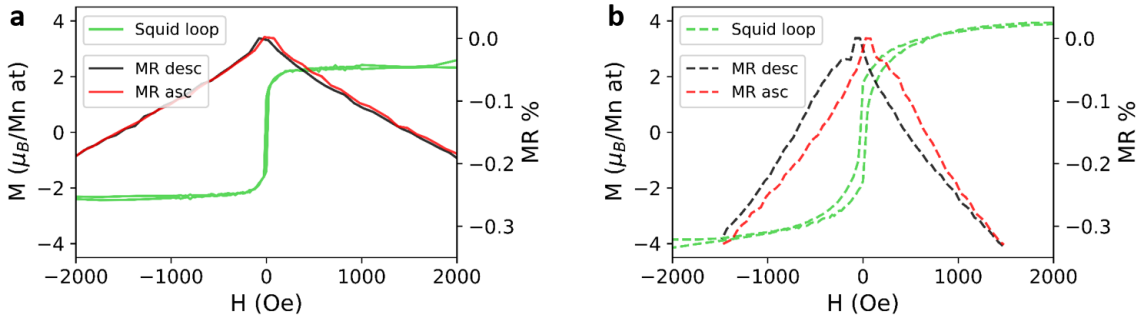

Figure 5.2: Comparison of selected magnetoresistance and hysteresis loops at 50 K before (**a**) and after (**b**) hydrogenation.

hydrogen splitting. The sample was cut in 2 parts of equal area after the growth, which served as pristine and hydrogenation sample. The exposure to 90 mbar of pure hydrogen atmosphere was performed at RT in the cryostat chamber during *in situ* resistance measurement. Figure 5.1 shows the observed resistance increase as soon as the hydrogen was injected. After 110 minutes of exposure, the hydrogen gas was removed from the chamber and the sample was vacuumized.

The characterization of pristine and hydrogenated LSMO started with transport measurements. Figure 5.1b shows the temperature dependent resistance upon cooling for both samples. The metallicity appears increased after the hydrogenation process.

SQUID magnetometry was measured for both samples in a temperature range between 10 and 300 K. Interestingly we found a substantially different behaviour of hysteresis loops before and after hydrogenation. The first discrepancy is observed in the saturation moment, which approaches that of optimally doped LSMO for the hydrogenated sample and is reduced in the whole temperature range for the pristine sample. The reduced moment in the pristine sample can be explained either by a thickness effect, or by the presence of canted A-type antiferromagnetism expected for the x=0.5 doping. As explained in the previous section, the net moment in this case greatly depends on the canting angle γ, which in turn is strongly dependent on the hole doping. The increased moment after hydrogen loading suggests that the sample has now an effective hole doping closer to the optimal x=0.33, with M_{sat}=3.88 μ_B/Mn at. Another difference was observed in the shape of hysteresis loops. Figure 5.2 shows as an example the loops at 50 K (green lines). While for the pristine sample (Panel a) we have a conventional LSMO behaviour, after hydrogenation (Panel b) we observe the opening of a finite coercivity and "wings" typical of exchanged coupled layers. This suggests the presence of two FM layers of different magnetic hardness, aligned non-collinearly with respect to each other at intermediate fields.

The samples were then studied with additional magnetoresistance experiments measured with in-plane current, conducted in a temperature range between 10 and 300 K. The pristine sample shows the classic colossal magnetoresistance present for FM LSMO in the whole temperature range, while for the hydrogenated sample we observe an additional GMR effect with maxima around coercivity and hysteretic behaviour at temperatures below 150 K. Two selected MR curves at 50 K are shown in red and black lines in Figure 5.2 for pristine (a) and hydrogenated sample (b). Another observation that becomes clear from this comparison is the increased steepness of CMR effect in the hydrogenated sample.

In order to unravel the presence of hydrogen atoms in the LSMO layer, comparative neutron reflectometry experiments were performed at the GINA reflectometer, at the Budapest Neutron Center. Room temperature NR measurements were performed on both samples, shown in Figure 5.3a. Due to the low beam intensity, high background, and small area of our samples, only 2 orders of reflectivity were detected, however a clear difference between the two curves was observed at the

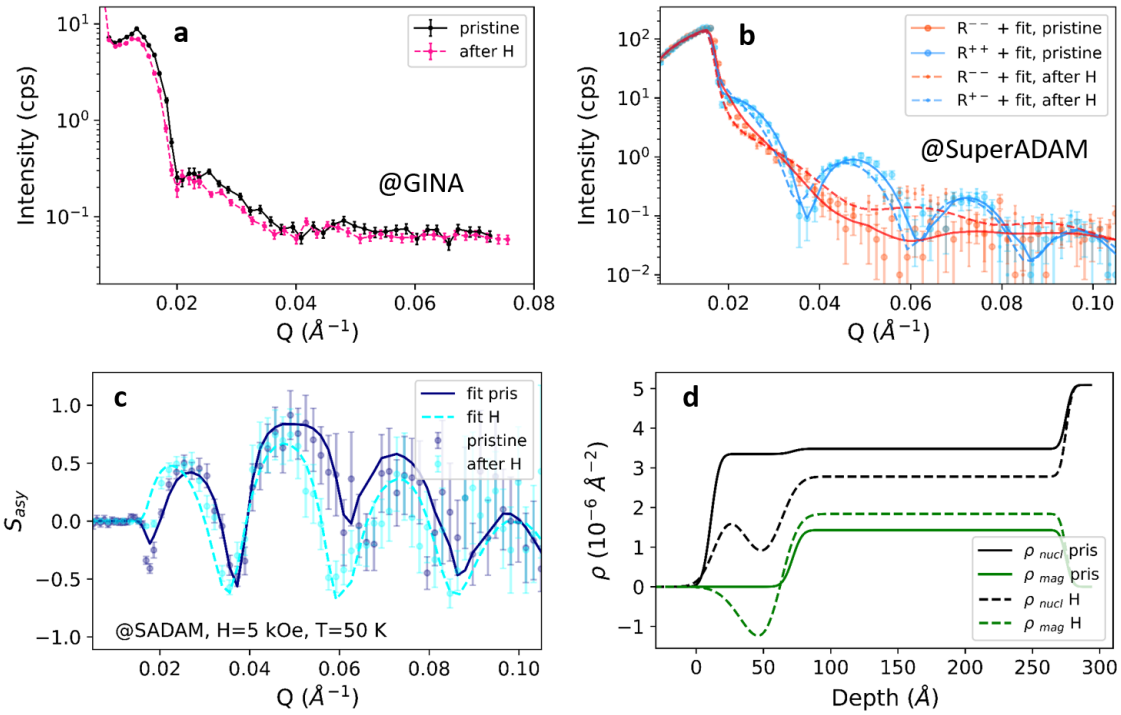

Figure 5.3: Neutron reflectometry experiments on pristine and hydrogenated sample. **a** NR measurements at RT at GINA; **b** PNR measurements at 50 K and 5 kOe at SuperADAM; **c**. Comparison of measured and fitted spin asymmetry for pristine and hydrogenated samples; **d**. Comparison of the fitted SLD nuclear and magnetic profile before and after hydrogen.

critical edge, indicating a smaller SLD of hydrogenated sample.

For a simultaneous study of hydrogen depth profile and depth dependent magnetic properties, PNR measurements were carried out at SuperADAM at various temperatures between 10 and 300 K. A PNR measurement of NSF channels was performed for both samples in saturation condition (H=5 kOe) at 50 K, as shown in Figure 5.3b. In order to better see the magnetic difference between pristine and hydrogenated samples, we can resort to the spin asymmetry, defined as in Eq.2.10. The corresponding data are shown in Figure 5.3c in dark (light) blue for the pristine (hydrogenated) sample. Here we can observe a clearly different signal, indicating different depth dependent magnetic properties, and allowing us to exclude a purely interstitial hydrogen absorption in the system.

A fit of model simulation to the experimental data was performed on both curves. The best fit of nuclear (magnetic) depth profiles are shown in Figure 5.3d as black (green) lines. For the pristine sample, shown in solid lines, we obtained the expected nuclear SLD profile and magnetic moment in the LSMO layer of reduced amplitude (M_{sat}=3.15μ_B/Mn at) with respect to optimally doped LSMO, consistently at least qualitatively with SQUID results. For the present sample, we could not detect the magnetic (0 0 $\frac{1}{2}$) Bragg peak expected for A-type AF order in analogy to the measurement shown in Figure 4.14a. As the LSMO layer of the present sample had only 40% of the thickness of the previous one, the weaker AF peak was probably hidden in the background. For the hydrogenated sample (dashed lines), an additional interface sheet had to be included in the model in between Pd and LSMO layers to improve the fit. According to this model, the hydrogen penetrated the Pd, as we see from the decrease of SLD. This is expected since Pd is a well known hydrogen absorber [181]. Interestingly we also observe a reduced nuclear SLD of the LSMO layer, which could be indicative of hydrogen presence or oxygen vacancies created by the reducing hydrogen atmosphere. If we disregard density changes, in the extreme cases of full hydrogenation and full reduction, this SLD change can be ascribed to either the formation of an oxyhydride of stoichiometry $La_{0.5}Sr_{0.5}MnO_3H_{1.1}$, or to an oxygen deficient structure of formula $La_{0.5}Sr_{0.5}MnO_{2.1}$. The latter stoichiometry is consistent with previous NR experiments on optimally doped LSMO [95], where the use of deuterium allowed to exclude the presence of hydrogen atoms in the oxide. The authors of this work however also comment that the presence of H inside LSMO, measured in other works by SIMS [94], is not to be excluded for *ex situ* measurements (as in our case), when H can be incorporated after the cooling of the sample to balance the charge in the system. At the interface layer we observe a dip in the nuclear profile, suggesting that here lies the majority of the absorbed hydrogen. This is not surprising since we expect the most of defects to be at the interface between two deeply different materials such as LSMO and Pd. Another observation deduced from this fit is the increased magnetic moment in the LSMO layer after hydrogenation (M_{sat}=3.99μ_B/Mn at), once again consistent with SQUID result. The increased moment suggests an electron injection in the system (with subsequent hole annihilation), that could be caused by hydrogen charge transfer as well as

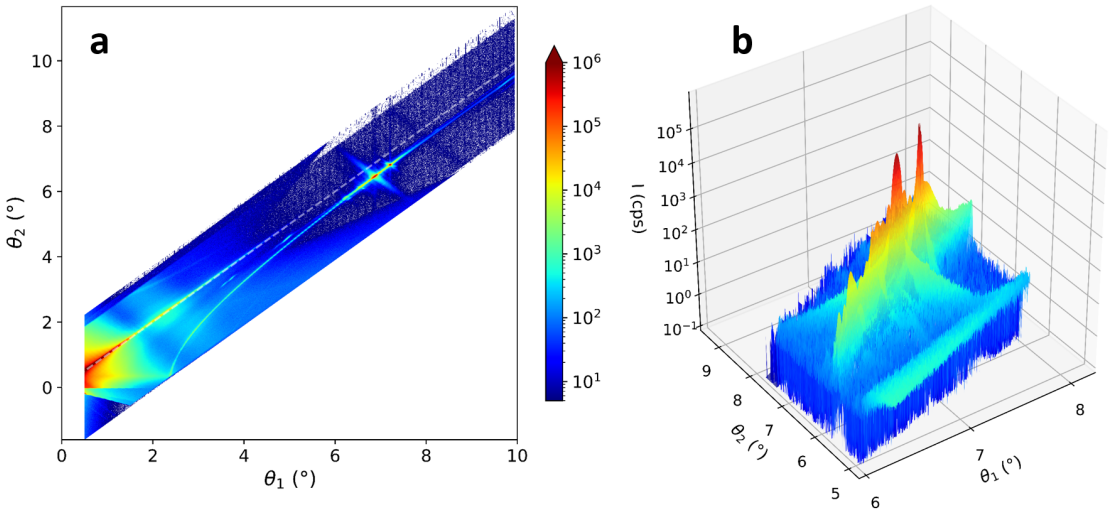

Figure 5.4: Diffuse scattering of pristine LSCO layer. **a**. Full scattering map showing specular (dashed line) and diffuse x-ray intensity; **b**. 3D map around the (002) LSCO Bragg peak.

oxygen deficiency as previously found by Refs. [94, 95]. Finally, we observed an induced magnetic moment with opposite sign to that of LSMO in the interface region. Even though this signal could be an artifact of the fitting process, this AP alignment would be consistent with the GMR effect observed in the magnetoresistance measurement.

In summary, we were able to modify the magnetic properties of LSMO layer by varying the effective hole doping via exposure of hydrogen at room temperature. The sample showed increased metallicity, bigger saturation moment, and emergence of GMR after 100 minutes in pure hydrogen gas atmosphere. This is an interesting example of the huge impact of hydrogen exposure on the electronic properties of oxide layers, which opens the way for proton-controlled spintronics.

5.2 Hydrogen in LSCO

Hydrogen atmosphere has also an impact on superconducting (SC) cuprate thin film. Our preliminary experiments show that it is possible to modify the crystal structure and electronic properties of $La_{2-x}Sr_xCuO_4$ (LSCO) layers via hydrogen

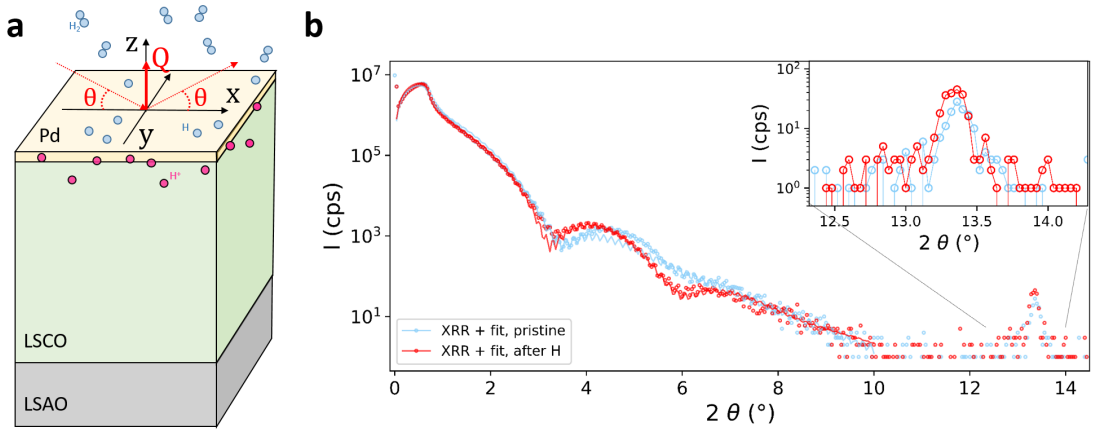

Figure 5.5: Hydrogenation of cuprate thin layer. **a**. Sketch of the sample showing scattering geometry of XRR experiment; **b**. Comparison of the XRR/XRD intensity measured before (azure) and after (red) hydrogen. Inset: zoom of the (002) LSCO Bragg peak. **c** Mutual inductance measurement before and after hydrogen exposure.

exposure at room temperature.

A sample of composition Pd(5nm)/$La_{1.84}Sr_{0.16}CuO_4$(50nm) was deposited by epitaxial MBE growth on LSAO substrates of area 10 x 10 mm^2. The nominal sample thickness corresponded to 130 monolayers of LSCO. The thin palladium was deposited on the surface as catalyst for hydrogen splitting.

The as-grown sample was first characterized by x-ray reflectometry. In Figure 5.4a we show the scattering map of the pristine sample reconstructed thanks to the use of the 1D detector. The reflectivity curve is found in the specular channel, shown as a white dashed line, while the diffuse scattering is found in the off-specular area. The first interesting observation from this measurement is that the the (002) Bragg peak of LSCO (found at $\theta \approx 6.7°$) is not centered on the specular channels. This means that the film c-axis was initially tilted of around 0.4° with respect to the substrate surface. A 3D representation of the scattered intensity around the Bragg peak is shown in Figure 5.4b, where we can observe the main and secondary reflections. Another feature found in the diffuse scattering is the parabolic signal known as Bragg sheet, which is normally the indication of μm distanced striped in either the substrate or the film itself.

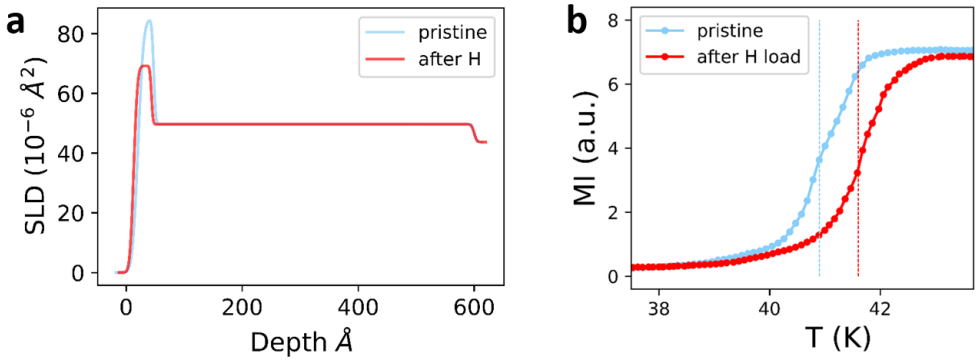

Figure 5.6: Hydrogenation effects on LSCO layer. **a**. Comparison of the SLD profiles obtained from XRR measured before (azure) and after (red) hydrogen; **b** Mutual inductance measurement before and after hydrogen exposure.

The sample was exposed to 10 mbar of pure H_2 at RT in the sample chamber, during *in situ* XRR measurement. A sketch of the sample and measurement geometry is shown in Figure 5.5a.

Figure 5.5b shows the specular cut of pristine and hydrogenated sample. The XRR curves (in the region up to circa 10°) both show 2 sets of Kiessig oscillations, a slow one related to the thickness of Pd, and a fast one related to the thickness of LSCO. At $2\theta \simeq 13.3°$ we observe the tail of the (002) Bragg peak, shown in the inset of Figure 5.5b. From the comparison of both measurement we can see that the major difference in reflectivity is observed on the slow oscillations, corresponding to a change in Pd thickness, expected due to hydrogen absorption. This was confirmed with the fitting of XRR data, shown as solid lines in Figure 5.5b. The comparison between SLD depth profiles is shown in Figure 5.6a, where we observe not only a slight thickness increase of Pd, but also a significant decrease of scattering potential, indicating a reduced density after H absorption. In the higher angles region (above 10°) we also observe a small difference in the LSCO Bragg peak, with an increased intensity and slight shift to lower angles. The slight shift of the Bragg peak to lower angles is indicative of an expansion of the c axis. The increased broadness of the peak on the other hand indicates that the modification of LSCO layer are not homogenous along the whole sample depth.

Mutual inductance (MI) measurements were employed to measure the super-

conducting transition temperature T_c in the pristine and hydrogenated sample. The technique is based on the Meissner effect, which makes the MI signal go to 0 when the magnetic field is expelled by the superconductor. Interestingly, MI measurements performed after the hydrogen exposure showed a small, yet seizable increase of the superconducting temperature T_c of almost 1 K. The proposed explanation for such effect is that starting from a slightly overdoped LSCO, hydrogen sequestrated few oxygen atoms, decreasing the overall hole concentration to approach the optimal doping.

Further investigations will be needed on these systems, which proved to be an interesting playground for using hydrogen exposure as the knob to travel through the phase diagram.

Conclusions and outlook

In summary, during my doctoral studies we developed a new method for the detection of hydrogen in thin films, which offers higher sensitivity and lower counting time with respect to conventional NR, while retaining the advantages of neutron methods, namely the direct detection of hydrogen atoms, the possibility to study *in situ* processes, and the absence of damage to the sample. These improvements could allow the testing of new candidate hydrogen storage materials, which are supposed to uptake and release hydrogen as fast as possible. In this case the study of these fast kinetics would be greatly aided by the fixed-Q RNR method, in which the counting time can be reduced to the sub-second range. On the other hand the high sensitivity that can be reached with RNR could help to answer some dilemmas which still have no explanation in the field of H-doping of complex materials. For example in the case of iron-based superconductors, where a sizeable increase of the superconducting temperature upon H intercalation was realized [87], a clear quantification of the H dopant incorporated has not yet been carried out. Other systems which are not yet fully comprehended are the nickelates reduced via topotactic reaction, and in general the effect of H exposure in TMOs. As it was explained in the previous chapter, it is still not clear whether hydrogen is effectively absorbed in interstitial sites, if it sequestrates oxygen atoms to form water, or if it bonds to oxygen to form hydroxyl groups. In this sense neutron methods, in combination with isotopic substitution, are extremely important, as they allow the clear distinction between the loss of oxygen and the incorporation of hydrogen (or deuterium), as shown in ref [95].

An additional advantage of RNR is the use of non-collinear magnetism to detect the resonance position. As we explained in Chapter 2.1.2, this is not a mandatory requirement for the method, but it has some specific advantages that must be

taken into account. On one hand, it allows the direct observation of hydrogen-related magnetic transitions, such as those explained in the outlook of Section 3.1. This is of particular interest because it is well known that hydrogen can be used to tune in a reversible way certain magnetic properties, such as the perpendicular magnetic anisotropy (Ref. [83]) and long range exchange coupling of thin film heterostructures (Ref. [79]). Many groups are moving in this direction, realizing proton-based devices [42, 182]. RNR measurements on such systems would allow the study of the dynamics of these transition, while also knowing the exact content of hydrogen absorbed.

Another interesting perspective comes directly from the newly found tunable non-collinear phase presented in Chapter 4. We have shown the growth of depth-modulated hole doped manganite superlattices, in which the thickness of the over-doped spacer is a control parameter for the magnetic properties of the entire structure. In particular, at intermediate spacer thickness, temperature and magnetic field we observed a 'fan-like' configuration of the magnetic moments, where consecutive ferromagnetic layers point to a specific angle α. This angle is a direct indication of the degree of non-collinearity of this system, and it can be varied with the application of small magnetic fields. We have also shown a preliminary device operation for this homojunction, with the application of in-plane electric current, and voltage. We were able to switch between two distinct resistive states, corresponding to high and low non collinearity, with the cycling of magnetic field. A much bigger response is predicted for electric currents applied in the out-of-plane direction, where we expect to observe giant magnetoresistive effects.

Taking inspiration from the previous studies of synthetic antiferromagnets such as Fe/Nb [79] and Fe/V [78], the question that comes to mind is whether hydrogen could also be a control parameter for the long-range magnetic order found in manganite homojunctions. Ours and other groups' preliminary studies indicate that it is possible to modify the structural, electrical and magnetic properties of LSMO thin films with hydrogen. Future studies on *in situ* hydrogen exposure of manganite homojunctions will hopefully shed light on this intriguing question.

Bibliography

[1] E. Acosta. Thin films/properties and applications. In Alicia Esther Ares, editor, *Thin Films*, chapter 1. IntechOpen, 2021.

[2] F. Radu and H. Zabel. *Exchange Bias Effect of Ferro-/Antiferromagnetic Heterostructures*, pages 97–184. Springer Berlin Heidelberg, Berlin, Heidelberg, 2008.

[3] A. I. Buzdin. Proximity effects in superconductor-ferromagnet heterostructures. *Rev. Mod. Phys.*, 77:935–976, Sep 2005.

[4] B. Heinrich and J.F. Cochran. Ultrathin metallic magnetic films: magnetic anisotropies and exchange interactions. *Advances in Physics*, 42(5):523–639, 1993.

[5] W. Gil, D. Görlitz, M. Horisberger, and J. Kötzler. Magnetoresistance anisotropy of polycrystalline cobalt films: Geometrical-size and domain effects. *Phys. Rev. B*, 72:134401, Oct 2005.

[6] P. F. Carcia. Perpendicular magnetic anisotropy in Pd/Co and Pt/Co thin-film layered structures. *Journal of Applied Physics*, 63(10):5066–5073, 1988.

[7] J. Chakhalian, J. W. Freeland, A. J. Millis, C. Panagopoulos, and J. M. Rondinelli. Colloquium: Emergent properties in plane view: Strong correlations at oxide interfaces. *Rev. Mod. Phys.*, 86:1189–1202, Oct 2014.

[8] H. Hwang, Y. Iwasa, M. Kawasaki, B. Keimer, N. Nagaosa, and Y. Tokura. Emergent phenomena at oxide interfaces. *Nature Materials*, 11:103–113, July 2012.

[9] K. S. Takahashi, M. Kawasaki, and Y. Tokura. Interface ferromagnetism in oxide superlattices of $CaMnO_3/CaRuO_3$. *Applied Physics Letters*, 79(9):1324–1326, 2001.

[10] J. W. Freeland, J. Chakhalian, A. V. Boris, J.-M. Tonnerre, J. J. Kavich, P. Yordanov, S. Grenier, P. Zschack, E. Karapetrova, P. Popovich, H. N. Lee, and B. Keimer. Charge transport and magnetization profile at the interface between the correlated metal $CaRuO_3$ and the antiferromagnetic insulator $CaMnO_3$. *Phys. Rev. B*, 81:094414, Mar 2010.

[11] J. D. Hoffman, B. J. Kirby, J. Kwon, G. Fabbris, and D. et al. Meyers. Oscillatory noncollinear magnetism induced by interfacial charge transfer in superlattices composed of metallic oxides. *Phys. Rev. X*, 6:041038, Nov 2016.

[12] J. Chakhalian, J. W. Freeland, H.-U. Habermeier, G. Cristiani, G. Khaliullin, M. van Veenendaal, and B. Keimer. Orbital reconstruction and covalent bonding at an oxide interface. *Science*, 318(5853):1114–1117, 2007.

[13] J. Chakhalian, J. W. Freeland, and G. et al. Srajer. Magnetism at the interface between ferromagnetic and superconducting oxides. *Nat. Phys.*, 2:244–248, 2006.

[14] T. Chien, L. Kourkoutis, J. Chakhalian, B. Gray, M. Kareev, N. P. Guisinger, D. A. Muller, and J. W. Freeland. Visualizing short-range charge transfer at the interfaces between ferromagnetic and superconducting oxides. *Nat. Comm.*, 4:2336, 2013.

[15] G. Kim, Y. Khaydukov, M. Bluschke, Y. E. Suyolcu, G. Christiani, K. Son, C. Dietl, T. Keller, E. Weschke, P. A. van Aken, G. Logvenov, and B. Keimer. Tunable perpendicular exchange bias in oxide heterostructures. *Phys. Rev. Materials*, 3:084420, Aug 2019.

[16] M. Gibert, P. Zubko, R. Scherwitzl, J. Iniguez, and J. Triscone. Exchange bias in $LaNiO_3$–$LaMnO_3$ superlattices. *Nature Materials*, 11:195–198, Jan 2012.

[17] M. Fan, W. Zhang, J. Jian, J. Huang, and H. Wang. Strong perpendicular exchange bias in epitaxial $La_{0.7}Sr_{0.3}MnO_3$:$LaFeO_3$ nanocomposite thin films. *APL Materials*, 4(7):076105, 2016.

[18] H. Bhatt, Y. Kumar, C. L. Prajapat, C. J. Kinane, A. Caruana, S. Langridge, S. Basu, and S. Singh. Emergent interfacial ferromagnetism and exchange bias effect in paramagnetic/ferromagnetic oxide heterostructures. *Advanced Materials Interfaces*, 7(21):2001172, 2020.

[19] D. Yi, J. Liu, S. Hsu, L. Zhang, Y. Choi, J. Kim, Z. Chen, J. D. Clarkson, C. R. Serrao, E. Arenholz, P. J. Ryan, H. Xu, R. J. Birgeneau, and R. Ramesh. Atomic-scale control of magnetic anisotropy via novel spin–orbit coupling effect in $La_{2/3}Sr_{1/3}MnO_3/SrIrO_3$ superlattices. *Proceedings of the National Academy of Sciences*, 113(23):6397–6402, 2016.

[20] D. Yi, C. L. Flint, P. P. Balakrishnan, K. Mahalingam, B. Urwin, A. Vailionis, A. T. N'Diaye, P. Shafer, E. Arenholz, Y. Choi, K. H. Stone, J. Chu, B. M. Howe, J. Liu, I. R. Fisher, and Y. Suzuki. Tuning perpendicular magnetic anisotropy by oxygen octahedral rotations in $(La_{1-x}Sr_xMnO_3)/(SrIrO_3)$ superlattices. *Phys. Rev. Lett.*, 119:077201, Aug 2017.

[21] J. Stahn, J. Chakhalian, Ch. Niedermayer, J. Hoppler, T. Gutberlet, J. Voigt, F. Treubel, H-U. Habermeier, G. Cristiani, B. Keimer, and C. Bernhard. Magnetic proximity effect in perovskite superconductor/ferromagnet multilayers. *Phys. Rev. B*, 71:140509, Apr 2005.

[22] M. A. Uribe-Laverde, D. K. Satapathy, I. Marozau, V. K. Malik, S. Das, K. Sen, J. Stahn, A. Rühm, J.-H. Kim, T. Keller, A. Devishvili, B. P. Toperverg, and C. Bernhard. Depth profile of the ferromagnetic order in a $YBa_2Cu_3O_7/La_{2/3}Ca_{1/3}MnO_3$ superlattice on a lsat substrate: A polarized neutron reflectometry study. *Phys. Rev. B*, 87:115105, Mar 2013.

[23] M. Saghayezhian, S. Kouser, Z. Wang, H. Guo, R. Jin, J. Zhang, Y. Zhu, S. T. Pantelides, and E. W. Plummer. Atomic-scale determination of spon-

taneous magnetic reversal in oxide heterostructures. *Proceedings of the National Academy of Sciences*, 116(21):10309–10316, 2019.

[24] J.-H. Kim, I. Vrejoiu, Y. Khaydukov, T. Keller, J. Stahn, A. Rühm, D. K. Satapathy, V. Hinkov, and B. Keimer. Competing interactions at the interface between ferromagnetic oxides revealed by spin-polarized neutron reflectometry. *Phys. Rev. B*, 86:180402, Nov 2012.

[25] S. M. Wu, S. A. Cybart, P. Yu, M. D. Rossell, J. X. Zhang, R. Ramesh, and R. C. Dynes. Reversible electric control of exchange bias in a multiferroic field-effect device. *Nature Materials*, 9:756–761, July 2010.

[26] F. A. Cuellar, Y. H. Liu, and J. et al. Salafranca. Reversible electric-field control of magnetization at oxide interfaces. *Nature Communications*, 5:4215, Jun 2014.

[27] T. Koida, M. Lippmaa, T. Fukumura, K. Itaka, Y. Matsumoto, M. Kawasaki, and H. Koinuma. Effect of a-site cation ordering on the magnetoelectric properties in $[(\mathrm{lamno_3})_m/(\mathrm{srmno_3})_m]_n$ artificial superlattices. *Phys. Rev. B*, 66:144418, Oct 2002.

[28] S. J. May, P. J. Ryan, J. L. Robertson, Kim J.-W., T. S. Santos, E. Karapetrova, J. Zarestky, X. Zhai, S. G. E. te Velthuis, J. N. Eckstein, S. D. Bader, and A. Bhattacharya. Enhanced ordering temperatures in antiferromagnetic manganite superlattices. *Nature Materials*, 8:892–897, 2009.

[29] A. Bhattacharya, S. J. May, S. G. E. te Velthuis, M. Warusawithana, X. Zhai, Bin Jiang, J.-M. Zuo, M. R. Fitzsimmons, S. D. Bader, and J. N. Eckstein. Metal-insulator transition and its relation to magnetic structure in $(\mathrm{LaMnO_3})_{2n}/(\mathrm{SrMnO_3})_n$ superlattices. *Phys. Rev. Lett.*, 100:257203, Jun 2008.

[30] F. Baiutti, G. Logvenov, G. Gregori, G. Cristiani, Y. Wang, W. Sigle, P. A. van Aken, and J. Maier. High-temperature superconductivity in space-charge regions of lanthanum cuprate induced by two-dimensional doping. *Nat. Comm.*, 6:8586, 2015.

[31] G. Binasch, P. Grünberg, F. Saurenbach, and W. Zinn. Enhanced magnetoresistance in layered magnetic structures with antiferromagnetic interlayer exchange. *Phys. Rev. B*, 39:4828–4830, Mar 1989.

[32] M. N. Baibich, J. M. Broto, A. Fert, F. Nguyen Van Dau, F. Petroff, P. Etienne, G. Creuzet, A. Friederich, and J. Chazelas. Giant magnetoresistance of (001)Fe/(001)Cr magnetic superlattices. *Phys. Rev. Lett.*, 61:2472–2475, Nov 1988.

[33] R.A. Duine, K.J. Lee, and S.S.P. et al. Parkin. Synthetic antiferromagnetic spintronics. *Nature Physics*, 14:217–219, 2018.

[34] K. R. Nikolaev, A. Bhattacharya, P. A. Kraus, V. A. Vas'ko, W. K. Cooley, and A. M. Goldman. Indications of antiferromagnetic interlayer coupling in $La_{2/3}Ba_{1/3}MnO_3/LaNiO_3$ multilayers. *Applied Physics Letters*, 75(1):118–120, 1999.

[35] K. R. Nikolaev, A. Yu. Dobin, I. N. Krivorotov, W. K. Cooley, A. Bhattacharya, A. L. Kobrinskii, L. I. Glazman, R. M. Wentzovitch, E. Dan Dahlberg, and A. M. Goldman. Oscillatory exchange coupling and positive magnetoresistance in epitaxial oxide heterostructures. *Phys. Rev. Lett.*, 85:3728–3731, Oct 2000.

[36] W. Lü, S. Saha, X. Wang, X. R. Wang, Z. Q. Liu, K. Gopinadhan, A. Annadi, S. W. Zeng, Z. Huang, B. C. Bao, C. X. Cong, M. Venkatesan, T. Yu, J. M. D. Coey, Ariando, and T. Venkatesan. Long-range magnetic coupling across a polar insulating layer. *Nature Communications*, 7:11015, 2016.

[37] B. Chen, H. Xu, C. Ma, S. Mattauch, D. Lan, F. Jin, Z. Guo, S. Wan, P. Chen, G. Gao, F. Chen, Y. Su, and W. Wu. All-oxide–based synthetic antiferromagnets exhibiting layer-resolved magnetization reversal. *Science*, 357(6347):191–194, 2017.

[38] M. Gibert, M. Viret, P. Zubko, N. Jaouen, J.-M. Tonnerre, A. Torres-Pardo, S. Catalano, A. Gloter, O. Stéphan, and J.-M. Triscone. Interlayer coupling through a dimensionality-induced magnetic state. *Nature Communications*, 7:11227, Apr 2016.

[39] J.C. Slonczewski. Overview of interlayer exchange theory. *Journal of Magnetism and Magnetic Materials*, 150(1):13 – 24, 1995.

[40] J. D. Hoffman, S. M. Wu, B. J. Kirby, and A. Bhattacharya. Tunable noncollinear antiferromagnetic resistive memory through oxide superlattice design. *Phys. Rev. Applied*, 9:044041, Apr 2018.

[41] P.X. Qin, H. Yan, X.N. Wang, Z.X. Feng, H.X. Guo, X.R. Zhou, H.J. Wu, X. Zhang, Z.G.G. Leng, H.Y. Chen, and Z.Q. Liu. Noncollinear spintronics and electric-field control: a review. *Rare Met.*, 39:95–112, 2020.

[42] D. Ielmini. Brain-inspired computing with resistive switching memory (RRAM): Devices, synapses and neural networks. *Microelectronic Engineering*, 190:44–53, 2018.

[43] Y.V. Fominov, A.A. Golubov, T.Y. Karminskaya, M. Yu. Kupriyanov, R. G. Deminov, and L. R. Tagirov. Superconducting triplet spin valve. *Jetp Lett.*, 91:308–313, 2010.

[44] V. I. Zdravkov, J. Kehrle, G. Obermeier, D. Lenk, H.-A. Krug von Nidda, C. Müller, M. Yu. Kupriyanov, A. S. Sidorenko, S. Horn, R. Tidecks, and L. R. Tagirov. Experimental observation of the triplet spin-valve effect in a superconductor-ferromagnet heterostructure. *Phys. Rev. B*, 87:144507, Apr 2013.

[45] J. Hoppler, J. Stahn, C. Niedermayer, V. K. Malik, H. Bouyanfif, A. J. Drew, M. Rössle, A. Buzdin, G. Cristiani, H.-U. Habermeier, B. Keimer, and C. Bernhard. Giant superconductivity-induced modulation of the ferromagnetic magnetization in a cuprate–manganite superlattice. *Nature Materials*, 8:315–319, 2009.

[46] V. Peña, Z. Sefrioui, D. Arias, C. Leon, J. Santamaria, J. L. Martinez, S. G. E. te Velthuis, and A. Hoffmann. Giant magnetoresistance in ferromagnet/superconductor superlattices. *Phys. Rev. Lett.*, 94:057002, Feb 2005.

[47] D. K. Satapathy, M. A. Uribe-Laverde, I. Marozau, V. K. Malik, S. Das, Th. Wagner, C. Marcelot, J. Stahn, S. Brück, A. Rühm, S. Macke, T. Tietze, E. Goering, A. Frañó, J. H. Kim, M. Wu, E. Benckiser, B. Keimer, A. Devishvili, B. P. Toperverg, M. Merz, P. Nagel, S. Schuppler, and C. Bernhard. Magnetic proximity effect in $yba_2cu_3o_7/la_{2/3}ca_{1/3}mno_3$ and $yba_2cu_3o_7/lamno_{3+\delta}$ superlattices. *Phys. Rev. Lett.*, 108:197201, May 2012.

[48] Yoav Kalcheim, Tal Kirzhner, Gad Koren, and Oded Millo. Long-range proximity effect in $La_{2/3}Ca_{1/3}MnO_3/(100)YBa_2Cu_3O_{7-\delta}$ ferromagnet/superconductor bilayers: Evidence for induced triplet superconductivity in the ferromagnet. *Phys. Rev. B*, 83:064510, Feb 2011.

[49] C. Visani, Z. Sefrioui, J. Tornos, C. Leon, J. Briatico, M. Bibes, A. Barthélémy, J. Santamaría, and Javier E. Villegas. Equal-spin Andreev reflection and long-range coherent transport in high-temperature superconductor/half-metallic ferromagnet junctions. *Nature Physics*, 8:539–543, 2012.

[50] Yu. N. Khaydukov, G. A. Ovsyannikov, A. E. Sheyerman, K. Y. Constantinian, L. Mustafa, T. Keller, M. A. Uribe-Laverde, Yu. V. Kislinskii, A. V. Shadrin, A. Kalaboukhov, B. Keimer, and D. Winkler. Evidence for spin-triplet superconducting correlations in metal-oxide heterostructures with noncollinear magnetization. *Phys. Rev. B*, 90:035130, Jul 2014.

[51] S.Y. Lee, J.H. Lee, Y.H. Kim, J.W. Kim, K.J. Lee, and S.J. Park. Recent progress using solid-state materials for hydrogen storage: A short review. *Processes*, 10(2), 2022.

[52] F. Ding and B. I. Yakobson. Challenges in hydrogen adsorptions: from physisorption to chemisorption. *Frontiers of Physics*, 6(2):142–150, 2011.

[53] M. Z. Jacobson, W. G. Colella, and D. M. Golden. Cleaning the air and improving health with hydrogen fuel-cell vehicles. *Science*, 308(5730):1901–1905, 2005.

[54] Q. Wang and K. Domen. Particulate photocatalysts for light-driven water splitting: Mechanisms, challenges, and design strategies. *Chemical Reviews*, 120(2):919–985, 2020. PMID: 31393702.

[55] J. Roth, E. Tsitrone, A. Loarte, Th. Loarer, G. Counsell, R. Neu, V. Philipps, S. Brezinsek, M. Lehnen, P. Coad, Ch. Grisolia, K. Schmid, K. Krieger, A. Kallenbach, B. Lipschultz, R. Doerner, R. Causey, V. Alimov, W. Shu, O. Ogorodnikova, A. Kirschner, G. Federici, and A. Kukushkin. Recent analysis of key plasma wall interactions issues for ITER. *Journal of Nuclear Materials*, 390-391:1–9, 2009. Proceedings of the 18th International Conference on Plasma-Surface Interactions in Controlled Fusion Device.

[56] I. Staffell, D. Scamman, A. Velazquez Abad, P. Balcombe, P. E. Dodds, P. Ekins, N. Shah, and K. R. Ward. The role of hydrogen and fuel cells in the global energy system. *Energy Environ. Sci.*, 12:463–491, 2019.

[57] E. Boateng and A. Chen. Recent advances in nanomaterial-based solid-state hydrogen storage. *Materials Today Advances*, 6:100022, 2020.

[58] A. Züttel. Materials for hydrogen storage. *Materials Today*, 6(9):24–33, 2003.

[59] I.A. Hassan, H. S. Ramadan, M. A. Saleh, and D. Hissel. Hydrogen storage technologies for stationary and mobile applications: Review, analysis and perspectives. *Renewable and Sustainable Energy Reviews*, 149:111311, 2021.

[60] Zhen Chen, Zhongliang Ma, Jie Zheng, Xingguo Li, Etsuo Akiba, and Hai-Wen Li. Perspectives and challenges of hydrogen storage in solid-state hydrides. *Chinese Journal of Chemical Engineering*, 29:1–12, 2021.

[61] Ying Wang and Yijing Wang. Recent advances in additive-enhanced magnesium hydride for hydrogen storage. *Progress in Natural Science: Materials International*, 27(1):41–49, 2017. SI-HYDROGEN STORAGE MATERIALS.

[62] T.Y. Wei, K.L. Lim, Y.S. Tseng, and S.L.I. Chan. A review on the characterization of hydrogen in hydrogen storage materials. *Renewable and Sustainable Energy Reviews*, 79:1122–1133, 2017.

[63] L. Pasquini. Design of nanomaterials for hydrogen storage. *Energies*, 13(13), 2020.

[64] L. Jinzhe, A. M. Lider, and V. N. Kudiiarov. An overview of progress in mg-based hydrogen storage films. *Chinese Physics B*, 28(9):098801, sep 2019.

[65] G. Song, A. Remhof, D. Labergerie, and H. Zabel. Kinetics of hydrogen absorption and desorption in epitaxial thin niobium films. *Phys. Rev. B*, 66:045407, Jul 2002.

[66] J. N. Huiberts, R. Griessen, J. H. Rector, R. J. Wijngaarden, J. P. Dekker, D. G. de Groot, and N. J. Koeman. Yttrium and lanthanum hydride films with switchable optical properties. *Nature*, 380:231–234, 1996.

[67] F. A. Stevie, C. Zhou, M. Hopstaken, M. Saccomanno, Z. Zhang, and A. Turansky. SIMS measurement of hydrogen and deuterium detection limits in silicon: Comparison of different SIMS instrumentation. *Journal of Vacuum Science & Technology B*, 34(3):03H103, 2016.

[68] A. Benninghoven, P. Beckmann, D. Greifendorf, K.-H. Müller, and M. Schemmer. Hydrogen detection by secondary ion mass spectroscopy: Hydrogen on polycrystalline nickel. *Surface Science*, 107(1):148–164, 1981.

[69] W. Assmann, H. Huber, Ch. Steinhausen, M. Dobler, H. Glückler, and A. Weidinger. Elastic recoil detection analysis with heavy ions. *Nuclear Instruments and Methods in Physics Research Section B: Beam Interactions with Materials and Atoms*, 89(1):131 – 139, 1994.

[70] J. Daillant and A. Gibaud. *X-ray and Neutron Reflectivity: principles and applications*. Springer, 2009.

[71] G. Song, M. Geitz, A. Abromeit, and H. Zabel. Solubility isotherms of hydrogen in epitaxial Nb(110) films. *Phys. Rev. B*, 54:14093–14101, Nov 1996.

[72] N. M. Jisrawi, M. W. Ruckman, T. R. Thurston, G. Reisfeld, M. Weinert, M. Strongin, and M. Gurvitch. Reversible depression in the T_c of thin Nb films due to enhanced hydrogen adsorption. *Phys. Rev. B*, 58:6585–6590, Sep 1998.

[73] H. Fritzsche, W.P. Kalisvaart, B. Zahiri, R. Flacau, and D. Mitlin. The catalytic effect of Fe and Cr on hydrogen and deuterium absorption in Mg thin films. *International Journal of Hydrogen Energy*, 37(4):3540–3547, 2012. International Conference on Renewable Energy (ICRE 2011).

[74] S. J. Callori, C. Rehm, G. L. Causer, M. Kostylev, and F. Klose. Hydrogen absorption in metal thin films and heterostructures investigated in situ with neutron and x-ray scattering. *Metals*, 6, 2016.

[75] W.P. Kalisvaart, E.J. Luber, E. Poirier, C.T. Harrower, A. Teichert, D. Wallacher, N. Grimm, R. Steitz, H. Fritzsche, and D. Mitlin. Probing the room temperature deuterium absorption kinetics in nanoscale magnesium based hydrogen storage multilayers using neutron reflectometry, x-ray diffraction, and atomic force microscopy. *The Journal of Physical Chemistry C*, 116(9):5868–5880, 2012.

[76] Ch. Rehm, H. Fritzsche, H. Maletta, and F. Klose. Hydrogen concentration and its relation to interplanar spacing and layer thickness of 1000-Å Nb(110) films during in situ hydrogen charging experiments. *Phys. Rev. B*, 59:3142–3152, Jan 1999.

[77] V. Leiner, K. Westerholt, B. Hj rvarsson, and H. Zabel. Tunability of the interlayer exchange coupling. *Journal of Physics D: Applied Physics*, 35(19):2377–2383, sep 2002.

[78] B. Hjörvarsson, J. A. Dura, P. Isberg, T. Watanabe, T. J. Udovic, G. Andersson, and C. F. Majkrzak. Reversible Tuning of the Magnetic Exchange Coupling in Fe/V (001) Superlattices Using Hydrogen. *Phys. Rev. Lett.*, 79:901–904, Aug 1997.

[79] F. Klose, Ch. Rehm, D. Nagengast, H. Maletta, and A. Weidinger. Continuous and Reversible Change of the Magnetic Coupling in an Fe/Nb Multilayer Induced by Hydrogen Charging. *Phys. Rev. Lett.*, 78:1150–1153, Feb 1997.

[80] E. Kravtsov, A. Nefedov, G. Nowak, K. Zhernenkov, H. Zabel, B. Hjörvarsson, A. Liebig, A. Hoser, G. J. McIntyre, L. Paolasini, and A. Remhof. Fine-tuning of the spin-density-wave state in Cr/V heterostructures via hydrogen uptake. *Journal of Physics: Condensed Matter*, 21(33):336004, jul 2009.

[81] S. Watt and M. Kostylev. Manipulation of the inverse spin Hall effect in palladium by absorption of hydrogen gas. *Phys. Rev. B*, Accepted 24 April 2020, 2020.

[82] P.C. Chang, T.H. Chuang, D.H. Wei, and W.C. Lin. Thermally modulated hydrogenation in FePd alloy films: Temperature-driven peculiar variation of magnetism. *Applied Physics Letters*, 116(10):102407, 2020.

[83] A. J. Tan, M. Huang, C. O. Avci, F. Büttner, M. Mann, W. Hu, C. Mazzoli, S. Wilkins, H. L. Tuller, and G. S. D. Beach. Magneto-ionic control of magnetism using a solid-state proton pump. *Nature Materials*, 18:35 – 41, 2019.

[84] M. Wang and Y. Feng. Palladium–silver thin film for hydrogen sensing. *Sensors and Actuators B: Chemical*, 123(1):101 – 106, 2007.

[85] P. S. Chauhan and S. Bhattacharya. Hydrogen gas sensing methods, materials, and approach to achieve parts per billion level detection: A review. *International Journal of Hydrogen Energy*, 44(47):26076 – 26099, 2019.

[86] G. Jiménez-Cadena, J. Riu, and F. X. Rius. Gas sensors based on nanostructured materials. *Analyst*, 132:1083–1099, 2007.

[87] Y. Cui, G. Zhang, H. Li, H. Lin, X. Zhu, H. Wen, G. Wang, J. Sun, M. Ma, Y. Li, D. Gong, T. Xie, Y. Gu, S. Li, H. Luo, P. Yu, and W. Yu. Protonation induced high-Tc phases in iron-based superconductors evidenced by NMR and magnetization measurements. *Science Bulletin*, 63(1):11 – 16, 2018.

[88] J. Shi, Y. Zhou, and R. Ramanathan. Colossal resistance switching and band gap modulation in a perovskite nickelate by electron doping. *Nat. Comm.*, 5, Sep 2014.

[89] H.T. Zhang, T. J. Park, A. N. M. N. Islam, and D. S. J. et al. Tran. Reconfigurable perovskite nickelate electronics for artificial intelligence. *Science*, 375(6580):533–539, 2022.

[90] D. Li, K. Lee, B.Y. Wang, M. Osada, S. Crossley, H.R. Lee, Y. Cui, Y. Hikita, and H.Y. Hwang. Superconductivity in an infinite-layer nickelate. *Nature*, 572:624–627, 2019.

[91] Liang Si, Wen Xiao, Josef Kaufmann, Jan M. Tomczak, Yi Lu, Zhicheng Zhong, and Karsten Held. Topotactic hydrogen in nickelate superconductors and akin infinite-layer oxides ABO_2. *Phys. Rev. Lett.*, 124:166402, Apr 2020.

[92] J. Chen, Y. Zhou, S. Middey, J. Jiang, N. Chen, L. Chen, X. Shi, M. Döbeli, J. Shi, J. Chakhalian, and S. Ramanathan. Self-limited kinetics of electron doping in correlated oxides. *Applied Physics Letters*, 107(3):031905, 2015.

[93] A. R. Mazza, Q. Lu, G. Hu, H. Li, J. F. Browning, T. R. Charlton, M. Brahlek, P. Ganesh, T. Z. Ward, H. N. Lee, and G. Eres. Reversible hydrogen-induced phase transformations in $La_{0.7}Sr_{0.3}MnO_3$ thin films characterized by in situ neutron reflectometry. *ACS Applied Materials & Interfaces*, 14(8):10898–10906, 2022. PMID: 35170955.

[94] J. Lee, Y. Ha, and S. Lee. Hydrogen Control of Double Exchange Interaction in $La_{0.67}Sr_{0.33}MnO_3$ for Ionic–Electric–Magnetic Coupled Applications. *Advanced Materials*, 33(11):2007606, 2021.

[95] A. R. Mazza, Q. Lu, G. Hu, H. Li, J. F. Browning, T. R. Charlton, M. Brahlek, P. Ganesh, T. Z. Ward, H. N. Lee, and G. Eres. Reversible hydrogen-induced phase transformations in $La_{0.7}Sr_{0.3}MnO_3$ thin films characterized by in situ neutron reflectometry. *ACS Applied Materials & Interfaces*, 14(8):10898–10906, 2022. PMID: 35170955.

[96] E. Benckiser, Y. Khaydukov, L. Guasco, K. Fürsich, P. Radhakrishnan, G. Kim, and B. Keimer. Complementary insights from neutron and resonant x-ray reflectometry for the study of perovskite transition metal oxide heterostructures. *Physica Status Solidi (b)*, page 2100253, 2021.

[97] R. K. Thomas and J. Penfold. Neutron and x-ray reflectometry of interfacial systems in colloid and polymer chemistry. *Current Opinion in Colloid and Interface Science*, 1(1):23–33, 1996.

[98] R. F. Martin, G. D'cunha, M. Pardee, and B. J. Allen. Induction of DNA double-strand breaks by ^{157}Gd neutron capture. *Pigment Cell Research*, 2(4):330–332.

[99] A. R. Mazza, Q. Lu, G. Hu, H. Li, J. F. Browning, T. R. Charlton, M. Brahlek, P. Ganesh, T. Z. Ward, H. N. Lee, and G. Eres. Reversible hydrogen-induced phase transformations in $La_{0.7}Sr_{0.3}MnO_3$ thin films characterized by in situ neutron reflectometry. *ACS Applied Materials & Interfaces*, 14(8):10898–10906, 2022.

[100] J. Als-Nielsen and D. McMorrow. *Elements of modern X-ray physics*. John Wiley & Sons, 2011.

[101] J. Daillant, S. Mora, and A. Sentenac. Diffuse scattering. In *X-ray and Neutron Reflectivity*, pages 133–182. Springer, 2009.

[102] L. G. Parratt. Surface studies of solids by total reflection of x-rays. *Physical review*, 95(2):359, 1954.

[103] S. Macke, A. Radi, J. E. Hamann-Borrero, A. Verna, M. Bluschke, S. Brück, E. Goering, R. Sutarto, F. He, G. Cristiani, et al. Element specific monolayer depth profiling. *Advanced Materials*, 26(38):6554–6559, 2014.

[104] H. Kuzmany. *Solid-state spectroscopy: an introduction*. Springer, 2009.

[105] W. Hayes and R. Loudon. *Scattering of light by crystals*. Courier Corporation, 2012.

[106] H. Zabel, K. Theis-Bröhl, and B. Toperverg. Handbook of magnetism and advanced magnetic materials (novel techniques for characterization and preparing samples, Vol 3), 2007.

[107] C. Fermon, F. Ott, and A. Menelle. Neutron reflectometry. In *X-ray and Neutron Reflectivity*, pages 183–234. Springer, 2009.

[108] F. Radu and V.K. Ignatovich. Theoretical description of neutron resonances in multilayer systems. *Physica B: Condensed Matter*, 292(1-2):160–163, oct 2000.

[109] V. K. Ignatovich. The remarkable capabilities of recursive relations. *American Journal of Physics*, 57(10):873–878, 1989.

[110] S. J. Blundell and J. A. C. Bland. Polarized neutron reflection as a probe of magnetic films and multilayers. *Phys. Rev. B*, 46:3391–3400, Aug 1992.

[111] S. V. Kozhevnikov, Yu. N. Khaydukov, T. Keller, F. Ott, and F. Radu. Polarized neutron channeling as a tool for the investigations of weakly magnetic thin films. *JETP Letters*, 103(1), Jan 2016.

[112] Yu.N. Khaidukov and Yu.V. Nikitenko. Magnetic non-collinear neutron wave resonator. *Nuclear Instruments and Methods in Physics Research Section A: Accelerators, Spectrometers, Detectors and Associated Equipment*, 629(1):245–250, Feb 2011.

[113] Yu. N. Khaydukov, G. A. Ovsyannikov, A. E. Sheyerman, K. Y. Constantinian, L. Mustafa, T. Keller, M. A. Uribe-Laverde, Yu. V. Kislinskii, A. V. Shadrin, A. Kalaboukhov, B. Keimer, and D. Winkler. Evidence for spin-triplet superconducting correlations in metal-oxide heterostructures with noncollinear magnetization. *Physical Review B*, 90(3), jul 2014.

[114] Yu. Khaydukov, A. M. Petrzhik, I. V. Borisenko, A. Kalabukhov, D. Winkler, T. Keller, G. A. Ovsyannikov, and B. Keimer. Magnetic waveguides for neutron reflectometry. *Physical Review B*, 96(16), oct 2017.

[115] M. Wolff, A. Devishvili, J. A. Dura, F. A. Adlmann, B. Kitchen, G. K. Pálsson, H. Palonen, B. B. Maranville, C. F. Majkrzak, and B. P. Toperverg. Nuclear spin incoherent neutron scattering from quantum well resonators. *Phys. Rev. Lett.*, 123:016101, Jul 2019.

[116] H. Zhang, P. D. Gallagher, S. K. Satija, R. M. Lindstrom, R. L. Paul, T. P. Russell, P. Lambooy, and E. J. Kramer. Grazing incidence prompt gamma emissions and resonance-enhanced neutron standing waves in a thin film. *Phys. Rev. Lett.*, 72:3044–3047, May 1994.

[117] V. Aksenov, Yu V. Nikitenko, F. Radu, Yu M. Gledenov, and P. V. Sedyshev. Observation of resonance enhanced neutron standing waves through (n, *alpha*) reaction. *Physica B: Condensed Matter*, 276-278:946–947, 3 2000.

[118] V. K. Ignatovich and F. Radu. Theory of neutron channeling in the resonant layer of multilayer systems. *Phys. Rev. B*, 64:205408, Oct 2001.

[119] S.V. Kozhevnikov, T. Keller, Yu. N. Khaydukov, F. Ott, and F. Radu. Channeling of neutrons in a nonmagnetic planar waveguide. *Journal of Experimental and Theoretical Physics*, 128(4):504–513, 2019.

[120] I.V Bondarenko, S.N. Balashov, A. Cimmino, P. Geltenbort, A.I. Frank, P. Hoghoj, A.G. Klein, S.V. Masalovich, and V.G. Nosov. Ucn gravity spectrometry using neutron interference filters for fundamental investigations in neutron optics. *Nuclear Instruments and Methods in Physics Research Section A: Accelerators, Spectrometers, Detectors and Associated Equipment*, 440(3):591–596, 2000.

[121] A. Perrichon, A. Devishvili, K. Komander, G. K. Pálsson, A. Vorobiev, R. Lavén, M. Karlsson, and M. Wolff. Resonant enhancement of grazing incidence neutron scattering for the characterization of thin films. *Phys. Rev. B*, 103:235423, Jun 2021.

[122] Y. Khaydukov, E. Kravtsov, V. Progliado, V. Ustinov, Yu. Nikitenko, T. Keller, V. Aksenov, and B. Keimer. Peculiarities of neutron waveguides with thin Gd layer. *Journal of Physics: Conference Series*, 746:012064, sep 2016.

[123] Y. Khaydukov, O. Soltwedel, and T. Keller. Nrex: Neutron reflectometer with x-ray option. *Journal of large-scale research facilities*, page A38, 2015.

[124] A. Devishvili, K. Zhernenkov, A. J. C. Dennison, B. P. Toperverg, M. Wolff, B. Hjörvarsson, and H. Zabel. SuperADAM: Upgraded polarized neutron reflectometer at the Institut Laue-Langevin. *Review of Scientific Instruments*, 84(2):025112, 2013.

[125] M. Trapp. V6: The Reflectometer at BER II. *Journal of large-scale research facilities*, page A114, 2017.

[126] L. Bottyan, D. G. Merkel, B. Nagy, J. Füzi, Sz. Sajti, L. Deák, G. Endroczi, A. V. Petrenko, and J. Major. GINA—A polarized neutron reflectometer at the Budapest Neutron Centre. *Review of Scientific Instruments*, 84(1):015112, 2013.

[127] M. Delheusy, J. Major, A. Ruehm, and A. Stierle. Dedicated beamlines for in-situ investigations of materials in reduced dimensions. *International Journal of Materials Research*, 102(7):913–924, 2011.

[128] M. Björck and G. Andersson. *GenX*: an extensible X-ray reflectivity refinement program utilizing differential evolution. *Journal of Applied Crystallography*, 40(6):1174–1178, Dec 2007.

[129] C. Braun. PARRATT 32 program. *Berlin Neutron Scattering Center (BENSC), Hahn-Meitner Institut, Berlin*, 1997.

[130] Y. Khaydukov, S. Puetter, L. Guasco, G. Morari, R. Kim, T. Keller, A. Sidorenko, and B. Keimer. Proximity effect in [Nb(1.5 nm)/Fe(x)]10/Nb(50 nm) superconductor/ferromagnet heterostructures. *Beilstein J. Nanotechnol.*, 11:1254–1263, 2020.

[131] S. Kokado, M. Tsunoda, K. Harigaya, and A. Sakuma. Anisotropic Magnetoresistance Effects in Fe, Co, Ni, Fe4N, and Half-Metallic Ferromagnet: A Systematic Analysis. *Journal of the Physical Society of Japan*, 81(2):024705, 2012.

[132] T. McGuire and R. Potter. Anisotropic magnetoresistance in ferromagnetic 3d alloys. *IEEE Transactions on Magnetics*, 11(4):1018–1038, 1975.

[133] L. Guasco, Yu. N. Khaydukov, S. Pütter, L. Silvi, M.A. Paulin, T. Keller, and B. Keimer. Resonant neutron reflectometry for hydrogen detection. *Nature Communications*, 13(1):1–8, 2022.

[134] L. Guasco, Yu. N. Khaydukov, S. Pütter, L. Silvi, M.A. Paulin, T. Keller, and B. Keimer. Kinetics of hydrogen absorption in Nb thin films by RNR and XRR. *in preparation*.

[135] A.R. Wildes, J. Mayer, and K. Theis-Bröhl. The growth and structure of epitaxial niobium on sapphire. *Thin solid films*, 401(1-2):7–34, 2001.

[136] Yu. Khaydukov, R. Morari, O. Soltwedel, T. Keller, G. Christiani, G. Logvenov, M. Kupriyanov, A. Sidorenko, and B. Keimer. Interfacial roughness and proximity effects in superconductor/ferromagnet CuNi/Nb heterostructures. *Journal of Applied Physics*, 118(21), 2015.

[137] J. A. Pryde and C. G. Titcomb. Solution of hydrogen in niobium. *Trans. Faraday Soc.*, 65:2758–2765, 1969.

[138] Y. Asada and H. Nosé. Superconductivity of niobium films. *Journal of the Physical Society of Japan*, 26(2):347–354, 1969.

[139] V. Burlaka, S. Wagner, M. Hamm, and A. Pundt. Suppression of phase transformation in Nb–H thin films below switchover thickness. *Nano Letters*, 16(10):6207–6212, 2016. PMID: 27626954.

[140] Q. M. Yang, G. Schmitz, S. Fähler, H. U. Krebs, and R. Kirchheim. Hydrogen in Pd/Nb multilayers. *Phys. Rev. B*, 54:9131–9140, Oct 1996.

[141] G. Reisfeld, Najeh M. Jisrawi, M. W. Ruckman, and Myron Strongin. Hydrogen absorption by thin Pd/Nb films deposited on glass. *Phys. Rev. B*, 53:4974–4979, Feb 1996.

[142] H. Maletta, Ch. Rehm, F. Klose, M. Fieber-Erdmann, and E. Holub-Krappe. Anomalous effects of hydrogen absorption in Nb films. *Journal of Magnetism*

and Magnetic Materials, 240(1):475–477, 2002. 4th International Symposium on Metallic Multilayers.

[143] A Abromeit, R Siebrecht, G Song, H Zabel, F Klose, D Nagengast, and A Weidinger. Thickness dependence of the hydrogen solubility in epitaxial Nb(110) films grown on Al_2O_3(110) substrates. *Journal of Alloys and Compounds*, 253-254:58–61, 1997.

[144] R. J. Walter and W. T. Chandler. The columbium-hydrogen constitution diagram. *Trans. Metall. Soc. AIME*, 233:726, 1965.

[145] N. Boes and H. Züchner. Diffusion of hydrogen and deuterium in Ta, Nb, and V. *Physica Status Solidi (a)*, 17(2):111–114, jun 1973.

[146] S. Tsuchiya, Y. Amenomiya, and R.J. Cvetanović. Study of metal catalysts by temperature programmed desorption: II. Chemisorption of hydrogen on platinum. *Journal of Catalysis*, 19(3):245 – 255, 1970.

[147] M. Eisterer. Radiation effects on iron-based superconductors. *Superconductor Science and Technology*, 31(1):013001, dec 2017.

[148] G.G. Ross and I. Richard. Influence of the ion beam induced desorption on the quantitative depth profiling of hydrogen in a variety of materials. *Nuclear Instruments and Methods in Physics Research Section B: Beam Interactions with Materials and Atoms*, 64(1):603 – 607, 1992.

[149] J. R. Skuza, C. Clavero, K. Yang, B. Wincheski, and R. A. Lukaszew. Microstructural, magnetic anisotropy, and magnetic domain structure correlations in epitaxial FePd thin films with perpendicular magnetic anisotropy. *IEEE Transactions on Magnetics*, 46(6):1886–1889, 2010.

[150] K. Munbodh, F. A. Perez, C. Keenan, D. Lederman, M. Zhernenkov, and M. R. Fitzsimmons. Effects of hydrogen/deuterium absorption on the magnetic properties of Co/Pd multilayers. *Phys. Rev. B*, 83:094432, Mar 2011.

[151] S. M. Valvidares, J. Dorantes-Dávila, H. Isern, S. Ferrer, and G. M. Pastor. Interface-driven manipulation of the magnetic anisotropy of ultrathin Co

films on Pt(111): Substrate deposition of hydrogen and model calculations. *Phys. Rev. B*, 81:024415, Jan 2010.

[152] G. Song, A. Remhof, K. Theis-Bröhl, and H. Zabel. Extraordinary adhesion of niobium on sapphire substrates. *Phys. Rev. Lett.*, 79:5062–5065, Dec 1997.

[153] L. J. Bannenberg, H. Schreuders, H. Kim, K. Sakaki, S. Hayashi, K. Ikeda, T. Otomo, K. Asano, and B. Dam. Suppression of the phase coexistence of the fcc–fct transition in hafnium-hydride thin films. *The Journal of Physical Chemistry Letters*, 12(45):10969–10974, 2021.

[154] C. Zlotea and M. Latroche. Role of nanoconfinement on hydrogen sorption properties of metal nanoparticles hybrids. *Colloids and Surfaces A: Physicochemical and Engineering Aspects*, 439:117–130, 2013. Nanoparticles@interfaces.

[155] P. E. de Jongh, M. Allendorf, J. J. Vajo, and C. Zlotea. Nanoconfined light metal hydrides for reversible hydrogen storage. *MRS Bulletin*, 38(6):488–494, 2013.

[156] M. Fanfoni and M. Tomellini. The Johnson-Mehl- Avrami-Kohnogorov model: A brief review. *Nouv Cim D*, 20:1171–1182, 1998.

[157] M. Avrami. Kinetics of phase change. i general theory. *The Journal of Chemical Physics*, 7(12):1103–1112, 1939.

[158] M. Avrami. Kinetics of phase change. ii transformation-time relations for random distribution of nuclei. *The Journal of Chemical Physics*, 8(2):212–224, 1940.

[159] M. Avrami. Granulation, phase change, and microstructure kinetics of phase change. iii. *The Journal of Chemical Physics*, 9(2):177–184, 1941.

[160] S. S. Das, G. Kopnov, and A. Gerber. Kinetics of the Lattice Response to Hydrogen Absorption in Thin Pd and CoPd Films. *Molecules*, 25(16), 2020.

[161] H. Zabel and J. Peisl. The incoherent phase transitions of hydrogen and deuterium in niobium. *Journal of Physics F: Metal Physics*, 9(7):1461–1476, jul 1979.

[162] M.S. Rashid and T.E. Scott. Crystal structure of niobium hydride. *Journal of the Less Common Metals*, 30(3):399–403, 1973.

[163] K. Nörthemann, R. Kirchheim, and A. Pundt. Surface modification of Nb-films during hydrogen loading. *Journal of Alloys and Compounds*, 356-357:541–544, 2003. Proceedings of the Eighth International Symposium on Metal-Hydrogen Systems, Fundamentals and Applications (MH2002).

[164] Laura Guasco, Yury Khaydukov, Gideok Kim, Thomas Keller, Alexei Vorobiev, Anton Devishvili, Peter Wochner, Georg Christiani, Gennady Logvenov, and Bernhard Keimer. Emergent magnetic fan structures in manganite homojunction arrays. *Advanced Materials*, 34(35):2202971, 2022.

[165] J. Hemberger, A. Krimmel, T. Kurz, H.-A. Krug von Nidda, V. Yu. Ivanov, A. A. Mukhin, A. M. Balbashov, and A. Loidl. Structural, magnetic, and electrical properties of single-crystalline $LaSrMnO_3$. *Phys. Rev. B*, 66:094410, Sep 2002.

[166] O. Chmaissem, B. Dabrowski, S. Kolesnik, J. Mais, J. D. Jorgensen, and S. Short. Structural and magnetic phase diagrams of $LaSrMnO_3$ and $PrSrMnO_3$. *Phys. Rev. B*, 67:094431, Mar 2003.

[167] J. Eichler, M. Novák, and M. Kosek. Experimental determination of the preisach model for grain oriented steel. *Acta Physica Polonica, A.*, 136(5), 2019.

[168] P. Schiffer, A. P. Ramirez, W. Bao, and S-W. Cheong. Low Temperature Magnetoresistance and the Magnetic Phase Diagram of $La_{1-x}Ca_xMnO_3$. *Phys. Rev. Lett.*, 75:3336–3339, Oct 1995.

[169] A. P. Ramirez. Colossal magnetoresistance. *Journal of Physics: Condensed Matter*, 9(39):8171–8199, sep 1997.

[170] M. Granada, J. C. Rojas Sánchez, and L. B. Steren. Giant magnetoresistance in oxide-based metallic multilayers. *Applied Physics Letters*, 91(7):072110, 2007.

[171] S. J. May, A. B. Shah, S. G. E. te Velthuis, M. R. Fitzsimmons, J. M. Zuo, X. Zhai, J. N. Eckstein, S. D. Bader, and A. Bhattacharya. Magnetically asymmetric interfaces in a $LaMnO_3/SrMnO_3$ superlattice due to structural asymmetries. *Phys. Rev. B*, 77:174409, May 2008.

[172] Y. P. Feng, C. F. Majkrzak, S. K. Sinha, D. G. Wiesler, H. Zhang, and H. W. Deckman. Direct observation of neutron-guided waves in a thin-film waveguide. *Phys. Rev. B*, 49:10814–10817, Apr 1994.

[173] Yu N Khaidukov and MA Andreeva. Waveguide enhancement of spin-flip scattering in reflection of polarized neutrons from the" soft-magnetic/hard-magnetic" layered structure. *Physics Bulletin*, 59(2), 2005.

[174] Yu. Khaydukov, A. M. Petrzhik, I. V. Borisenko, A. Kalabukhov, D. Winkler, T. Keller, G. A. Ovsyannikov, and B. Keimer. Magnetic waveguides for neutron reflectometry. *Phys. Rev. B*, 96:165414, Oct 2017.

[175] T. Koida, M. Lippmaa, T. Fukumura, K. Itaka, Y. Matsumoto, M. Kawasaki, and H. Koinuma. Effect of a-site cation ordering on the magnetoelectric properties in $[(LaMnO_3)_m/(SrMnO_3)_m]_n$ artificial superlattices. *Phys. Rev. B*, 66:144418, Oct 2002.

[176] A. Glavic, H. Dixit, V. R. Cooper, and A. A. Aczel. Constructing a magnetic handle for antiferromagnetic manganites. *Phys. Rev. B*, 93:140413, Apr 2016.

[177] M. Keunecke, F. Lyzwa, D. Schwarzbach, V. Roddatis, N. Gauquelin, K. Müller-Caspary, J. Verbeeck, S. J. Callori, F. Klose, M. Jungbauer, and V. Moshnyaga. High-Tc Interfacial Ferromagnetism in $SrMnO_3/LaMnO_3$ Superlattices. *Advanced Functional Materials*, 30(18):1808270, 2020.

[178] T. S. Santos, S. J. May, J. L. Robertson, and A. Bhattacharya. Tuning between the metallic antiferromagnetic and ferromagnetic phases of

$La_{1-x}Sr_xMnO_3$ near $x = 0.5$ near $x = 0.5$ by digital synthesis. *Phys. Rev. B*, 80:155114, Oct 2009.

[179] T. S. Santos, B. J. Kirby, S. Kumar, S. J. May, J. A. Borchers, B. B. Maranville, J. Zarestky, S. G. E. te Velthuis, J. van den Brink, and A. Bhattacharya. Delta doping of ferromagnetism in antiferromagnetic manganite superlattices. *Phys. Rev. Lett.*, 107:167202, Oct 2011.

[180] A. Brataas, G. E.W. Bauer, and P. J. Kelly. Non-collinear magnetoelectronics. *Physics Reports*, 427(4):157–255, 2006.

[181] F. A. Lewis. *The palladium/hydrogen system*. Citeseer, 1967.

[182] J. Chen, W. Mao, L. Gao, F. Yan, T. Yajima, N. Chen, Z. Chen, H. Dong, B. Ge, P. Zhang, X. Cao, M. Wilde, Y. Jiang, T. Terai, and J. Shi. Electron-doping mottronics in strongly correlated perovskite. *Advanced Materials*, 32(6):1905060, 2020.

[183] V.G. Syromyatnikov, A.F. Schebetov, A.P Lott, D. and. Bulkin, N.K. Pleshanov, and V.M. Pusenkov. PNPI wide-aperture fan neutron supermirror analyzer of polarization. *Nucl. Inst. Meth.*, 634:S126, 2011.

[184] A.G. Gilev, N.K. Pleshanov, B.A. Bazarov, A.P. Bulkin, A.F. Schebetov, V.G. Syromyatnikov, V.V. Tarnavich, and V.A. Ulyanov. Magnetic systems for wide-aperture neutron polarizers and analyzers. *Nucl. Inst. Meth. A*, 833:233, 2016.

[185] K. Halbach. Design of permanent multipole magnets with oriented rare earth cobalt material. *Nuclear Instruments and Methods*, 169:1, 1980.

Acknowledgements

First of all I would like to thank Professor Bernhard Keimer for allowing me to join his group of very talented but at the same time very nice people. He always showed great trust in me and my projects, steering them so that they reached their highest potential. Secondly, I have to thank my day to day supervisors Thomas Keller, for the incessant encouraging words and guidance he gave me, and Yury Khaydukov, for patiently teaching me practically everything I know in reflectometry and thin films, for all the fruitful discussions we had, but also for always being a good friend to share a laugh with. I was lucky to work with him and I will never be able to thank him enough!

I am really grateful to all the people that I collaborated with during my Ph.D., in particular Gideok Kim, not only for his top of the notch samples, experiments together, and his valuable advices, but also for all the good times we had together. I want to thank Sabine Pütter for her high-quality samples, encouragement, and for all our nice discussions. Thanks to Liz Montanez for the help with AFM images. Thanks to Luca Silvi and Mariano Paulin, for our unforgettable beamtimes at the Ber II reactor, which were successful thanks to your support and never felt too tiring in your company. Thanks to the colleagues of Uppsala University, Anton Devishvili and Alexei Vorobiev, for their help and expertise during the beamtimes at ILL, and for the good discussions we had. Thanks to the thin film technology group, in particular Gennady Logvenov and Georg Christiani, for always being enthusiastic and supportive in our common projects. Thanks as well to Peter Wochner for the help during the beamtime at KARA.

I would also like to thank all the people of professor Keimer's department. Thanks to Eva Benckiser for the nice discussions about hydrogen and for her support in the matters of the graduate school. Thanks to Padma Radhakrishnan,

for being so friendly and honest with me, thanks to Katrin Fürsich for her help with the teaching classes and for nice chats about women in science, thanks to Cissy Suen for being a good friend, and thanks to Heiko Trepka, for helping me out in several occasions. Even though I was not spending much time in Stuttgart I always felt welcome and I was always happy to spend time with the group, so for this I want to thank Ksenia Rabinovich, Valentin Zimmermann, Suguru Nakata, Rebecca Pons, Roberto Ortiz, Sajna Hameed, Hun-Ho Kim, Matteo Minola, David Dawson, Matthias Hepting, Alexander Boris, Christopher Dietl, Elirjete Kryeziu, and Petar Yordanov. I also want to thank Sonja Balkema for all her support on administrative matters.

Finally I want to thank the people that supported me outside of the scientific environment. Thanks to Kaltrina, Johannes, Ceren, Ben, Rafał, Fiammetta, and Giancarlo that perfectly understand the Ph.D. life and were always there for me when I needed advices, distraction, or to celebrate together. Thanks also to all my dear friends Neda, Sara, Ambra, Alex, Richi, Marco, Matte, Dave, and Ericka who always encouraged me and stood by me.

A big, enormous thanks goes to my family and in particular my parents, for being my number 1 supporters, and to my partner in life Michał, for the advices, the cheering and the all the love he showed me.

Grazie a tutti!

Appendix A

Fan analyzer design

In this appendix, we report on the design and testing of a wide area polarization analyzer for NREX. The active area of this analyzer (200 mm$x$200 mm) covers the entire sensitive area of the 2-dimensional detector at NREX. Simultaneous polarization analysis of the specular and diffuse reflectivity leads to a gain factor of 40 in measurement time compared to the present analyzer with a small active area of 5 mm$x$200 mm. The analyzer is a fan-shaped arrangement of 30 polarizing FeSi supermirrors on 1 mm Borofloat glass substrates. A compact yoke with permanent magnets was optimized by a finite element analysis to provide a uniform field of 700 Gs across the analyzer volume (200 mm$x$200 mm$x$250 mm). Test mirrors characterized at NREX show a polarization efficiency of $\sim 99\%$.

A.1 Introduction

The NREX neutron reflectometer at the MLZ is optimized for the investigation of magnetization profiles of thin film heterostructures by neutron polarization analysis. NREX is operated at constant wavelength (4.28 Å) in $\theta - 2\theta$ mode, the sample surface is horizontal. A 2-dimensional detector collects on 200 mm$x$200 mm both specular and off-specular reflected intensities with a position resolution of ~ 3 mm. The polarization analysis involves the instrument components polarizer (P), radio frequency spin flippers (SF), sample electromagnet, and polarization analyzer (AP). Both the P and the AP at present are single FeSi supermirrors on 0.3 mm

silicon substrates, operating in transmission mode. The polarization efficiency of these mirrors is optimal, with a flipping ratio FR > 200, but the transmitted beam is narrow in height, $\sim 5\,\mathrm{mm}$. This does not represent a problem for the polarizer, since the beam height upstream the sample is $< 1\,\mathrm{mm}$, but the analyzer illuminates only $\sim 5\,\mathrm{mm}$ of the full detector height of $200\,\mathrm{mm}$. For the measurement of the specular reflectivity this narrow beam height is no severe limitation, but for the polarization analysis of the diffuse scattering arising from lateral magnetic structures, such as magnetic domains, a wide area analyzer covering the whole detector would save a factor $200/5 = 40$ in measurement time.

A.2 Analyzer design

There are two different concepts for the design of such wide area analyzers. The first one is based on the spin dependent neutron absorption in nuclear spin-polarized He-3 gas in a quartz cell, where a strong laser drives the nuclear polarization process. Such polarizers exist, but are not commercialized and require extensive expert knowledge and a dedicated technician for operation. The second concept is based on magnetic supermirrors. If properly designed, these devices are easy to use also by non-experts.

For reflectometers fan-shaped supermirror analyzer [183] has advantages over so-called benders. The mirrors are flat and need not to be curved, such that the alignment of the mirrors is easy and precise. The layout of the fan-type analyzer takes advantage of the small beam height at the sample. Fig. A.1 shows the polarizing mirrors are arranged radially around a center C, with a vertical offset h_0 from the sample center. Spin-up neutrons reflected by the sample will be reflected by the FeSi coating of the analyzer mirrors towards the detector, spin-down neutrons will be absorbed in the borated glass substrates of the mirrors. Due to the radial geometry the range of reflection angles are the same on each mirror of the fan.

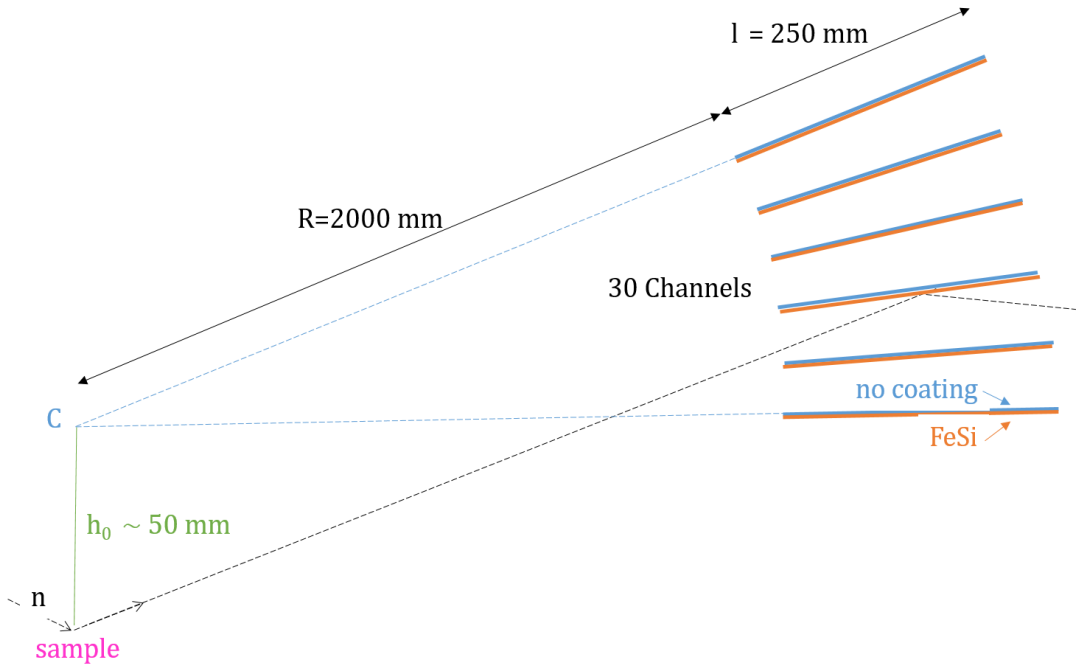

Figure A.1: Fan-shaped polarization analyzer (side view). The mirrors are arranged in a radial alignment on the center line C, which is located $\sim 50\,\mathrm{mm}$ above the sample. The Borofloat substrates ($1\,\mathrm{mm}x200\,\mathrm{mm}x250\,\mathrm{mm}$) are coated on the bottom side with a FeSi bandpass, $m = 2.5 - 3.5$, the other side is not coated.

A.2.1 Geometry of the fan-shaped analyzer

The geometry parameters of the fan are the radius R, the vertical entrance width of one channel w_i, the length of the mirror l, the thickness of the glass substrate w_m, and the m-value of the coating. Fig. A.2 shows a side view of one analyzer channel. The radius $R = 2000\,\mathrm{mm}$ is given by the sample-analyzer distance at NREX. The mirrors have a relatively large area and are supported only at the side, outside the beam area. To avoid bending by gravity, a glass of thickness $w_m = 1.0\,\mathrm{mm}$ will be used.

The m-value of the polarizing FeSi coating is determined by the range of reflection angles α and the neutron wavelength $\lambda = 4.28\,\text{Å}$. The range of α is given by the inclination of the fan and the entrance width w_i of the channels. The minimum α should be large enough to avoid reflection of the spin-down neutrons at

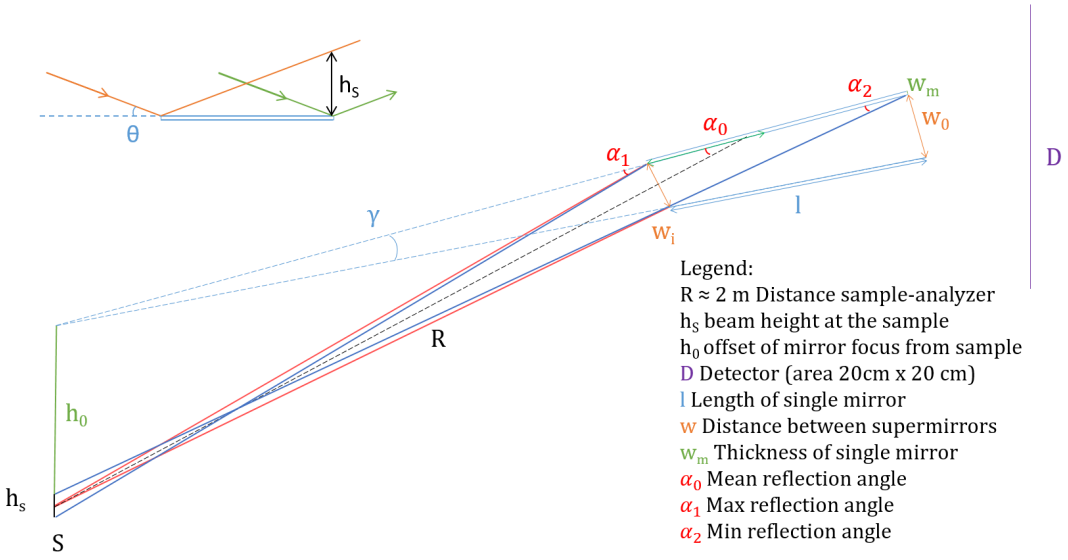

Figure A.2: Parameter definitions showing one channel of the fan analyzer. The inset shows the reflection at the sample. $R = 2000\,\text{mm}$, $w_m = 1.0\,\text{mm}$, $w_i = 5.0\,\text{mm}$, $l = 250\,\text{mm}$, angle between mirrors $\gamma = 0.172°$, width of the mirror 200 mm, $m = 2.5 - 3.5$ (FeSi bandpass). The mirrors are coated only on one side.

the silicon layers, which happens for $\alpha < 0.06° \times \lambda[\text{Å}] = 0.26°$, and the m-value should be < 3.5. Higher m are possible, but at dramatically increased cost. The choice of w_i is no clear-cut task. The geometrical transmission factor $w_i/(w_i + w_m)$ increases with increasing w_i and constant substrate thickness $w_m = 1\,\text{mm}$. Neutron reflections inside the channel smear out the vertical resolution, which is in the worst case given by the channel width. If the channel is wide enough that single reflections are sufficient to provide acceptable transmission, then by coating only one side of the channel with FeSi will avoid double reflections, and the vertical position resolution within one channel can be partly recoverd by vertical inversion of the intensity profile. Finally, we will use $w_i = 5\,\text{mm}$ with 83% transmission for spin-up neutrons.

We first calculate the effective beam height at the sample, and then the range of reflection angles at the mirrors. The reflection at the sample is shown in the inset of Fig A.2. We assume a maximum sample length of 30 mm, and a maximum momentum transfer of $Q = 0.5\,\text{Å}^{-1}$. With $\lambda = 4.28\,\text{Å}$, we get the minimum

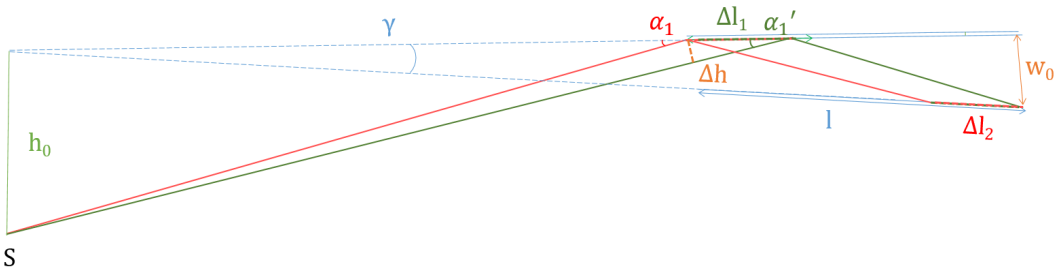

Figure A.3:

incident angle θ and and the beam height h_S at the sample:

$$\theta = \arcsin\left(\frac{Q\lambda}{4\pi}\right) = 9.8° \tag{A.1}$$

$$h_S = l_S \tan(\theta) = 5.18\,\text{mm} \tag{A.2}$$

The maximum reflection angle occurs at the entrance α_1 for a trajectory from the lower side of h_S (Fig. A.2). We choose $m_{\max} = 3.4$ for the FeSi mirror, then for $\lambda = 4.28\,\text{Å}$ we get with the critical angle of reflection $\theta_c(\lambda, m) = 0.1° \times \lambda[\text{Å}] \times m$

$$\alpha_{1\,\max} = 1.46° \tag{A.3}$$

$$\alpha_{2\,\min} = \alpha_{1\,\max} - \frac{w_i}{R} - \frac{h_S}{R} = 1.16° \tag{A.4}$$

To reflect a neutron at the angle $\alpha_{2\,\min}$, $m_{\min} = 2.7$ is required. As there are no smaller reflection angles, the FeSi coating can be produced as a band pass. We choose

$$2.5 < m < 3.5 \tag{A.5}$$

Omitting the smaller m-values with associated thick Fe and Si layers has the advantage, that both the flipping ration and the micro-roughness and reflectivity of the mirrors is improved.

The inclination of the fan is given as offset of the center C from the sample:

$$h_0 = R\sin(\alpha_{1\,\max} - h_S/(2R)) = 48\,\text{mm} \tag{A.6}$$

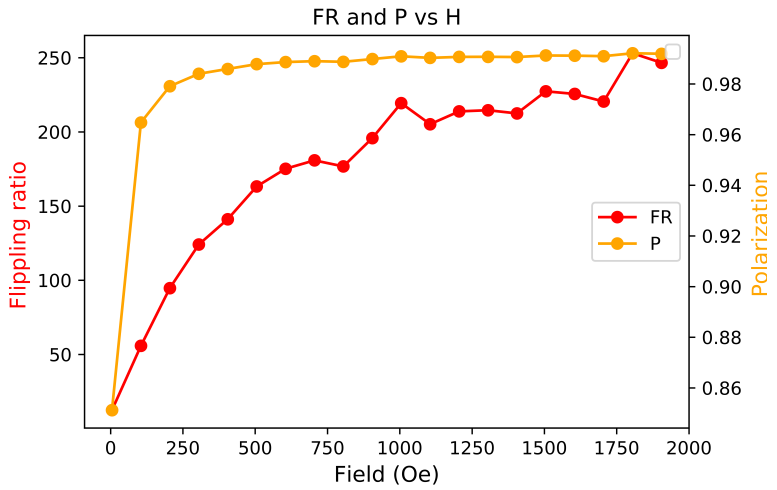

Figure A.4: Flipping ratio and polarization versus B of a FeSi bandpass mirror ($m = 2.5 - 3.5$) measured at NREX.

The mirrors must be sufficiently long to suppress the direct sight from the sample to the detector, such that all neutrons are reflected and spin-analyzed. From Fig. A.2

$$l_{\min} = \frac{w_i}{\tan(\alpha_{2\,\min})} = 247\,\text{mm} \tag{A.7}$$

We choose as design value $l = 250\,\text{mm}$. The angle between the mirrors is

$$\gamma = \frac{w_i + w_m}{R} = 0.172 \tag{A.8}$$

Then the width of the channel at the exit is

$$w_o = w_i + \gamma l = 5.75\,\text{mm} \tag{A.9}$$

With 30 channels the detector height of 200 mm is covered.

Double reflection inside the analyzer channel is suppressed, as neutrons being reflected on the FeSi mirror within the region Δl_1 (Fig. A.3), hit the opposite glass surface in the area Δl_2 at angles close to $\alpha_1 \simeq 1.2°$, which are well above the critical reflection angle of glass, and are absorbed in the glass. Neutrons passing the entrance window within the region Δh thus are lost. The transmission including

the geometrical losses is then

$$T = 1 - \frac{\Delta h + w_m}{w_m + w_i} = 0.74 \tag{A.10}$$

where the loss by single sided coating of the substrates is only about 9%. In eq. A.10 and Fig. A.3 we use

$$\begin{aligned} \alpha_1' &= \frac{w_o}{l - \Delta l_1} = \frac{\Delta h}{\Delta l_1} \\ \Delta l_1 &= \frac{h_0 l - w_o R \cos(\alpha_1)}{h_0 + w_o} = 21.3\,\text{mm} \\ \Delta h &= \frac{\Delta l_1 w_o}{l - \Delta l_1} = 0.54\,\text{mm} \end{aligned}$$

Finally we estimate the neutron absorption of the glass substrates, which is important to avoid leakage of spin-down neutrons to the neighboring channel. A borosilicate glass suitable for the substrates is Schott D263, which contains about 9% (weight) of B_2O_3. With a glass density of $2.51\,\text{g/cm}^3$ the number density of boron atoms is $n = 3.9 \times 10^{21}\,\text{cm}^{-3}$. The absorption cross section of natural boron is $\sigma_{\text{th}} = 767\,\text{barn}$, and the linear absorption coefficient is $\sigma_{th} \times n = 3.0\,\text{cm}^{-1}$ (for $\lambda = 1.8\,\text{Å}$). For $\lambda = 4.28\,\text{Å}$ and a maximum angle of incidence $\alpha_{1\,\text{max}} = 1.46°$, the effective path length through the 1 mm glass is $d_{\text{eff}} = 3.9\,\text{cm}$, and the transmission is $\exp(-\sigma n d_{\text{eff}}) = 7.8 \times 10^{-13}$, and thus can be safely neglected.

A.2.2 Magnetizing field

The FeSi supermirrors require a relatively large magnetization field, where the flipping ratio (FR) improves by increasing B. Fig. A.4 shows the fliping ratio FR and polarization efficiency $(\text{FR} - 1)/(\text{FR} + 1)$ of a test mirror measured at NREX. Our minumum requirement (FR = 100) is met with a magnetizing field $B \sim 250\,\text{Gs}$, but the FR increases with B. We designed a yoke with NdFeB magnets generating $B \sim 700\,\text{Gs}$ with sufficient homogeneity and relatively low external fields. The layout follows an idea from the Gatchina group [184] based on a iron box yoke, and a magnet configuration in the spirit of the Halbach [185] with partially opposite polarity of the magnets. Fig. A.5(a) shows the yoke made

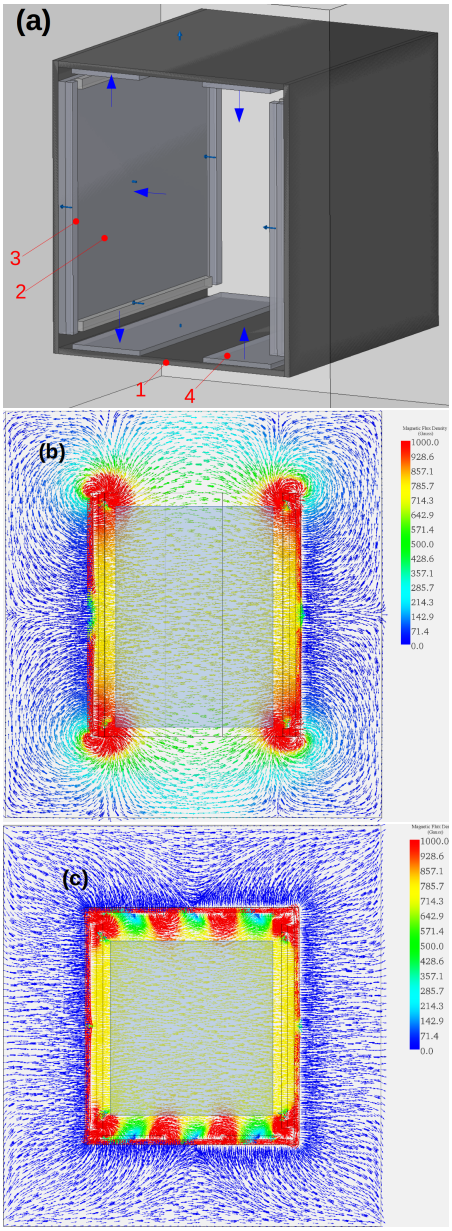

Figure A.5: (a) Yoke with NdFeB permanent magnets. 1: Iron box (ARMCO, 6 mm), outer dimensions 260 mm$x$290 mm$x$300 mm (width x height x length). 2-4: Permanent magnets, thickness 8 mm (2,3), and 5 mm (4). The blue arrows indicate the magnetization direction. (b) Field $\boldsymbol{B}$ in the horizontal symmetry plane, the grey area (200 mm$x$250 mm) shows the size of the mirror. (c) $\boldsymbol{B}$ in the vertical symmetry plane. The grey area (200 mm$x$250 mm) shows the size of the entrance window. The unit of the scale is Gauss.

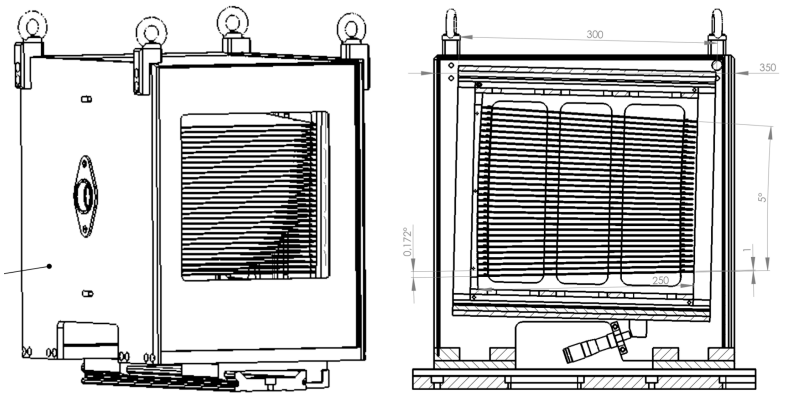

Figure A.6: Mechanical design of the fan analyzer for NREX

from pure (ARMCO) iron (1). The main field is generated by the magnets (2, NdFeB thickness 8 mm). The magnets (4, NeFeB thickness 5 mm) help to improve the homogeneity of B in the vertical direction, and the magnet stripes (3) reduce the drop of the field in beam direction from the center to the entrance and exit windows. The plots in Fig. A.5(b,c) show $\boldsymbol{B}$ in horizontal and vertical symmetry planes calculated with the EMWorks finite elements software. We optimized the homogeneity by changing the magnet dimensions and positions.

The mechanical design is shown in Fig. A.6. The magnet yoke with the mirrors is housed in a second box with bearings at the side and a manual micrometer to adjust the inclination angle of the stack. This outer box also protects the fragile mirrors during installation. The total weight of the analyzer is 36 kg.